UNIVERSITY OF CALIFORNIA SAN DIEGO

Diagnostics and Prognostics of Pitting Corrosion in Large Civil infrastructure Using Multi-scale Simulation and Machine Learning

A dissertation submitted in partial satisfaction of the
requirements for the degree Doctor of Philosophy

in

Structural Engineering

by

Guofeng Qian

Committee in charge:

Professor Michael D. Todd, Chair
Professor Joel Conte
Professor Charles Farrar
Professor Zhen Hu
Professor Behrouz Touri

2023

The Dissertation of Guofeng Qian is approved, and it is acceptable in quality and form for publication on microfilm and electronically.

University of California San Diego

2023

DEDICATION

This dissertation is dedicated to my wife, Cindy, who believed in me when I didn't. I also dedicate this to my parents, Yu and Bangjun, who always support me for higher education.

EPIGRAPH

All models are wrong, but some are useful.

George E.P. Box

TABLE OF CONTENTS

LIST OF FIGURES

LIST OF TABLES

ACKNOWLEDGEMENTS

The completion of this dissertation is profoundly indebted to the support of numerous individuals. Foremost, I express my gratitude to my advisor and mentor, Professor Michael Todd, whose belief in me and guidance have been instrumental throughout my research journey. I also extend my acknowledgment to Professor Zhen Hu, with whom I had the opportunity to work closely, and whose substantial contributions greatly enriched my work.

Portions of this dissertation have been published or are currently being considered for publication. Chapter 2 is composed of two publications:

Guofeng Qian, Karnpiwat Tantratian, Lei Chen, Zhen Hu, and Michael D Todd. A probabilistic computational framework for the prediction of corrosion-induced cracking in large structures. *Scientific Reports*, 12(1):20898, 2022.

Guofeng Qian, Zhen Hu, and Michael D Todd. A hybrid surrogate modeling method for corrosion morphology prediction under non-stationary dynamic loading. In Structural Health Monitoring 2023, *Proceedings of the International Workshop on Structural Health Monitoring 2023*, pages 643–650. DEStech, 2023.

Chapter 3 is composed of two publications:

Guofeng Qian, Karnpiwat Tantratian, Lei Chen, Zhen Hu, and Michael D Todd. A probabilistic computational framework for the prediction of corrosion-induced cracking in large structures. *Scientific Reports*, 12(1):20898, 2022.

David A Najera-Flores, **Guofeng Qian**, Zhen Hu, and Michael D Todd. Corrosion morphology prediction of civil infrastructure using a physics-constrained machine learning method. *Mechanical Systems and Signal Processing*, 200:110515, 2023

Chapter 4 is composed of one publication:

Guofeng Qian, Zhen Hu, and Michael D Todd. Physics-based corrosion reliability analysis of miter gates using multi-scale simulations and adaptive surrogate modeling. *Mechanical Systems and Signal Processing*, 200:110619, 2023.

Chapter 5 is currently in preparation for publication:

Guofeng Qian, Zihan Wu, Zhen Hu, and Michael D Todd. Pitting corrosion diagnostics and prognostics using multi-scale simulation and image inspection data. In preparation.

The author acknowledges financial support from the United States Army Corps of Engineers through the US Army Engineer Research and Development Center Research Cooperative Agreement W9132T-22-2-20014.

VITA

2019	Bachelor of Engineering, Harbin Institute of Technology, China
2019–2020	Master of Science, University of California San Diego
2021–2023	Research Assistant, University of California San Diego
2023	Doctor of Philosophy, University of California San Diego

PUBLICATIONS

Guofeng Qian, Zhen Hu, and Michael D Todd. Physics-based corrosion reliability analysis of miter gates using multi-scale simulations and adaptive surrogate modeling. *Mechanical Systems and Signal Processing*, 200:110619, 2023.

Guofeng Qian, Karnpiwat Tantratian, Lei Chen, Zhen Hu, and Michael D Todd. A probabilistic computational framework for the prediction of corrosion-induced cracking in large structures. *Scientific Reports*, 12(1):20898, 2022.

Guofeng Qian, Zhen Hu, and Michael D Todd. A hybrid surrogate modeling method for corrosion morphology prediction under non-stationary dynamic loading. In Structural Health Monitoring 2023, *Proceedings of the International Workshop on Structural Health Monitoring 2023*, pages 643–650. DEStech, 2023.

Guofeng Qian, Zhen Hu, and Michael D Todd. Physics-based corrosion reliability analysis of miter gates using multi-scale simulations. *In Society for Experimental Mechanics Annual Conference and Exposition*, pages 101–105. Springer, 2023.

David A Najera-Flores, **Guofeng Qian**, Zhen Hu, and Michael D Todd. Corrosion morphology prediction of civil infrastructure using a physics-constrained machine learning method. *Mechanical Systems and Signal Processing*, 200:110515, 2023.

Zhao, Ying, Mayank Chadha, Nicholas Olsen, Elissa Yeates, Josh Turner, Guga Gugaratshan, **Guofeng Qian**, Michael D. Todd, and Zhen Hu. "Machine learning-enabled calibration of river routing model parameters." *Journal of Hydroinformatics* 25, no. 5 (2023): 1799-1821.

Guofeng Qian, Zihan Wu, Zhen Hu, and Michael D Todd. Pitting corrosion diagnostics and prognostics using multi-scale simulation and image inspection data. (in progress)

ABSTRACT OF THE DISSERTATION

Diagnostics and Prognostics of Pitting Corrosion in Large Civil infrastructure Using Multi-scale Simulation and Machine Learning

by

Guofeng Qian

Doctor of Philosophy in Structural Engineering

University of California San Diego, 2023

Professor Michael D. Todd, Chair

Corrosion, particularly pitting corrosion, stands as one of the most prevalent forms of deterioration in large infrastructure, known for its slow, continuous, capacity-degrading nature. With the aging of structures, there is an increasing demand for the assessment and monitoring of corrosion status to facilitate system life-cycle management and optimal maintenance. However, due to the intricacies involved in the corrosion process, several challenges impede effective diagnosis and prognosis. These challenges include the inadequate coupling of mechanical stress into existing corrosion simulations, the computational intensity of most physics-based corrosion simulations limiting probabilistic studies and real-time predictions, and the difficulty in detecting

pitting corrosion due to its localized nature, making it impractical to measure individual pits. This dissertation presents a comprehensive prognosis and diagnosis framework applied to a miter gate case study. The framework integrates multi-scale simulation including mesoscale Phase-Field (PF) simulation and macroscale structural analysis with Machine Learning (ML) methods to enable real-time corrosion diagnosis and prognosis. It enables for effective structural health monitoring (SHM) with digital twin (DT) for corrosion damage. The key components of this framework encompass the development of a multi-scale simulation for simulating pitting corrosion in large structures, the construction of ML-based surrogate models to expedite simulations, the implementation of both aleatory and epistemic uncertainty quantification (UQ), and the integration of pitting corrosion diagnosis and prognosis.

Chapter 1

Introduction

Civil infrastructure systems are distinct from other structures due to their extensive length scales, high cost, and unique design and performance characteristics. Furthermore, many civil infrastructure used in inland waterways navigation (like navigational locks in the US) are required to operate even after their design life [49]. With the aging of these structures, there is an escalating necessity for the assessment of their condition and the prediction of structural deterioration state (i.e., damage) to ensure their continued safety. However, the traditional time-based maintenance approach is susceptible to the risks posed by unforeseen faults occurring between inspections, and it is not cost-effective when dealing with a structure in an otherwise sound condition. Therefore, implementing continuous condition assessment alongside damage prediction can facilitate optimal maintenance practices, ensuring safer and more cost-effective system-level life-cycle management.

Corrosion stands as one of the most prevalent forms of deterioration in civil infrastructure, with pitting corrosion (defined in detail later) recognized as the most destructive manifestation [159]. On one hand, material loss resulting from corrosion can lead to component failure, significantly impacting the structural integrity of the infrastructure. On the other hand, deep pits characterized by sharp interfaces have the potential to initiate stress corrosion cracking (SCC), particularly under dynamic cyclic loading conditions [81]. However, pitting corrosion often occurs in localized areas, making it challenging to detect before it significantly affects the overall

structural integrity. Therefore, the development of a comprehensive diagnosis and prognosis framework for pitting corrosion in civil infrastructure is imperative.

1.1 Pitting Corrosion

1.1.1 Mechanisms

Pitting corrosion is characterized by localized metal dissolution resulting from the breakdown of a passive fluid film on a metallic surface. This breakdown is often instigated by chloride ions due to their relatively small size and high diffusivity, as documented by Frankel [52]. In the presence of dissolved oxygen in water, the reaction $O_2 + 2H_2O + 4e^- \rightarrow 4OH^-$ takes place at the metal surface as the Figure 1.1. The process of metal dissolution can be represented by the equation $M \rightarrow M^{n+} + ne^-$. Subsequent pit growth is facilitated through both anodic and cathodic electrochemical reactions once a pit starts to develop. The accumulation of positive ions (M^+) on the anodic side leads to the reaction $M^+ + H_2O \rightarrow MOH + H^+$, creating an acidic environment that further promotes pit growth and propagation.

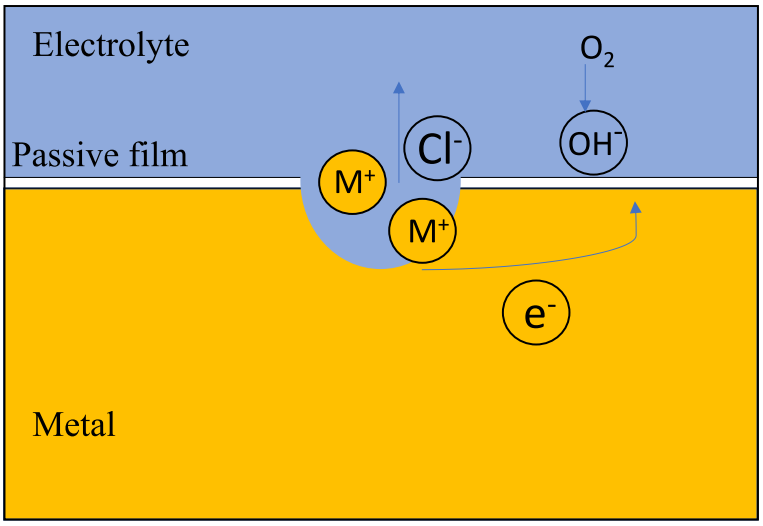

Figure 1.1. Pitting corrosion mechanism

In pitting corrosion, three distinct stages are commonly identified: the initiation stage, the metastable stage, and the stable stage. The initiation stage, associated with the breakdown

of the passive film, is not thoroughly understood, primarily due to the challenges in directly observing the breakdown event and the typically nanometer-scale dimensions of most passive films. The initiation process involves intricate mechanisms of nucleation and early propagation, which currently remain a subject of active research [51, 83, 84, 86, 87]. Following the initiation stage, if a pit only undergoes limited growth before repassivation, it falls within the metastable stage. Metastable pits are generally micron-sized. Although the influence of metastable pits may not be significant, they can potentially continue to grow into larger pits. If they continue to evolve past the metastable stage, pits progress into the stable stage, where their growth is primarily influenced by factors such as material properties, potential, ion concentration, and mass transportation. Among the three stages, the stable stage has been the subject of more comprehensive study and understanding. From a structural perspective, the breakdown of the passive film and the presence of micron-sized pits have minimal effects at the component or higher level. Therefore, the stable stage remains the primary focus of the current study.

Pitting corrosion is influenced by numerous factors, including material composition, environmental conditions, and surface characteristics. Notably, several experiments have indicated that the stress field exerted on the metal also significantly impacts the corrosion behavior [108, 164]. This observation is particularly critical given that the stress field within a civil infrastructure is typically intricate and subject to alteration. Despite these experimental findings, a comprehensive connection between these observations and their implications for civil structures has yet to be established.

1.1.2 Modeling and Simulation

The pit initiation process is modeled statistically due to the lack of detailed understanding of its mechanisms. The corrosion initiation stage is characterized by the time until local corrosion commences. Research has found the corrosion initiation time for steel to be dependent on various factors, including temperature, the concentration of metal cations, and the potential drop across the interface [83, 85]. Despite these findings, the precise electrochemical mechanisms governing

corrosion initiation continue to not be well understood. Consequently, owing to the absence of a comprehensive physics-based model, corrosion initiation time is typically assumed to be a random variable, derived from historical or experimental data [132, 142]. Notably, in the context of reinforced concrete structures, corrosion is often assumed to initiate when the chloride concentration on the steel surface exceeds a certain threshold [125].

Different kinds of computational models have been proposed to simulate pitting corrosion stable growth such as the finite volume method (FVM) [128], cellular automata (CA) techniques [137], peridynamic (PD) formulations [161], and phase-field (PF) models [30]. Among them, the phase-field method shows great potential and flexibility in simulating the morphological evolution of the pitting corrosion process and SCC initiation process [72]. The model involves multiple coupled partial differential equations (PDEs) including the Allen-Cahn equation describing phase transition and the Cahn-Hilliard equation describing the evolution of the molar concentration of metal atoms [90]. The PF model considers the influence of mechanical stress by coupling a stress equilibrium PDE into the model [98, 118]. Nevertheless, the model is intrinsically computationally expensive as it consists of multiple coupled PDEs.

The progression from pit to stress corrosion cracking initiation may also be modeled. Two criteria are commonly utilized to describe this transition process, which essentially involves a competition between pit growth and crack growth. One approach involves comparing the current stress intensity factor, estimated using empirical formulas, with the threshold stress intensity factor [142]. The other criterion involves comparing the pit growth rate derived from the corrosion growth model with the crack growth rate based on Paris' law, assuming that the current pit shape represents a short crack [132].

1.2 Structural Health Monitoring and Prognostics

1.2.1 Overall Strategy

Structural Health Monitoring refers to an automated monitoring practice that aims to evaluate the condition or health of a structure [35, 47, 48]. The practice involves obtaining measurements, extracting damage-sensitive features from those measurements, and statistically inferring the structural condition from those features with uncertainty quantified, so as to support decision-making. Thus, a diagnosis is an assessment structural condition/state, conditioned upon observing and characterizing observed features from data. Furthermore, such diagnostics may also be used, along with relevant modeling, to extend to prognostics health management (PHM), which emphasizes predicting the future state with uncertainties also quantified [145]. Diagnostics may be thought of as a current snapshot of the structure's condition can be exploited to propagate anomaly in the time domain, and modeling and uncertainty quantification may be used to propagate the current state into the future so that comparison to potential limit states (e.g., critical damage) may be performed. In this way, PHM can provide information to support optimal maintenance and life-cycle management [156, 151].

The overall SHM and prognostics strategy is shown in Figure 1.2. The strategy can be roughly divided into two parts, i.e., diagnostics (on the bottom, in orange color) and prognostics (on the top, in green color), despite the intricacy and interconnection among all components. The prognostics starts with an offline physics-based model. The physics-based model, often a finite element model (or models), simulates the known physics of the system, including how external loads and other inputs induce system responses, and incorporates deterioration model(s) for whatever deterioration/damage mode(s) are of interest. The interactions between system inputs, degradation processes (like corrosion considered here), and their effects on the structural behavior are often extremely complex, require multi-physics simulation, and/or require high-fidelity modeling; such is the case for corrosion, where finite element structural modeling must be coupled to systems of partial differential equations (PDEs) that describe the corrosion physics.

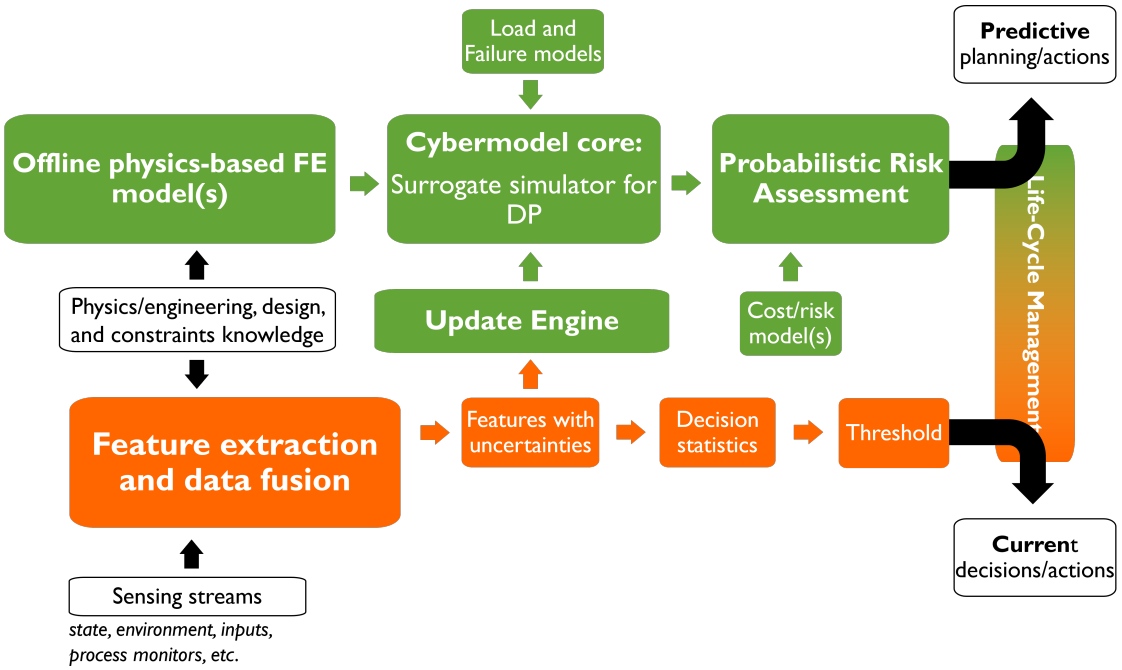

Figure 1.2. SHM and prognostics overall strategy

Inevitably, this complexity and fidelity makes running the model(s) computationally expensive, which can preclude use of the models for real-time prediction or probabilistic assessment, as such an assessment would require the model(s) to be run many times over all the uncertain parameters. Consequently, a run-time surrogate model, referred to as the "cybermodel" in Figure 1.2, must be built, usually from machine learning architectures. Based on this fast surrogate emulator, probabilistic predictions can be made as part of a risk assessment that integrates cost/risk models. The cost/risk models incorporate regulations, codes, liability and business models to inform future maintenance planning or other limit-state actions.

The diagnostics starts with sensing streams that sample structural response, environment, loads, and/or any operating process. Different sources of measurement data may be combined with data fusion engine. The data may be used to update various physics-based model parameters directly and further mined for damage-sensitive features via signal processing, machine learning, or other techniques. These features effectively become proxies of the damage state that are then used to update the prognostic model suite described previously, and this cycle repeats over

time as new data are obtained. Adaptive statistical modeling of the features helps to formulate a hypothesis test to decide whether the feature changes are critical or not by coupling to the cost/risk models. Current maintenance other performance-related decisions may be made by comparing the current features with the cost/risk-informed threshold.

Previous studies have been done applying SHM and prognostics for pitting corrosion, a number of which are summarized in the Section 1.2.2 and Section 1.2.3.

1.2.2 SHM for Corrosion

Different characteristics of pitting corrosion are relevant. Pit depth represents the maximum depth of a local corrosion site. The corresponding pitting depth factor is defined as the pit depth divided by the average penetration based on uniform corrosion [56]. The cross-sectional area loss is often used to describe the corrosion growth of reinforcement steel in reinforced concrete structures. The associated pitting area factor is defined as the ratio between the minimum cross-sectional area and the area based on uniform corrosion [163]. Volume loss is another commonly used metric for corrosion growth. Since corrosion is considered an electrochemical process, other features related to this are relevant. The corrosion current density describes the amount of charge per unit of time that flows through a unit area of a chosen cross-section. The corrosion current density is also called corrosion rate and is related to the thickness reduction rate in uniform corrosion [50]. Pitting corrosion current density is defined by multiplying a coefficient and the maximum pit depth. It is usually approximated with a linear relation with current density [138].

To characterize corrosion and evaluate the condition without affecting the structural state, nondestructive evaluation techniques (NDT) are applied to monitor and evaluate the pitting corrosion including visual inspection, acoustic techniques, electromagnetic techniques, electrochemical-based techniques, and indirect environment monitoring. Visual inspection facilitated by a trained inspector represents the most straightforward and common technique for detecting corrosion in civil infrastructure. This approach remains a fundamental practice

in maintenance procedures. Recent advancements in mobile scanners and robots equipped with cameras have rendered this method more effective and accessible. However, despite these advancements, there are still situations where corrosion persists undetected, particularly in areas that are difficult to access. More recently, computer vision-based methods have emerged as a promising avenue for inspection and have garnered significant attention in research [19, 2].

Acoustic and ultrasonic techniques have been effectively utilized in measuring corrosion damage. Ultrasonic Testing (UT) scans over a surface produce a thickness mapping of the area. However, the resolution is often insufficient to accurately capture the relatively small thickness loss in corrosion. Guided Waves (GW) have also been explored for corrosion detection. Sicard et al. [135, 133, 134] applied the Synthetic Aperture Focusing Technique (SAFT) for Lamb waves to detect pitting corrosion. Bingham et al. [17] extracted features using the Dynamic Wavelength Fingerprint technique to identify regions of corrosion and thickness loss. Nonetheless, the transducers used in the GW approach described above can be bulky and challenging to mount on actual structures. Several researchers have studied the Acoustic Emission (AE) from steel corrosion [25, 130]. However, the challenge of denoising persists for many corrosion phenomena in real-life environments, making the identification of corrosion location a continuing challenge.

Electromagnetic techniques are also employed in the detection of corrosion. Eddy Current (EC) testing operates based on the principles of electromagnetic induction, detecting defects through impedance changes [123, 71]. Conventional EC techniques can sometimes face challenges in imaging the gradual thinning resulting from corrosion. However, the use of multiple frequencies can aid in measuring several parameters simultaneously, enabling the estimation of small changes in thickness [122, 4]. Infrared thermography (IRT) allows the recording of electromagnetic waves emitted from objects by using an infrared imaging system. Marinetti et al. [101] demonstrated detection of hidden corrosion in steel plates. Jonsson et al. [76] showed the capability to detect blisters and filiform corrosion. However, the efficacy for local corrosion such as pitting appears to be quite limited.

Indeed, techniques such as linear polarization resistance (LPR), electrochemical noise

analysis (ENA), and electrochemical impedance spectroscopy (EIS) are well-established in laboratory settings. However, applying these methods for in situ measurements on actual structures is often not feasible.

Another approach to monitoring corrosion more indirectly involves tracking environmental parameters such as temperature, humidity, pH, chemical species in solutions, among others. However, for civil infrastructure, the surrounding areas are often extensive and exposed to the environment. Consequently, detecting environmental changes attributable to local corrosion is not always practical. For civil infrastructure, the threshold is more difficult than other structures due to the lack of the failure cases. For local damage like pitting corrosion, the assessment is even harder as it happens in small area in a large complex structure.

1.2.3 Corrosion Prognosis

Various data-driven approaches have been explored for corrosion prognostics. These methods primarily rely on historical data for making predictions, operating without a physics-based model of damage evolution. Damage prognosis, relying on features or inspection data, has been addressed through various statistical methods. These include multi-step adaptive Kalman filtering [82], stochastic auto-regressive integrated moving average models [73], Weibull models [59], and particle filter methods [110]. Each method contributes to predicting the progression of damage based on specific statistical principles. In situations where the sensor network is inadequate or the level of criticality doesn't warrant a high prognostic accuracy cost, a statistical experience-based prognostic approach is suitable. This method involves gathering inspection history data and fitting a statistical failure distribution, such as the Weibull distribution, to the data [59, 129]. Even a straightforward statistical prognostic distribution can still enhance traditional time-based maintenance approaches. For slow degradation types under similar loading conditions, trend-based prognostics is applied to monitor and analyze the deviations in specific features or measurements. However, it necessitates ample information for measurement, as relevant features must be extracted accurately from the measurements [45]. This method forecasts future features

by observing detectable deviations.

In addition to statistics-based prognostics, machine learning-based prognostics have gained popularity in the realm of data-driven prognostics, leveraging the rapid advancements in machine learning algorithms in recent years [166]. Gobel et al. [54] conducted a comparison between Gaussian progress regression (GPR) and neural networks (NN), using the same damage data for training. Ossai et al. [112] applied various fundamental ML algorithms, including principal component analysis (PCA), particle swarm optimization (PSO), feed-forward artificial NN (FFANN), gradient boosting machine (GBM), random forest (RF), and deep NN (DNN), for estimating corrosion defect depth growth. Susto et al. [141] proposed a multiple classifier machine learning (ML) methodology for predictive maintenance. Zhao et al. [167] uses a back propagation neural network to predict the remaining useful life (RUL) of the aircraft engine. Li et al. [88] applied deep convolutional neural network (DCNN) to predict the RUL on aero-engine degradation dataset. Dourado et al. [40] incorporated a physics-informed layer based on the Paris law into their model for corrosion-fatigue prognostics. These studies showcase the diverse applications of ML in predicting damage progression.

Most data-driven methods require historical failure data, as statistical algorithms lack an understanding of physical failure mechanisms. However, such failure data is often scarce or even absent for civil infrastructure, and generating it through reasonable approaches proves challenging. Given these constraints, there is a strong inclination towards physics-based prognostics for civil infrastructure. Another distinction lies in the fact that the Data-Driven approach heavily relies on measurements with minimal consideration of underlying physics [165]. In contrast, the model-based approach can offer estimates even in the absence of measurements. Furthermore, when diagnostic information becomes available, the model can be refined or updated based on this additional information.

Empirical pitting corrosion growth models have been investigated by multiple scholars. Empirical models are typically derived from historical observations rather than from established physics theories. For example, power-law models have been proposed to characterize the

variability of corrosion growth, with the time-variant corrosion depth represented as a constant power of time [79]. Various empirical formulas have also been developed to describe the evolution of the pitting depth factor [139], the pitting area factor [163], and the corrosion current density [140]. Some empirical equations also account for environmental factors that might influence corrosion growth [26].

A physics-based model is used to understand how damage progresses in components. These models help calculate damage to critical components based on operational conditions, allowing for a detailed assessment of the cumulative effects on component life usage. By combining physical and stochastic modeling techniques, these models can analyze remaining useful life distribution, considering uncertainties from component strength/stress properties, loading, or other operating conditions. This approach provides a comprehensive understanding of how components behave and their reliability under various conditions.

In physics-based models for pitting corrosion, Faraday's law is one of the most widely used principles. According to Faraday's law, the pit is assumed to grow at a constant volumetric rate, as follows [65]:

$$\frac{dV_o}{dt} = \frac{MI_{\rho^0}}{nF_r\omega} \exp\left(\frac{-\Delta H}{RT}\right), \tag{1.1}$$

where V_o is the volume of the metal, M is the molecular weight, n is the valence, F_r is the Faraday's constant, I_{ρ^0} is the pitting current coefficient, ω is the density, ΔH is the activation enthalpy, R is the universal gas constant, and T is the absolute temperature. The exponential term is introduced to take the effect of temperature into consideration.

To address uncertainty in both empirical models and physics-based models, the model parameters of the aforementioned approaches are often treated as random variables, characterized by probability distributions such as normal, lognormal, Weibull, and Gumbel distributions [55, 125, 132]. In addition to representing the corrosion growth metric as a deterministic function of random variables, stochastic processes can also be utilized for probabilistic corrosion modeling. Commonly employed stochastic process models include the Gamma process, Poisson square

wave process, Markov chain process, and other similar stochastic processes [55, 14, 147, 119].

When physics-based models such as the phase-field model are employed for failure forecasting, various sources of aleatory uncertainty (e.g., material properties, load conditions, etc.) in the simulation model need to be considered [70]. Proper consideration usually requires many (thousands or more) evaluations of the high-fidelity simulation model [116, 117], particularly if a Monte Carlo simulation (MCS)-based method is adopted. However, most physics-based models are computationally very expensive due to multiple coupled nonlinear partial differential equations (PDE). Advanced uncertainty quantification or reliability analysis methods are therefore usually needed to tackle the computational challenge. Among existing uncertainty quantification or reliability analysis methods, MCS based on surrogate modeling is one of the most widely used. In such a strategy, a computationally cheaper yet accurate surrogate model is first constructed to replace the computationally expensive computer simulation models. MCS is then conducted using the surrogate model to quantify the distribution of features of interest (e.g., corrosion depth, shape) or predict the probability of failure (limit state analysis) [69].

Multiple approaches have been made in recent years to build surrogate models emulating phase-field simulations. For instance, Shen et al. [131] used the least square regression (LSR) and the back-propagation neural network (BPNN) to produce an analytical expression for the breakdown strength based on phase-field simulation data. Eduardo et al. [37] utilized k-nearest neighbor (k-NN) and artificial neural networks (ANN) algorithms to detect the presence and location of failure based on simulation data. For time-dependent processes, Montes et al. [103] applied a long-short-term (LSTM) network to perform microstructure evolution predictions as the surrogate model of the phase-field simulation. The principal component analysis (PCA) technique was applied for dimension reduction; however, the reconstructed microstructure from the LSTM-trained surrogate model had a considerably noisy boundary. Nevertheless, in the corrosion simulation, the boundary between the corroded material and the solution is of main interest. Qian et al. [118] implemented a convolutional neural network with Gaussian process regression imbued with a nonlinear autoregressive exogenous structure (CNN-GP-NARX) network. In

that work, a CNN-Autoencoder is trained to map between the high-dimensional image space and the low-dimensional latent space. The mean values of prediction are accurate, but there are some spurious corrosion shapes because of the uncertainty in the prediction. Even though these data-driven surrogate models show great potential in overcoming the computational cost for probabilistic physics-based failure forecasting, their accuracy may be significantly affected by the training data, and the prediction sometimes may violate physical law due to the limited amount of training data. Nejera et al. [104] implemented physics constraints in the surrogate models to increase the accuracy and reduce the uncertainties in the prediction by modifying the loss function.

1.3 Research Needs, Objectives, and Contributions

While pitting diagnostics and prognostics have undergone extensive investigation due to the ubiquitous nature of corrosion, certain challenges persist in current state of the art.

- First, the noticeable scale of pitting corrosion is in the millimeter range, whereas civil infrastructure typically span tens to hundreds of meters, introducing a multi-scale complexity that complicates both diagnostics and prognostics. The scale disparity between structures and the unpredictable outdoor environment renders many traditional corrosion assessment approaches impractical for diagnosis, and physics-based models struggle to maintain the same fidelity across different scales in prognosis.

- Second, advanced physics-based models pose computational challenges for prognostic predictions, requiring numerous runs for uncertainty propagation.

- Third, the crucial and dynamic loading condition of mechanical stress in civil infrastructure has not been adequately integrated into current diagnostic and prognostic methods.

In exploring pitting corrosion within civil infrastructure, it is imperative to establish a linkage between mesoscale corrosion simulations and macroscale structural simulations. Moreover,

the implementation of computationally intensive simulations for prognosis with uncertainties is not practical. Additionally, traditional sensing technologies are unsuitable for deployment in civil infrastructure. To tackle these challenges, the objectives of this thesis are as follows:

- Establish a connection between mesoscale corrosion simulation and macroscale structure simulation through a multi-scale simulation approach.
- Construct surrogate models to expedite physics-based simulation, facilitating probabilistic analysis and reliability assessment.
- Create a pitting corrosion diagnosis framework for civil infrastructure, utilizing strain measurements and images. Subsequent prognostics will be carried out with the model updated based on the diagnosis results.

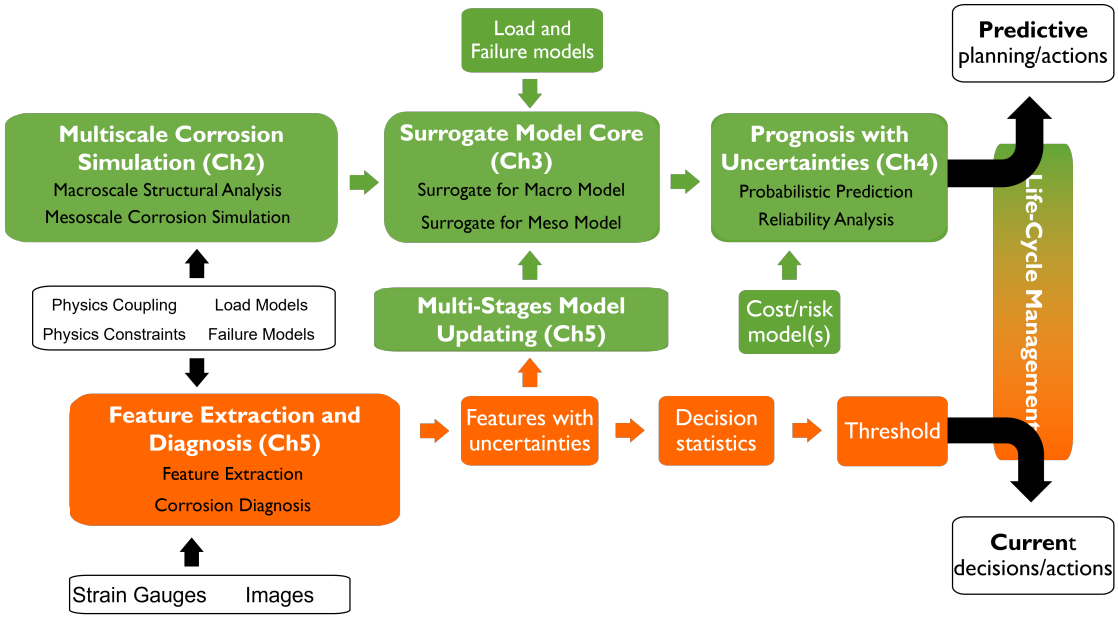

Figure 1.3. Proposed diagnosis and prognosis framework for pitting corrosion in civil infrastructure

To realize these objectives, there are four chapters in this thesis to develop and exemplify the approach. Chapter 2 presents a multi-scale simulation with the local PF corrosion simulation one-way coupled with the structural level finite element (FE) simulation. Chapter 3 explores

different surrogate modeling techniques based on machine learning (ML) for the multi-scale simulation proposed in Chapter 2. Chapter 4 shows a reliability analysis framework for SCC initiation with an adaptive surrogate modeling technique based on the surrogate models proposed in Chapter 3. Chapter 5 presents a diagnosis framework with the combined measurements from strain gauge as well as the images. A multi-stages model updating technique is developed to update the predictive model. Figure 1.3 summarizes the major components for diagnostics and prognostics for pitting corrosion in civil structures in this thesis.

The contributions are summarized as:

- Development of a multi-scale simulation connecting a mesoscale high-fidelity PF corrosion simulation with a macroscale FE simulation. Modifying the PF simulation to simulate the corrosion evolution under different static and dynamic stress conditions.
- Development of ML-based surrogate model for the physics-based computational model to accelerate the forward simulation.
- Quantification of epistemic uncertainties in the corrosion evolution prediction. Development of a reliability analysis approach with adaptive surrogate modeling technique and the adaptive importance sampling (IS) technique.
- Diagnosis of pitting corrosion with images with a multi-stage model updating approach.

Chapter 2

Physics-Based Multi-Scale Corrosion Simulation

2.1 Introduction

Stress corrosion and stress corrosion cracking (SCC) damage have been significant types of deterioration in large civil infrastructure [96, 33]. Over decades of service, components are exposed to variable service loads and a changing natural environment at the same time. Such operational and environmental loading has significant influence on the evolution of local pitting corrosion [99] and SCC initiation, which may ultimately lead to structural failure.

The phase-field method is a powerful mesoscale method to analyze the spatiotemporal evolution of microstructure. This method can be extended by coupling with an electrochemical reaction model to simulate the phase evolution in the corrosion process. The phase change is described by a continuous variable such that an explicit treatment of the interface may be avoided. LQ Chen proposed a phase-field for microstructure evolution [30]. Nonlinearity is introduced to this model by considering the chemical reaction kinetics [91]. Multiple applications of the phase-field method on corrosion have been proposed and studied [99, 8, 93, 109, 126, 21, 28]. Mai et al. [99] proposed a phase-field model to simulate pitting corrosion. Local free energy was described with the Kim-Kim-Suzuki (KKS) model [80]. However, the electrical potential distribution for ion concentration was not considered. Ansari et al. [7] took the influence of insoluble corrosion products into consideration in phase field corrosion modeling. Chen et al.

[95] coupled mechanical influence to the electrochemical system by multiplying an interpolation function of the order parameter with the original mechanical energy. The mechanical term in the electrochemical potential that was calculated similarly by taking variation of total free energy was a square term of the elastic strain tensor. Chen et al. [93] also involved mechanical effect coupled with galvanic influence. The change of chemical potential of electrode due to mechanical deformation is considered as the sum of mechanical energy density and mechanical potential. All current attempts for coupling mechanical influence into phase field corrosion modeling led to a similar behavior under tensile or compressive stress. Nevertheless, multiple experiments showed obvious differences between the corrosion under tensile and compressive stress [107, 108, 164]. Such differences between tensile stress and compressive stress is rarely studied or discussed in the phase-field modeling area, and it will be one aspect considered in this work.

Stress corrosion cracking (SCC) was also simulated with the phase-field method. Mai et al. [98] modified the kinetics parameter term by assuming a linear relationship with the SCC growth velocity. Nguyen et al. [109] took ion concentration and elastic energy densities into consideration in total free energy. However, the transition from corrosion to crack and the relationship between crack initiation and applied mechanical load has not been studied yet. More crucially, multiple experimental data show that the uncertainties at the crack initiation stage is obviously higher than during the stable propagation stage [28, 80]. A probabilistic analysis framework which can take the uncertainty sources at the crack initiation stage into consideration is thus an important gap to fill, and this is also addressed in this work.

However, implementing such corrosion simulation on the civil structures is challenging because the scale difference.The noticeable scale of pitting corrosion is in the millimeter range, whereas civil infrastructure typically span tens of meters, introducing a multi-scale complexity that complicates simulation. The physics-based models struggle to maintain the same fidelity across different scales. To address this concern, we proposed a multi-scale corrosion simulation approach as Figure 2.1 shows. This approach includes a mesoscale corrosion simulation, a

macroscale structural analysis and a statistical method for pit initiation modeling. An electro-chemo-mechanical phase-field model coupled with mechanical stress is also developed based on the generalized chemical potential. This model can capture the influence of different kinds of mechanical loading (tensile, compressive, and shear stress) on pitting corrosion growth, by embedding the stress term into the overpotential in the Butler-Volmer equation. A SCC initiation criterion based on a Von-mises limit state is proposed and compared with the other SCC initiation criteria [94] based on the Tsujikawa–Kondo condition [81].

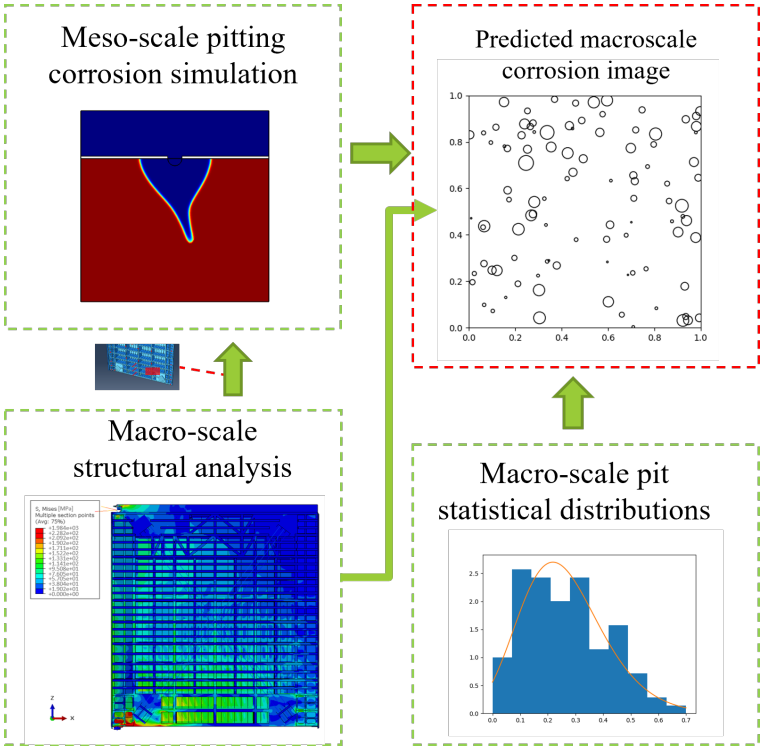

Figure 2.1. Schematics of multi-scale pitting corrosion simulation

The remainder of this chapter is organized as follows: Section 2.2 introduces the macroscale structural analysis with dynamic load; Section 2.3 presents the pitting corrosion simulation using a phase-field model, pit-to-crack transition analysis, calibration, and the stress influence on corrosion evolution and stress corrosion cracking initiation. Finally, Section 2.4 concludes and discusses the presented work in the chapter.

2.2 Macroscale Structural Analysis

2.2.1 Stochastic Load Condition Modeling

The structure of interest in this work is the Greenup miter gate located in Kentucky, USA. The water elevation on both sides of the Greenup dam is monitored every fifteen minutes by the United States Geological Survey [1]. In order to model the water levels, the water level monitoring data is decomposed into the trend, seasonality, and noise [114] with moving average. However, the monitoring data show almost no regular seasonal pattern in the series as Figure 2.2 shows. Thus, the water level time series data is decomposed mainly into the trend and noise two parts.

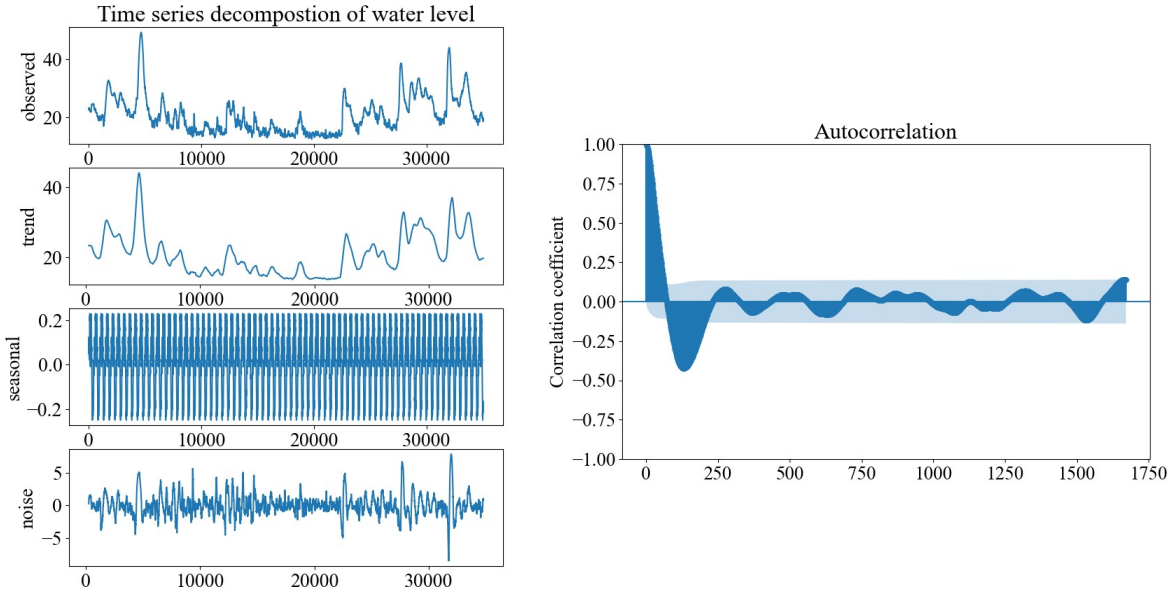

Figure 2.2. Time series decomposition for water level monitoring data (left) and autocorrelation plot of noise component (right)

After that, the water level is modeled as a second-order stochastic process using the Karhunen–Loeve expansion method as below [146]

$$h(t) = \mu(t) + \sigma(t) \sum_{i=1}^{N} \sqrt{\lambda_i(t)} \xi_i \eta_i(t), \tag{2.1}$$

in which $\mu(t)$ is the mean of the process and is the trend component from the decomposition; $\sigma(t)$ is the standard deviation calculated from noise component; $\lambda_i(t)$ and $\eta_i(t)$ are the eigenvalues and the associated eigenvectors obtained from eigendecomposition of the autocorrelation matrix obtained with the noise component and the correlation function is shown in Figure 2.2; ξ_i is a set of uncorrelated standard Gaussian random variables.

Based on the stochastic modeling of the water level, different realizations of water level time series data can be generated with the KL expansion.

2.2.2 Macroscale Structural Analysis

To simulate the stress response of the structure under varying water levels, a high-fidelity linear finite element model of a large infrastructure, the Greenup miter gate, is utilized. This finite element model, as shown on the left side in Figure 5.8 has been validated in the previous study [44]. The structure is discretized with 64919 shell elements. The model is capable of simulating the structure behavior under different water elevations on both sides.

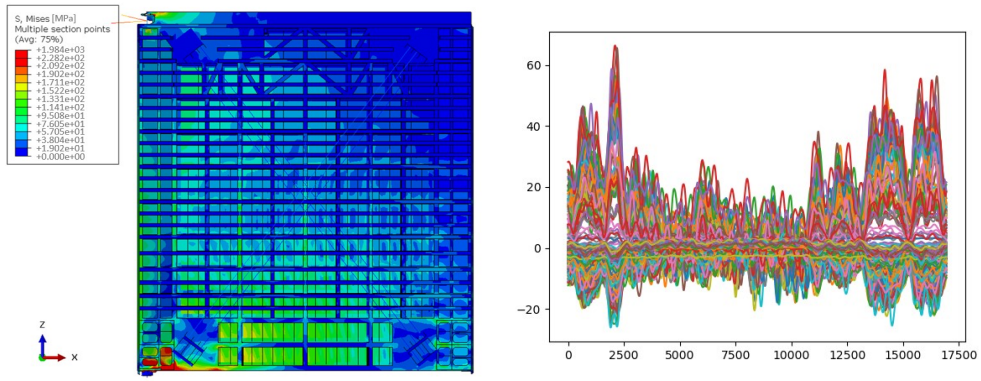

Figure 2.3. Miter gate finite element model (left) and the stress values of locations selected (right)

The stress distribution is complex in such large infrastructures. However, a limited number of stress responses can be simulated in the corrosion model due to computational cost. Therefore, two hundred locations within different average stress ranges are selected to represent

the stress response on the entire structure. Specifically, the stress responses under one hundred time-series realizations of KL-expansion water levels are simulated and averaged over different realizations and time series. Positions on the gate are then grouped by different stress ranges for the selection. The right side plot on Figure 5.8 shows the stress value of the locations selected.

2.3 Mesoscale Pitting Corrosion Modeling

2.3.1 Stress corrosion and SCC mechanism

The stress corrosion process, as shown in Figure 2.4, starts from the local breakage of the passive film. Under a corrosive environment, the metal is corroded and produce cations (M^+) into the electrolyte as well as the electrons in the electrode. During service life, complex mechanical loading conditions typically occur in different locations. However, mechanical loading changes the chemical potential of the electrode (metal), affecting the corrosion process. Stress concentration at the tip of the pitting corrosion amplifies the influence from the mechanical stress. In order to properly quantify the contribution from mechanical load, a generalized potential is introduced.

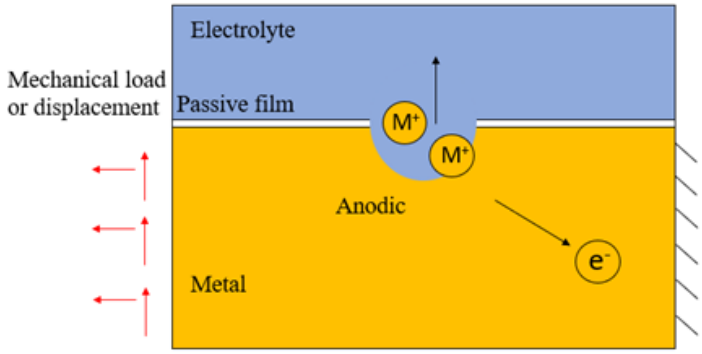

Figure 2.4. Schematics of stress corrosion

2.3.2 Statistical Modeling of Pit Initiation Time and Location

To facilitate the simulation of multiple pit evolutions on the macro structure, we introduce a multi-scale simulation approach that establishes a connection between mesoscale single pit

simulations and the macroscale structure.

For simulating multiple pits based on the behavior of a single pit at the local level, obtaining information about multiple pit initiation times and locations is crucial. Pit initiation stems from the breakdown of the local passive film, a process involving intricate mechanisms of nucleation and early propagation, currently under active research [51, 83, 84, 86, 87].

Given the complexity of these mechanisms, we resort to statistical information to describe this stage. The passive film breakdown event is modeled as a nonhomogeneous Poisson process [12], and the Weibull distribution has been identified as a suitable fit for the pit initiation time distribution [11, 89].

2.3.3 Generalized chemical potential and kinetics in corrosion system with mechanical stress

The generalized chemical potential in the electrochemical system is expressed as

$$\mu = \mu_t + \mu_{el} + \mu_{gr} + \mu_{me'} \tag{2.2}$$

where μ is the well-defined chemical potential, μ usually consists of thermal potential μ_t, electrical potential μ_{el}, gradient energy density or gradient potential μ_{gr}, and mechanical energy density or mechanical potential μ_{me}.

The influence of mechanical deformation on corrosion process originates from the potential change due to mechanical deformation on the surface of the solid [63, 62]. According to Gibbs–Duhem equation [38], the differential of chemical potential dependence is described as

$$\sum_i N_i d\mu_i = -SdT + VdP \tag{2.3}$$

where N is molarity, V is the volume, S is the entropy, T is the temperature and P is the pressure, calculated with hydrostatic stress by $P = -\frac{1}{3}\sum_{k=1}^{3}\sigma_{kk}$

Assuming the metal response is linearly elastic [127], the linear expression for μ_{me} by

integrating Equation 2.3 follows expression in mechanochemistry area by Gutman [63, 62]

$$\mu_{me} = \int_{P_1}^{P_2} V(P)dP \approx \Delta P V_{m'} \tag{2.4}$$

where P_1,P_2 are the initial and end pressure and V_m is the molar volume.

The thermal potential is expressed as

$$\mu_t = g(\bar{c}) + c_0 RT(\bar{c}_+ \ln \bar{c}_+ + \bar{c}_- \ln \bar{c}_-) + \sum_i c_i \mu_i^{\Theta} \tag{2.5}$$

Where $\mathbf{c} = \{c, c_+, c_-\}$ is a set of concentrations for the metal atom, metal cations, and electron, respectively. Further, $\bar{c}$ is defined as the set of dimensionless concentrations as $\{c_- = \frac{c}{c_s}, \bar{c}_+ = \frac{c_+}{c_0}, \bar{c}_- = \frac{c_-}{c_0}\}$, where c_s is the site density of the metal iron and c_0 is the bulk concentration of electrolyte solution, R is molar gas constant, and T is the temperature. The double-well function $g(\bar{c}) = W\bar{c}^2(1-\bar{c})^2$ is used to describe the transition between electrode ($\bar{c} = 1$) and electrolyte ($\bar{c} = 0$). W represents barrier height of corrosion. μ_i^{Θ} is the reference chemical potential of spices i.

The electric potential μ_{el} is expressed as

$$\mu_{el} = \rho_e \phi \tag{2.6}$$

where ϕ is the electrostatic potential, ρ_e is the charge density which can be expressed as $\rho_e = F z_i c_i$ where F is Faraday's constant, z_i is the valence and c_i is the concentration of species i.

The interfacial potential μ_{gr} is given by taking partial derivative of the interface energy as [91]

$$\mu_{gr} = g'(\bar{c}) - \kappa \nabla^2 \bar{c} \tag{2.7}$$

where κ is interface coefficient.

According to previous formulation of electrochemical reaction kinetics, the reaction rate, R_e of corrosion is expressed as the difference between forward ($S_1 \rightarrow S_2$) and backward ($S_2 \rightarrow S_1$) reactions in a form of Butler–Volmer equation as

$$R_e = k_0(\exp[\frac{-(\mu_t^{ex} - \mu_1)}{RT}] - \exp[\frac{-(\mu_t^{ex} - \mu_2)}{RT}]) \tag{2.8}$$

where μ_1 and μ_2 refers to the total chemical potential at state 1 and state 2 respectively, μ_t^{ex} is the activation barrier, k_0 is the reaction constant.

Based on the potentials Equation 2.2-2.7 we defined previously, we can get the potential expressions of initial state 1 (electrode) and later state 2 (electrolyte) by different components in the corrosion reaction, $M \rightarrow M^{n+} + ne^-$

$$\mu_1 = \mu_M = \mu_M^t + \mu_M^{me} + \mu_M^{gr} = \mu_{gr} + \mu_M^{\Theta} + \mu_{me} \tag{2.9}$$

$$\mu_2 = \mu_{M^{n+}}^t + n\mu_{el} = RT\ln a_{M^{n+}} + \mu_{M^{n+}}^{\Theta} + nF\phi_s + nRT\ln a_e + n\mu_e^{\Theta} - nF\phi_e \tag{2.10}$$

where ϕ_s and ϕ_e are the electrostatic potential in the solution and the electrode respectively, a_M, $a_{M^{n+}}$ and a_e are the activities of the components. The activity for electrons is unity assuming that the electrolyte solution is dilute. The interfacial potential difference is $\Delta\phi = \phi_e - \phi_s$. At the equilibrium, the potential difference $\Delta\mu = \mu_2 - \mu_1 = 0$ according to the Nernst equation

$$\Delta\phi^{eq} = \frac{\mu_{M^{n+}}^{\Theta} + n\mu_e^{\Theta} - \mu_M^{\Theta} + RT\ln c_+^- + \mu_{me} - \mu_{gr}}{nF} \tag{2.11}$$

Outside equilibrium, the reaction is driven by the overpotential, η, which is defined as

$$\eta = \Delta\phi - \Delta\phi^{eq} \tag{2.12}$$

Substituting Equation 2.12 with Equation 2.11, η is expressed as

$$\eta = \Delta\phi - \frac{\mu^{\Theta}_{M^{n+}} + n\mu^{\Theta}_{e} - \mu^{\Theta}_{M}}{nF} - \frac{RT\ln \bar{c_{+}} - \mu_{gr}}{nF} + \frac{\mu_{me}}{nF} \tag{2.13}$$

where the second term represents the standard potential difference between reactants and products, the third term expresses the concentration overpotential, and the third term is the influence of mechanical elastic energy density. The total overpotential can be separated into activation overpotential $\eta_a = \Delta\phi - \frac{\mu^{\Theta}_{M^{n+}} + n\mu^{\Theta}_{e} - \mu^{\Theta}_{M} + \mu_{me}}{nF}$, concentration overpotential $\eta_c = \frac{RT\ln \bar{c_{+}} - \mu_{gr}}{nF}$.

The excess electrochemical potential in the transition state is defined as [15]

$$\mu^{ex}_{t} = RT\ln\gamma_t + \mu^{ex}_{me} + (1-\alpha)\mu^{\Theta}_{M} + \alpha(\mu^{\Theta}_{M^{n+}} + n\mu^{\Theta}_{e}) \tag{2.14}$$

where γ_t is the activity coefficient at the transition state, μ^{ex}_{me} represents the mechanical potential at the transition state, and α is an approximate constant ranging from zero to one called symmetry factor.

The reaction rate can be expressed by substituting Equations 2.9 to 2.14 into Equation 2.7

$$r = \frac{k_0}{\gamma_t}\exp(-\frac{\mu^{ex}_{me}}{RT}) \times \{\exp(\frac{\mu_{gr} + (1-\alpha)\eta_a}{RT} - \bar{c}_{+} exp(\frac{-\alpha nF\eta_a}{RT})\} \tag{2.15}$$

The influence of the interfacial potential concentration gradient at the interface on the corrosion process is usually small comparing to other components in the total chemical potential [29]. A nonlinear relationship for phase transforming is proposed by Liang et al. [91, 143] as

$$r = -L_\sigma(g'(\bar{c}) - \kappa\nabla^2\bar{c}) - L_\eta(\exp(\frac{(1-\alpha)\eta_a}{RT}) - \bar{c}_{+} exp(\frac{-\alpha nF\eta_a}{RT})) \tag{2.16}$$

where $L_\sigma = \frac{k_0}{RT\eta_t c_s} exp(-\frac{\mu^{ex}_{me}}{RT}) exp(\frac{(1-\alpha)\eta_a}{RT})$ represents interfacial mobility and $L_n = \frac{k_0}{\eta_t} exp(-\frac{\mu_{\mu_{me}}}{RT})$ represents a reaction coefficient. In the work, we assume the reaction coefficient is a constant value which will be calibrated in Section 4.1.

2.3.4 Governing equations for corrosion with stress

A continuous order parameter ξ is introduced to describe the diffuse interface in the proposed phase field model. The order parameter physically corresponds to the dimensionless concentration of the metal, as $\xi = \bar{c}$. The dimensionless concentration $\bar{c} = 1$ in the metal and $\bar{c} = 0$ in the electrolyte solution.

In this model, we consider the order parameter's evolution is driven by electrochemical reaction rate r. Thus, the driving force can be clearly divided into two parts: the interface energy and the electrode reaction. To describe the electrochemical reaction kinetics at the diffuse interface, an interpolating function $h'(\xi) = 30\xi^2(1-\xi)^2$ is introduced. Notice that the order parameter changes from one to zero for phase evolution in corrosion process. The phase evolution has a negative relationship with reaction rate r. Therefore, the governing equation for the phase evolution is

$$\frac{\partial \xi}{\partial t} = -L_\sigma \left(g'(\xi) - \kappa \nabla^2 \xi \right) - L_\eta h'(\xi) \left(\exp \frac{(1-\alpha)\eta_a}{RT} - \bar{c}_+ \exp \frac{-\alpha n F_r \eta_a}{RT} \right), \tag{2.17}$$

Equation 2.16 indicates that the mechanical deformation changes the total chemical potential with the mechanical potential μ_{me} (in term η_a). If $\mu_{me} > 0$, the mechanical contribution has a positive influence on the corrosion process; if $\mu_{me} < 0$, the mechanical contribution has a negative influence on the corrosion process.

The metal atom is considered as fixed except during diffusion process. The electrochemical reaction provides the source term which depends on the corrosion (metal consumption) process. The diffusion can be described with the Nernst-Plank equation as

$$\frac{\partial \bar{c}_+}{\partial t} = \nabla \cdot \left(D^{eff} \nabla \bar{c}_+ \frac{D^{eff} \bar{c}_+}{RT} n F \nabla \phi \right) - \frac{c_s}{c_0} \frac{\partial \xi}{\partial t}, \tag{2.18}$$

where D^{eff} represents the effective diffusion coefficient as $D^{eff} = D^e h(\xi) + D^s(1 - h(\xi))$, where D^e and D^s are the diffusion coefficients for metal cation in the electrode and electrolyte,

respectively.

The mechanical equilibrium equation is expressed with stress tensor $\sigma = A^e \varepsilon^{eq}$ as

$$\mathrm{div}(\sigma) = 0, \tag{2.19}$$

where the body force is neglected.

It is obvious that fully corroded metal cannot support stress or strain. The equivalent elastic strain tensor considering solid-liquid interface is modified as follows:

$$\varepsilon^{eq} = p(\bar{c}) \left\{ \frac{1}{2} \left(\frac{\partial u_i}{\partial x_j} + \frac{\partial u_j}{\partial x_i} \right) \right\} (i, j = 1, 2, 3), \tag{2.20}$$

where u_i and u_j are displacement components, $p(\bar{c})$ is an interpolation function to smooth the discontinuity in the interface and it also satisfies $p(0) = 0$ and $p(1) = 1$. Combining Equation 2.19 and 2.20, we can get the governing equation for mechanical equilibrium as

$$\mathrm{div} \left(A^e p(\bar{c}) \left\{ \frac{1}{2} \left(\frac{\partial u_i}{\partial x_j} + \frac{\partial u_j}{\partial x_i} \right) \right\} \right) = 0, \tag{2.21}$$

2.3.5 Pit-to-crack transition

Two different SCC initiation criteria are implemented based on the corrosion morphology and the applied mechanical load.

One criterion is based on the Von Mises yield criterion or Tresca yield criterion (which give the same results under a plane strain assumption). The crack is assumed to initiate when the stress reaches the Von Mises yield criterion. Note that this is an approximate conservative criterion for crack initiation

$$\sigma_1 - \sigma_2 = 2\sqrt{\left(\frac{\sigma_x - \sigma_y}{2} \right)^2 + \tau_{xy}^2} < \frac{2Y}{\sqrt{3}}, \tag{2.22}$$

where Y is uniaxial yield stress, σ_y is zero under a uniaxial stress state, σ_x is the normal stress at the tip, and τ_{xy} is the shear stress at the tip. Both σ_x and τ_{xy} at the tip position can be approximated with the stress concentration equation [6]

$$\sigma_x = \sigma_{norm}\left(1+2\sqrt{\frac{a}{\rho}}\right), \tau_{xy} = \tau_{norm}\left(1+2\sqrt{\frac{a}{\rho}}\right), \tag{2.23}$$

where a represents corrosion depth and ρ represents the curvature at the bottom of corrosion pits or potential crack tip position. Both the curvature radius *rho* and corrosion depth a are calculated from the corrosion morphology. From the Equation 2.22-2.23, we can notice that the larger corrosion depth and sharper interfaces are more likely to initiate cracking.

The other SCC initiation criterion is the Tsujikawa–Kondo criterion [81], which compares the corrosion growth velocity with the crack propagation velocity. When the crack propagation speed surpasses the corrosion growth speed, the crack is assumed to initiate. One implementation is based on that the driving force from mechanical stress are separated from that from electrode dissolution [164]. The corrosion speed at pit tip and mouth area of the model are calculated as v_{tip} and v_{mouth} based on the displacement of the interface at pit tip location and the mouth top location, respectively. A parameter $K_v = (v_{tip} - v_{mouth})/v_{mouth}$ is used to evaluate the portion of driving force from mechanical stress. v_{tip} represents the crack propagation speed and v_{mouth} represents the corrosion speed in the crack initiation stage. When the v_{tip} is twice as large as the v_{mouth}, implying the mechanical driving force is much larger than the corrosion without stress, the crack is assumed to initiate. Both criteria are implemented and compared as given in Figure 2.5. Both the approximated Von Mises stress at the tip and parameter K_v are plotted over time. The SCC initiation time is identified when the criterion is met, i.e., the Von Mises stress reaches the yield stress, or K_v reaches two. The proposed SCC initiation criterion is an indicator about the time and location of a possible SCC initiation. The overall trend for these two parameters is similar while the criterion based on the approximated stress is more conservative and stable than that based on corrosion growth speed.

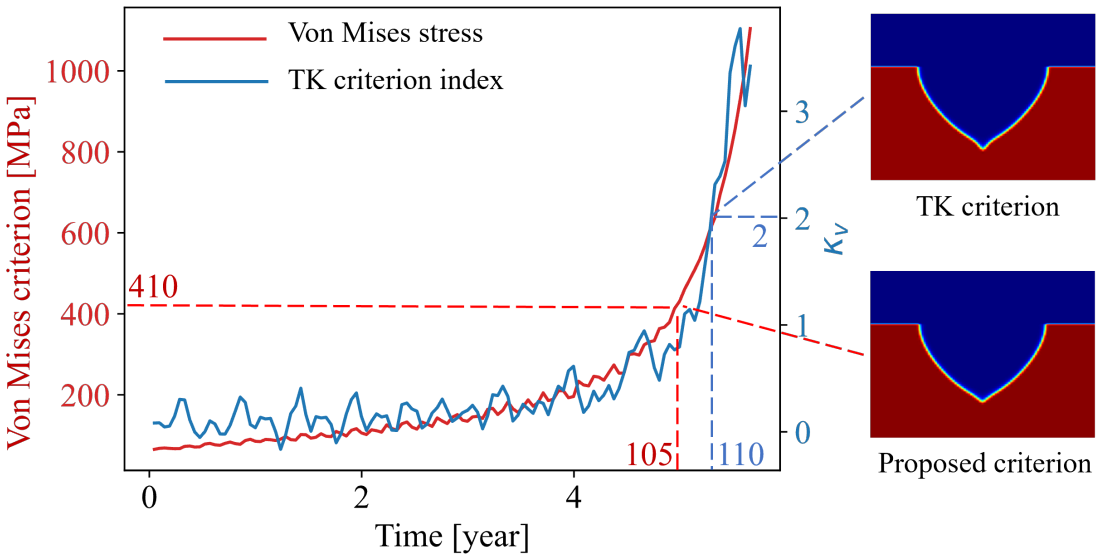

Figure 2.5. Comparation between two crack initiation criteria

2.3.6 Calibration of the phase-field model

The electro-chemo-mechanical phase-field model is calibrated through the measurement data in the literature [29, 113, 22]. In the phase field model for a new system, the reaction constant L_η is usually unknown or unavailable. Here, L_η is calibrated through the measurement of the inner bottom plates of sea-going bulk carriers as shown in Figure 5.3.3. The measured data is not stable because there were some repair and replacement actions going on during the measurement [113]. The different size of the spots represents the number of pits with a certain depth at a certain time. We can notice that changes in the reaction constant greatly affect the corrosion growth. The size of the measurement data point represents the number of pits at certain time with certain depth. The value 40 after normalization, corresponding to $1.3 \times 10^{-7}/s$ is selected for L_η in this work. Details about the normalization of all parameters can be found in the appendix. Other parameters such as gradient energy coefficient and diffusion coefficient are chosen from the literature [29, 22].

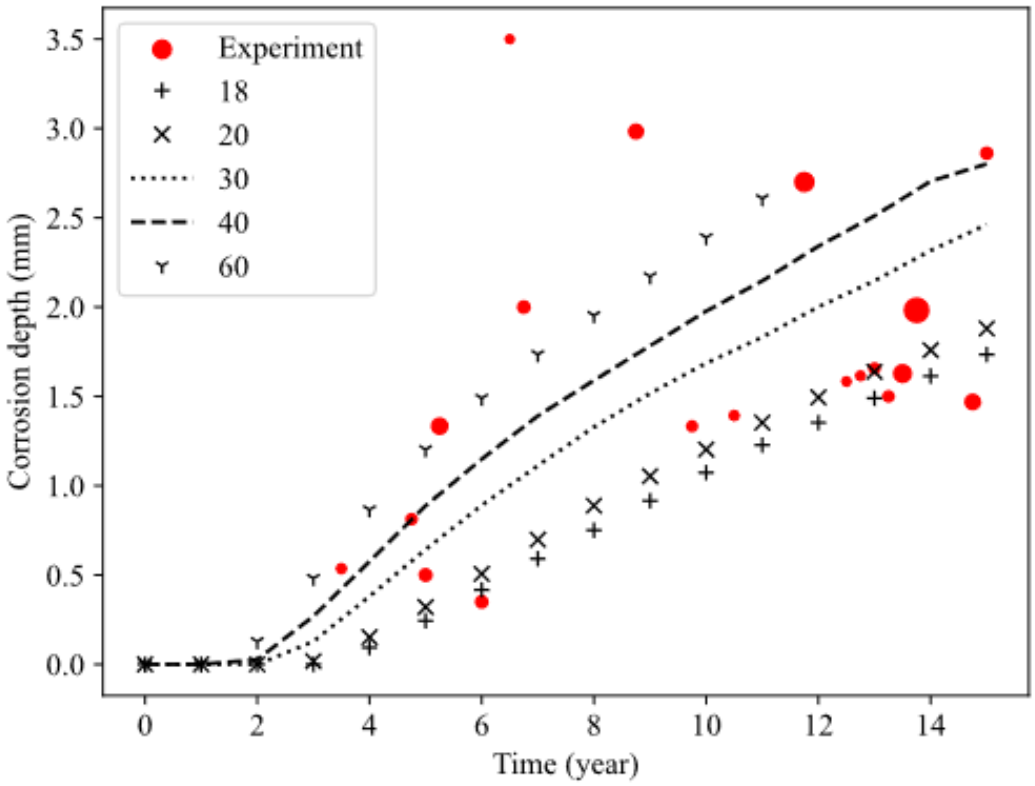

Figure 2.6. Calibration of reaction constant with measurement data

2.3.7 Stress effect on corrosion

The influence of different kinds of mechanical loading on corrosion evolution is considered in this section. Figure 2.7 shows the geometry and boundary conditions of the model. The interface between metal and electrolyte is separated with a layer of non-penetrable passive film except the center semicircle area, which is the initial pit assumed. Normal stress, shear stress with an average magnitude of 50 MPa, and combinations therein are applied to the model because these stress status are common in a miter gate (a type of large civil infrastructure that serves as the underlying structure of interest in this work) in service according to a validated simulation [148] as Figure 2.8 shows. The right surface is fixed. Plane strain is assumed for the model.

Figure 2.9 (a) compares the influence of constant normal tensile stress and compressive stress on the corrosion process. Given applied stress, tensile stress leads to greater corrosion

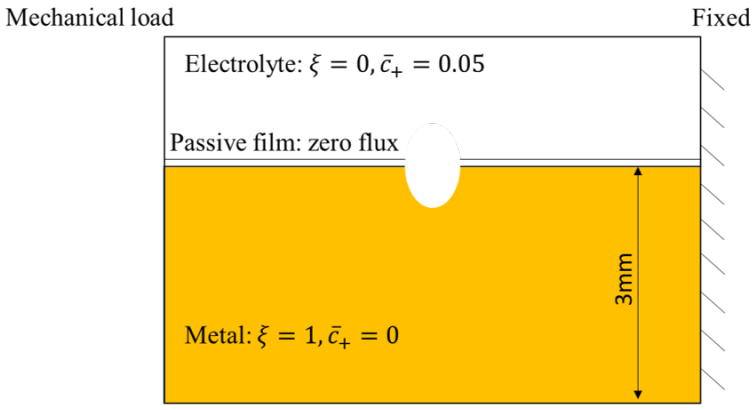

Figure 2.7. Geometry and boundary conditions of the model for stress effect study

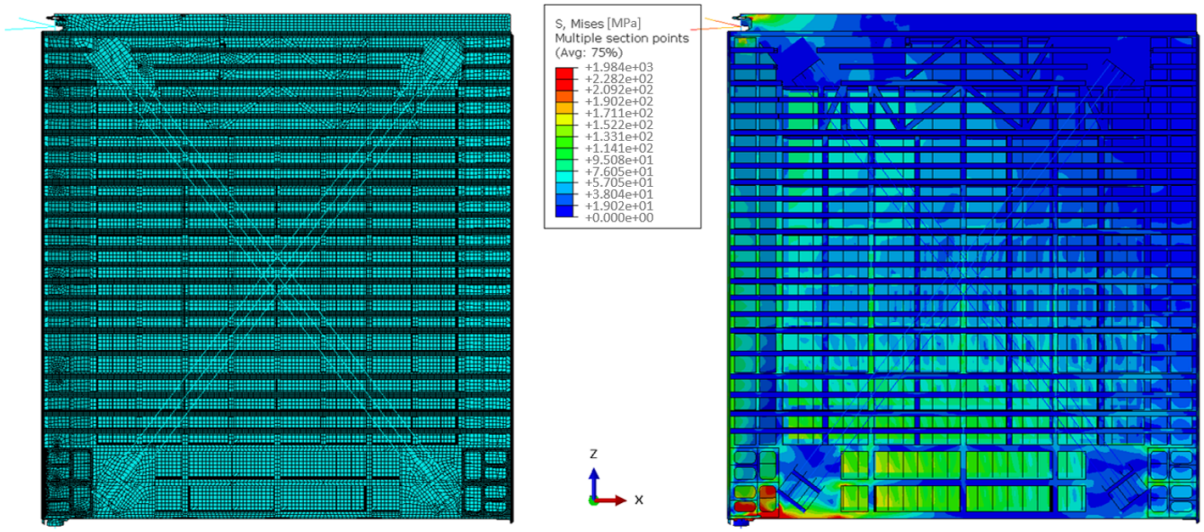

Figure 2.8. Stress magnitude of miter gate simulation

depth while compressive stress results in less corrosion depth. The morphology shows that the tensile stress results in a sharper interface while compressive stress results in a flatter interface. Both cases with tensile stress and compressive stress have stress concentrations because of material loss in the pit evolution. Note that the stress condition affects the corrosion evolution with the hydrostatic stress term in the mechanical elastic energy density as indicated in Equation 2.3. As the corrosion evolves, the absolute value of hydrostatic stress at corrosion tip increases greatly since stress concentration is severe. Therefore, the contribution of mechanical stress is becoming more and more dominant as the stress concentration increases. However, the tensile

stress leads to positive hydrostatic stress while compressive stress leads to negative hydrostatic stress. Large positive hydrostatic stress in the tensile case accelerates the corrosion growth. Because stress concentrates at the pit tip, the tip area has larger positive hydrostatic stress. Thus, corrosion in this area grows faster than in neighboring areas such that the interface becomes sharper. A sharper interface leads to more serious stress concentration. This cycle accelerates the corrosion evolution and fosters potential crack initiation. Conversely, in the compressive case, the negative hydrostatic stress decreases the corrosion growth. As the absolute value of the negative hydrostatic stress increases at the tip area due to stress concentration, the corrosion evolves slower than in other areas. This leads to a flatter interface as the morphology figure shows.

Figure 2.9 (b) shows the influence of constant shear stress on the corrosion evolution. Positive and negative shear stress are applied to the model. Negative shear stress leads to larger corrosion depth while positive shear stress leads to smaller corrosion depth than the zero-stress case. In addition, negative shear stress also changes the corrosion (or SCC) evolution direction. Negative shear stress applied on the top surface brings tension stress to the right side of the model. The tension stress leads to positive hydrostatic stress, contributing to faster corrosion growth. The sharp interface is formed with similar reasoning as with tensile stress case discussed above. The change of corrosion evolution direction is interesting. The shear stress acting on a stress element can result in a "shear diagonal", which is the principal tension in the diagonal direction as shown in Figure 2.9 (b). This principal tension creates higher hydrostatic stress in the perpendicular direction. With tensile stress on vertical direction, the principal stress direction is smaller than 45 degrees. Therefore, the corrosion evolves with the perpendicular direction to the principal stress direction.

However, the positive shear stress case shows completely different behavior. This is because positive shear stress at the top surface leads to compressive stress, and thus negative hydrostatic stress to the right side of the model. This results in a slower corrosion depth growth. Similar to the negative shear stress case, positive shear stress also results in shear diagonal at the

other diagonal direction. There is slightly more corrosion (upper left side) on the perpendicular direction to the shear diagonal. The difference is not as obvious as the negative shear stress case, as the compressive stress decreases the overall corrosion growth, and thus there is less stress concentration reducing the driving force from mechanical stress.

Figure 2.10 shows the effect of combined mechanical load of normal and shear stress. We can find that a tensile stress with a negative shear stress leads to the fastest corrosion depth growth, while a compression stress with a positive shear stress leads to the slowest corrosion depth growth. This is because the complex stress can result in higher or lower hydrostatic stress in the model.

The dynamic normal stress and shear stress described in Section 2.2 are applied on one side of the plate, resulting in the growth of pitting corrosion from the top center region. The dynamic stress is generated from the miter gate simulation described above. The results are shown in Figure 2.11. The corrosion evolution shows different growth speeds, directions, and shapes. This result is interesting as the dynamic load actually has a significant influence on the corrosion process.

It should be noted that pitting corrosion/propagation is a complex process that involves multiple chemical reactions, environmental impacts, and different kinds of nucleation mechanisms. This part mainly focuses on the influence from mechanical stress on the pitting corrosion. Therefore, the pitting shapes from this model cannot cover all the shapes reported from experimental observation [3]. However, some shapes are still foreseen from shapes in this model. As the Figure 2.12 shows, when the metal is under tensile loading, the pitting shape tends to be sharp and narrow; when under compression, the shape becomes wide and shallow; when without mechanical actions, the shape becomes semi-circle like, indicating isotropic corrosion; when under certain direction shear stress, sideway pit is more likely to be formed. In the future, the model can be extended with the environmental conditions associated with nucleation mechanisms as well as material microstructures.

2.3.8 Stress effect on the SCC initiation

Different normal stress and shear stress conditions are applied to the model to investigate the influence of stress level on the SCC initiation time. There is no SCC initiation when the compressive stress and positive shear stress are applied because they decrease the corrosion growth speed at the tip location where the stress concentration is critical; however, tensile stress and negative shear stress can lead to SCC initiation as Figure 2.9 shows. For both tensile stress and shear stress, the SCC initiation time decreases with the increase of stress level, which means higher stress level leads to an earlier SCC initiation. For the same magnitude of stress, shear stress results in earlier SCC initiation than tensile stress. The morphology on the right of Figure 2.13 also shows the SCC propagation direction of both the tension case and the shear case corresponding to the crack direction in the tension and shear failure modes.

2.4 Conclusions

The integration of mesoscale corrosion simulation, macroscale structural analysis, and statistical initiation time modeling provides a robust foundation for capturing pitting corrosion in large structures.

The influence of mechanical stress on the corrosion evolution and SCC initiation is analyzed in details. Tensile stress results in faster corrosion speed than compressive stress. Complex stress case can cause faster or slower corrosion speed than any simple stress of the same magnitude. Both tensile and shear stress can lead to sharp interface and potential crack initiation. Larger stress and higher reaction coefficient induce earlier crack initiation time. There are also some limitations in the current corrosion model. The impact of the environment is not studied in this work. The parameters related to the environment (such as reaction constant, diffusivity of metal ion) are considered as constant. The corrosion nucleation mechanism is not considered in this work. The corrosion is assumed to start at the beginning of the simulation. In addition, pitting corrosion/propagation is a complex process that involves multiple chemical reactions and

affected by different microstructures of the metal. The predicted pitting morphologies in this work cannot cover all the pitting formations reported in experimental observation [3]. These issues will be studied in our future work.

2.5 Appendices:

Normalization table

Parametere	Real value	Normalization	Normalized Value
Reaction constant L_η	$8.3\times10^{-6}/s$	$\tilde{L}_\eta = L_\eta \times \Delta t_0$	40
Gradient energy coeff. κ	$5\times10^{-5}J/m$	$\tilde{\kappa} = \kappa/(E_0 \times l_0^2)$	1×10^{-2}
Diffusion coeff. in electrode D^e	$7.19\times10^{-13}m^2/s$	$\tilde{D}^e = D^e/(l_0^2/\Delta t_0)$	2.157×10^{2}
Diffusion coeff. in solution D^s	$7.19\times10^{-10}m^2/s$	$\tilde{D}^s = D^s/(l_0^2/\Delta t_0)$	2.157×10^{5}
Time step Δt	$1.5\times10^{5}s$	$\Delta\tilde{t} = \Delta t/\Delta t_0$	5×10^{-3}

where the characteristic length $l_0 = 100\mu m$, the characteristic time $\Delta t_0 = 3\times10^9 s$, and the characteristic energy density $E_0 = 1.5\times10^6 J/m^3$.

Gaussian process regression

A Gaussian process is formed by assuming a zero-mean multivariant Gaussian prior distribution [120]

$$f(x_i) \sim \mathcal{N}(f|0,K), \tag{2.24}$$

where K is the covariance matrix, the element at i-th row jth column is $K_{ij} = k(x_i,x_j)$, k is a covariance function that describes the relation between different inputs, zero mean is assumed for the prior.

Assuming the noise to be Gaussian with a variance of σ_y^2, the joint distribution between training data and test data is given by

$$\begin{pmatrix} Y \\ y^* \end{pmatrix} \sim \mathcal{N}\left(\begin{pmatrix} Y \\ y^* \end{pmatrix} \middle| 0, \begin{bmatrix} K(X,X)+\sigma_y^2\mathbf{I} & K(X,x^*) \\ K(x^*,X) & K(x^*,x^*) \end{bmatrix} \right), \tag{2.25}$$

where x^* represents the new input vector for the test data and y^* represents corresponding predicted output, $K(X,X)$ is the covariance matrix between different training inputs with element $k(x_i,x_j)$, $K(x^*,X)$ denotes the covariance matrix between training inputs and new test inputs with element $K(x^*,x_j)$ and $K(x^*,x^*)$ denotes the covariance between new test inputs.

Next, the Bayesian inference is used to calculate the posterior distribution over y^*

$$y^* \sim \mathcal{N}(y^*|\mu^*(x^*), K^*(x^*,x^*)), \tag{2.26}$$

where the mean of posterior prediction is $\mu^*(x^*) = K(x^*,X)[K(x^*,x^*) + \sigma_y^2\mathbf{I}]^{-1}K(X,x^*)$, and the variance of posterior prediction is $K^*(x^*,x^*) = K(x^*,x^*) - K(x^*,X)[K(x^*,x^*) + \sigma_y^2\mathbf{I}]^{-1}K(X,x^*)$

2.6 Remarks

Material for this chapter was published in the following articles:

[1] **Guofeng Qian**, Karnpiwat Tantratian, Lei Chen, Zhen Hu, and Michael D Todd. A probabilistic computational framework for the prediction of corrosion-induced cracking in large structures. *Scientific Reports*, 12(1):20898, 2022.

[2] **Guofeng Qian**, Zhen Hu, and Michael D Todd. A hybrid surrogate modeling method for corrosion morphology prediction under non-stationary dynamic loading. In Structural Health Monitoring 2023, *Proceedings of the International Workshop on Structural Health Monitoring 2023*, pages 643–650. DEStech, 2023.

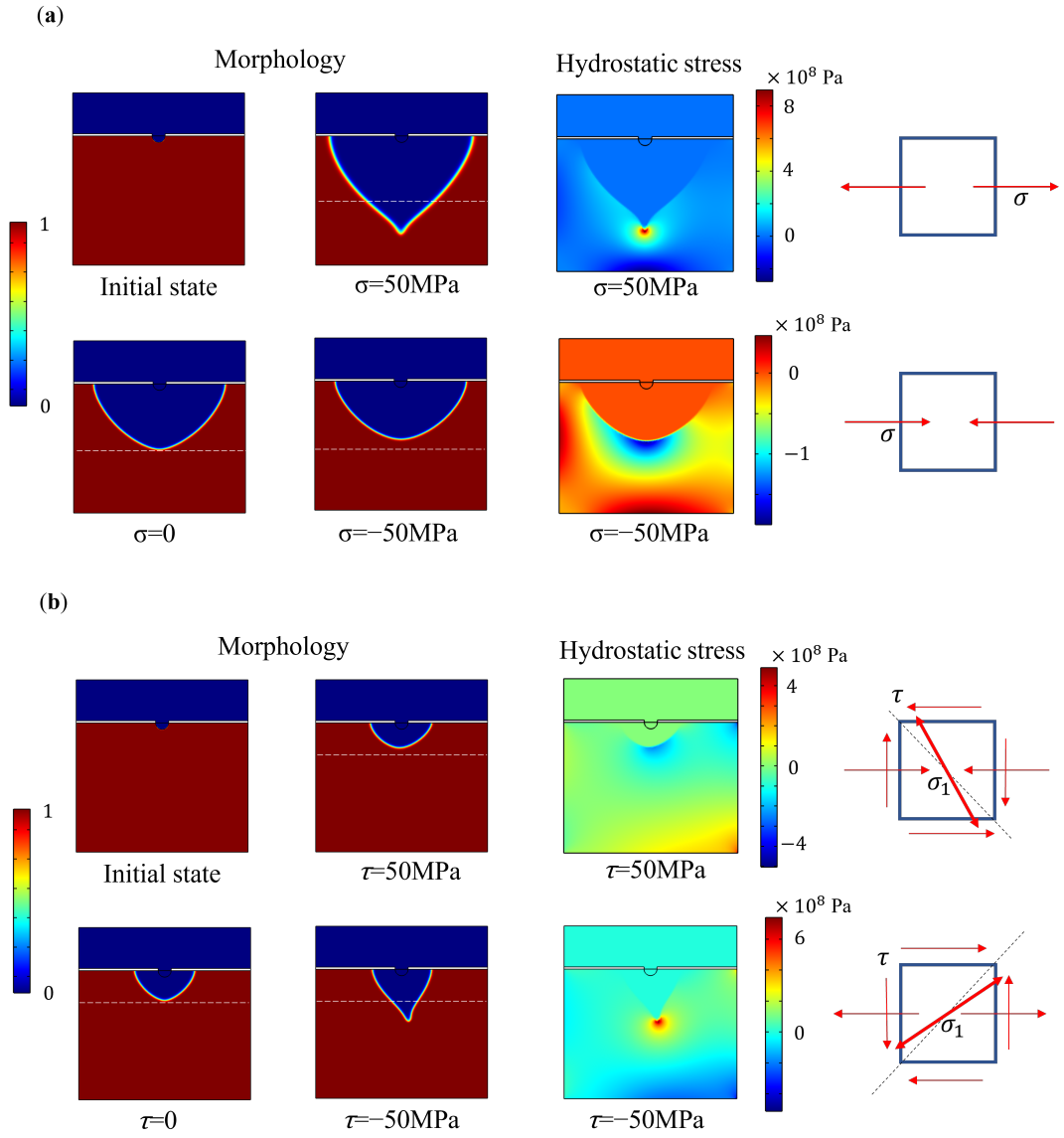

Figure 2.9. Results of pitting corrosion evolution with the influence of (a) normal stress, and (b) shear stress

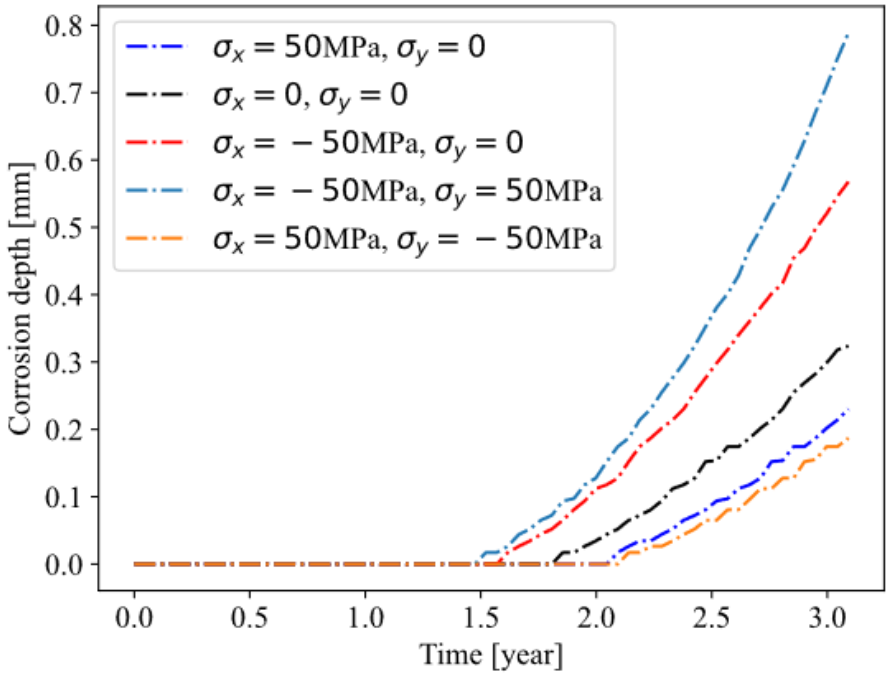

Figure 2.10. Corrosion depth under different stress conditions

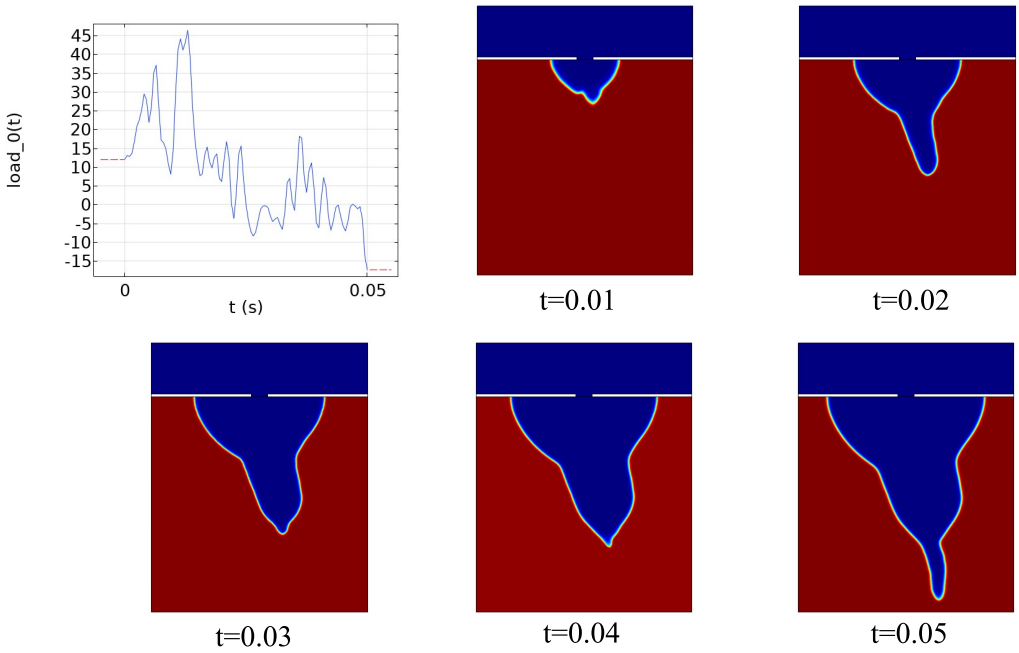

Figure 2.11. Corrosion simulation result and mechanical dynamic load

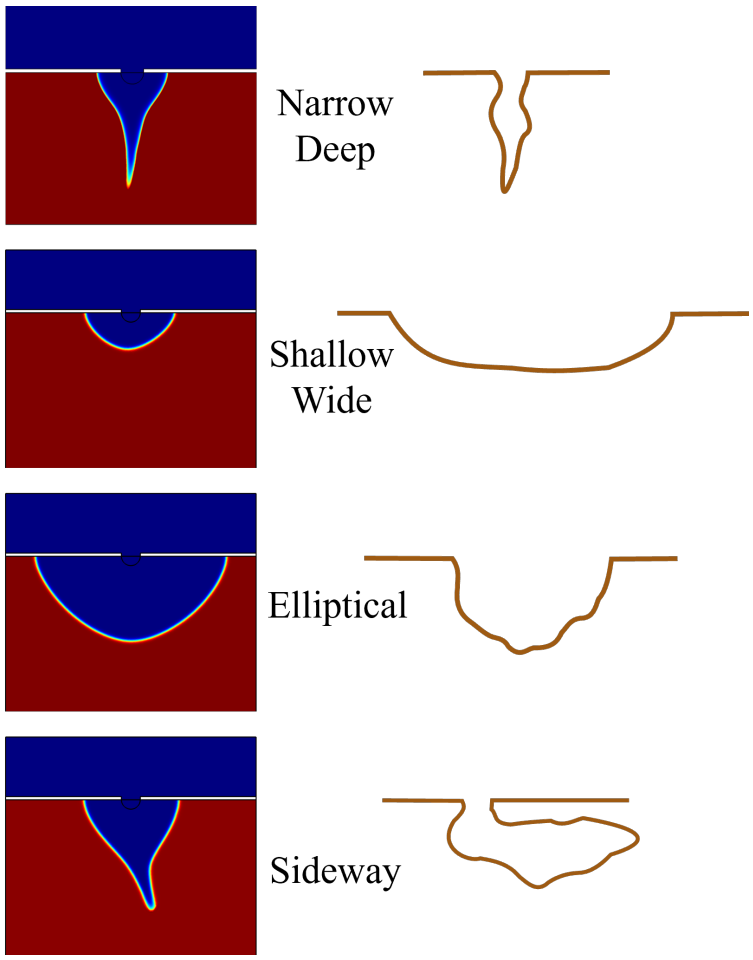

Figure 2.12. Different pitting shapes from simulations (left) and observations (right)

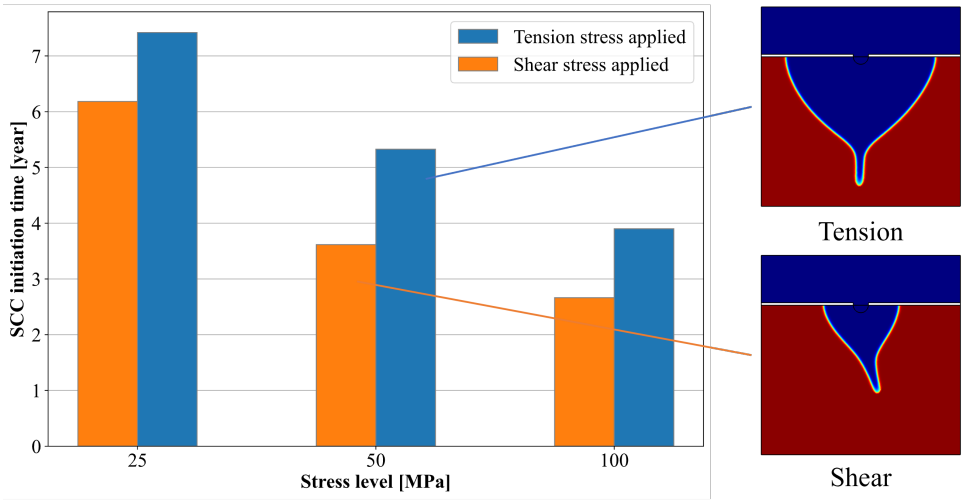

Figure 2.13. Stress influence on SCC initiation

Chapter 3

Machine Learning-Based Surrogate Modeling

3.1 Introduction

Pitting corrosion under stress is a common type of degradation in civil infrastructure [96, 64]. Forecasting the damage evolution of pitting corrosion over time is essential for maintenance planning and life-cycle cost optimization for any structure where corrosion-induced consequences are important. Specifically, one limit state is defined as the corrosion-induced cracking initiation within the time of interest. The curvature information from corrosion morphology, together with stress condition, is utilized in the crack initiation criterion based on fracture mechanics. The detailed information can be found in Ref. [118]. Damage limit state forecasting may be typically performed using some form of a data-driven method, a physics-based approach, or a combination thereof [144, 145]. For large civil infrastructures such as the miter gates considered in this work, data that indicate degradation caused by pitting corrosion are usually unavailable. Physics-based corrosion damage prediction using high-fidelity computer simulations provides a promising way to overcome this challenge.

The operational and environmental loading (demand) play a significant role in corrosion evolution over long-term life cycle operations [121]. In order to account for these factors in physics-based simulation of pitting corrosion growth, different kinds of computational models have been proposed such as the finite volume method (FVM) [128], cellular automata (CA)

techniques [137], peridynamic (PD) formulations [161], and phase-field (PF) models [30]. Among them, the phase-field method has the advantage of having the flexibility to couple the mechanical stress into the electrochemical equations to simulate the corrosion growth under mechanical stress [118].

When physics-based models such as the phase-field model are employed for failure forecasting, various sources of uncertainty (e.g., material properties, load conditions, etc.) in the simulation model need to be considered [70]. Proper consideration usually requires many (thousands or more) evaluations of the high-fidelity simulation model, particularly if a Monte Carlo simulation (MCS)-based method is adopted. However, the phase-field simulation is computationally very expensive due to multiple coupled nonlinear partial differential equations (PDE). Advanced uncertainty quantification or reliability analysis methods are therefore usually needed to tackle the computational challenge. Among existing uncertainty quantification or reliability analysis methods, MCS based on surrogate modeling is one of the most widely used. In such a strategy, a computationally cheaper yet accurate surrogate model is first constructed to replace the computationally expensive computer simulation models. MCS is then conducted using the surrogate model to quantify the distribution of features of interest (e.g., corrosion depth, shape) or predict the probability of failure (limit state analysis) [69].

Multiple approaches have been made in recent years to build surrogate models emulating phase-field simulations. For instance, Shen et al. [131] used the least square regression (LSR) and the back-propagation neural network (BPNN) to produce an analytical expression for the breakdown strength based on phase-field simulation data. Eduardo et al. [37] utilized k-nearest neighbor (k-NN) and artificial neural networks (ANN) algorithms to detect the presence and location of failure based on simulation data. For time-dependent processes, Montes et al. [103] applied a long-short-term (LSTM) network to perform microstructure evolution predictions as the surrogate model of the phase-field simulation. The principal component analysis (PCA) technique was applied for dimension reduction; however, the reconstructed microstructure from the LSTM-trained surrogate model had a considerably noisy boundary. Nevertheless, in the

corrosion simulation, the boundary between the corroded material and the solution is of main interest.

This work overcomes the limitations of current pitting corrosion simulation methods by proposing a surrogate model combining Convolutional neural network (CNN) and Gaussian process (GP)-based nonlinear autoregressive network with exogenous inputs (NARX) to predict the corrosion growth and potential crack initiation time and location. This model can provide accurate prediction with negligible computing time, enabling probabilistic methods for risk-informed lifecycle management. The other physics-constrained surrogate model is furtherly proposed to reduce the prediction epistemic uncertainties of the previous CNN-GP-NARX model. This model consists of a convolutional variational autoencoder to reduce the dimension of pitting corrosion shape images and a Bayesian multi-layer perceptron network (also known as the Bayesian Latent Space Time Evolution Network) to model the evolution of the corrosion pit morphology over time. To account for the fact that corrosion damage without repair is an irreversible process, a physics constraint is added to the surrogate model to ensure that the corrosion rate is strictly negative.

3.2 CNN-GP-NARX surrogate model of pitting corrosion simulation and crack initiation

The inputs for the proposed surrogate model are the corrosion morphology at a certain time step t, the external mechanical load, and other physical parameters including reaction constant and diffusion coefficient that would affect the growth of the corrosion pits over time. The output of the surrogate model is the corrosion morphology at future time step $t+n(n>0)$. Specifically, the corrosion morphology here are represented by the order parameter ξ value in the phase-field model defined in Section 2.3, ranging from 0 to 1 where 0 means liquid while 1 means metal. 80 by 40 pixels for one channel (ξ) are extracted from the FEM implementation results to represent the corrosion morphology in our study.

To extract features, a CNN-Autoencoder and decoder is used to map the high-dimensional corrosion morphology into low-dimensional compressed features in the latent space. Low-dimensional features need to be extracted from the images to feed into the GP-NARX algorithms, as fewer features require fewer training data and less training time. The model also can make more accurate predictions with fewer features if features encode the essential information needed for prediction. Figure 3.1 presents the overall workflow of the CNN-GP-NARX surrogate modeling method.

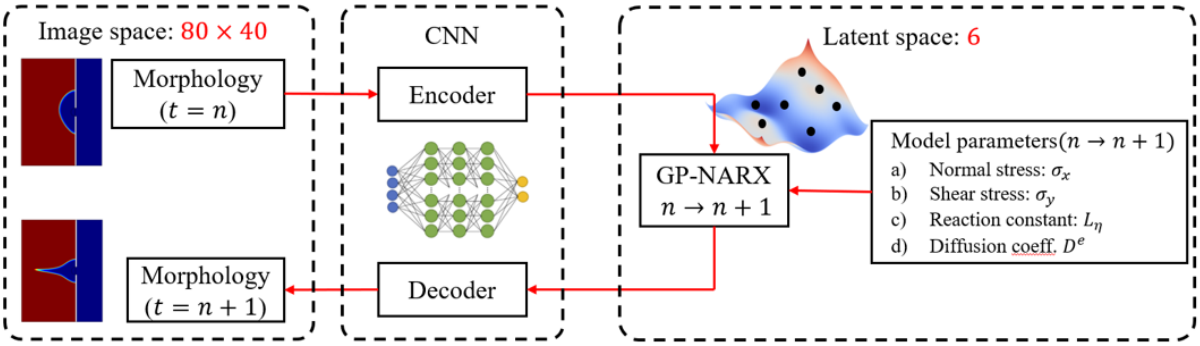

Figure 3.1. Workflow of CNN-GP-NARX Surrogate model

3.2.1 CNN-autoencoder and decoder for dimension reduction

A CNN is selected as the autoencoder in our surrogate model for feature extraction because a CNN is the most widely used architecture for image data. Several filters in the convolutional layers would extract important features when images pass through. We compared CNN with commonly used dimension-reduction techniques, such as principal component analysis (PCA). The results show that CNN has a better performance. PCA requires hundreds of principal components to obtain 98% variance for 80-by-40 pixel images, while CNN can reduce the dimension to fewer than ten with accurate reconstruction.

Different numbers of features have been tested for the CNN architecture and the test loss history is shown in the Figure 3.2. The decrease of the test loss with the increase of the number of features stops when the feature number gets to six. This number might be sensitive to the size and

architecture of the neural network. In this work, the number of latent features is therefore chosen as six for the CNN. As shown in Figure 3.3, the CNN-autoencoder contains six layers, including two combinations of one convolutional layer followed by one max-pooling layer to reduce the dimension, a dense layer to flatten multi-dimensions output from previous convolutional layers to one-dimensional vector, and a fully connected layer to reduce the length of the one-dimensional vector from the dense layer to the ideal number of features. In this network, six features are kept after compression with encoder to balance the error and dimension reduction performance according to the test results shown in Figure 3.1. The decoder consists of two fully connected

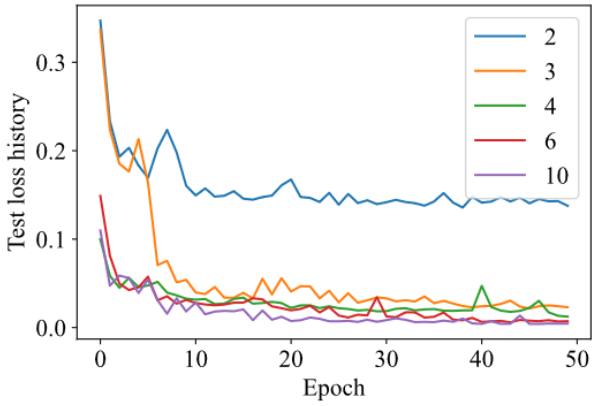

Figure 3.2. Test loss history of different numbers of features

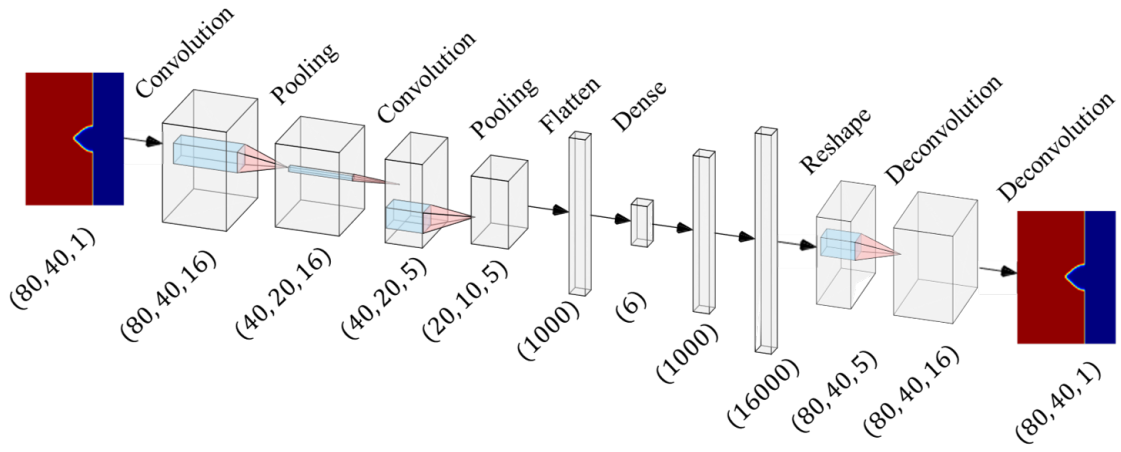

Figure 3.3. Architecture of CNN-autoencoder

layers followed by two deconvolutional layers to reconstruct the image from the compressed

features. There are no un-pooling layers because that requires extra information, namely the indices of maximum values from the max-pooling layer. However, the decoder should work independently without any extra information from the encoder after training. In other words, the information needed in the images is not properly compressed into features since there are still some information that lies in the indices of maximum values.

The encoder and decoder are trained together. The purpose of encoder-decoder structure is dimensionality reduction. Therefore, more accurate reconstruction results are desired from low-dimensional latent space. Thus, the input and output for training is the same image. In this case, 75% of the morphology images are randomly selected for training, and the remaining 25% is used to validate the neural network.

3.2.2 GP-NARX models

Gaussian process regression (GPR) is a probabilistic predictive model class that has been widely used in many domains to build a data-driven model for prediction [120]. It has an advantage over other machine learning models in that it provides not only mean predictions (a "point estimate", like a neural network) but also confidences in a closed form. While GPRs are widely employed for surrogate modeling of static and quasi-static problems, they may be extended for dynamic systems by adopting a nonlinear autogressive exogenous model (NARX) framework. NARX model describes the relationship between the responses y_i at t_i as a nonlinear function of exogenous inputs as follows

$$y_i = G\left(y_{i-1}, \cdots, y_{i-p}, u_i, \cdots, u_{i-q}\right) = \varepsilon_i, \tag{3.1}$$

where $G(\cdot)$ is a nonlinear function, $u_i, \cdots, u_{i-q}$ are the exogenous inputs, p and q are respectively the number of lags for the inputs and the response variable, and ε_i is the error term.

In GP-NARX, a GPR model is constructed to learn the nonlinear function $G(\cdot)$. Let the latent responses of corrosion morphology after the mapping using CNN-autoencoder be

$\boldsymbol{\alpha}_1, \cdots, \boldsymbol{\alpha}_6$, where $\boldsymbol{\alpha}_j = \left[\alpha_{j1}, \alpha_{j2}, \cdots, \alpha_{jN_t}\right], \forall j = 1, \cdots, 6$ is a vector of the j-th latent response, α_{jk} is the j-th latent response at time step t_k, and N_t is the total number of time steps in the pitting corrosion simulation, six GP-NARX models are constructed in the latent space as follows

$$\alpha_{jk} = \hat{G}_j\left(\tilde{\boldsymbol{\alpha}}_1, \cdots, \tilde{\boldsymbol{\alpha}}_6, \boldsymbol{\theta}\right) + \varepsilon_k, \forall j = 1, \cdots, 6, \tag{3.2}$$

in which $\tilde{\boldsymbol{\alpha}}_j = \left[\alpha_{j1}, \cdots, \alpha_{jp}\right]$ are the previous p time steps of the j-th latent response, $\alpha_{jk} \sim N(\mu_{jk}, \sigma_{jk}^2)$ is a probabilistic prediction which is represented as a Gaussian distribution with mean μ_{jk} and standard deviation σ_{jk} from the GP-NARX models, and $\boldsymbol{\theta}$ is a vector of other input parameters that affect corrosion growth at previous time steps. Note that parameters $\boldsymbol{\theta}$ change slowly in the corrosion problem and thus are assumed to be constant in the simulated time period.

Once the GP-NARX models are trained, there are two kinds of prediction that may be performed. The basic one is one-step ahead prediction. One-step ahead prediction is made with the observations from previous certain steps, which is using morphology features of a few continuous time steps to predict latent features of the following step, i.e.,

$$\alpha_{jk}^* = \hat{G}_j\left(\tilde{\boldsymbol{\alpha}}_1, \cdots, \tilde{\boldsymbol{\alpha}}_6, \boldsymbol{\theta}\right) + \varepsilon_k, \forall j = 1, \cdots, 6; \text{where } \alpha_{jk}^* \sim N(\mu_{jk}^*, \sigma_{jk}^{*2}), \tag{3.3}$$

The other kind of prediction is called multi-step ahead prediction. In multi-step ahead prediction, the prediction at the current time step will be used as inputs of the future time steps and is performed recursively as follows

$$\alpha_{jk}^* = \hat{G}_j\left(\tilde{\boldsymbol{\alpha}}_1^*, \cdots, \tilde{\boldsymbol{\alpha}}_6^*, \boldsymbol{\theta}\right) + \varepsilon_k, \forall j = 1, \cdots, 6, \tag{3.4}$$

where $\tilde{\boldsymbol{\alpha}}_j^* = \left[\alpha_{j1}^*, \cdots, \alpha_{jp}^*\right]$ is a vector of uncertain predictions from previous time steps. Usually, multi-step ahead prediction is more demanding for the model, as the errors from every previous prediction can accumulate.

Since a large volume of data may be generated from each simulation in the pitting corrosion simulation process, each simulation data step is down-sampled by every third time step, as the original time interval is too small to show obvious corrosion evolution. After the data down-sampling, p=5 is chosen in this work, which is a number determined through cross-validation that can give the best prediction. It means that the compressed morphology features of previous 5-time steps (15-time steps from the simulation) are used in the input of NARX structure. The considered model parameters $\boldsymbol{\theta}$ as mentioned above include external normal load, external shear load, reaction constant, and the diffusion coefficient.

3.3 Physics-Constrained machine learning-based surrogate model of pitting corrosion simulation

A physics-constrained ensemble of neural networks is proposed in this section as a surrogate model to predict the pitting corrosion evolution over time. As shown in Fig. 3.4, the ensemble had two main components: a convolutional variational autoencoder (CVAE) that reduced the dimensionality of the pitting corrosion images, and a multilayer perceptron network (i.e., BLSTEN) that modeled the time evolution of the corrosion. The machine learning components were implemented using Tensorflow 2.10.0 and Tensorflow Probability 0.18.0. Multiple loss terms including a reconstruction loss, a latent space disentanglement loss, a BLSTEN loss, and physics loss are combined together to co-train the CVAE and BLSTEN networks, in order to ensure the effectiveness of the training and to incorporate physical laws into the training of the neural networks. The following subsections explain the models and different loss terms in detail.

3.3.1 Convolutional Variational Autoencoder

The first network is a CVAE designed to reduce the dimensionality of the corrosion images, represented by ξ. The encoder $q_{\Phi}(\mathbf{z}|\xi)$ consists of three 2D convolutional layers with a kernel size of 3, stride of 2, and 9 filters. The swish activation function is used for all the layers.

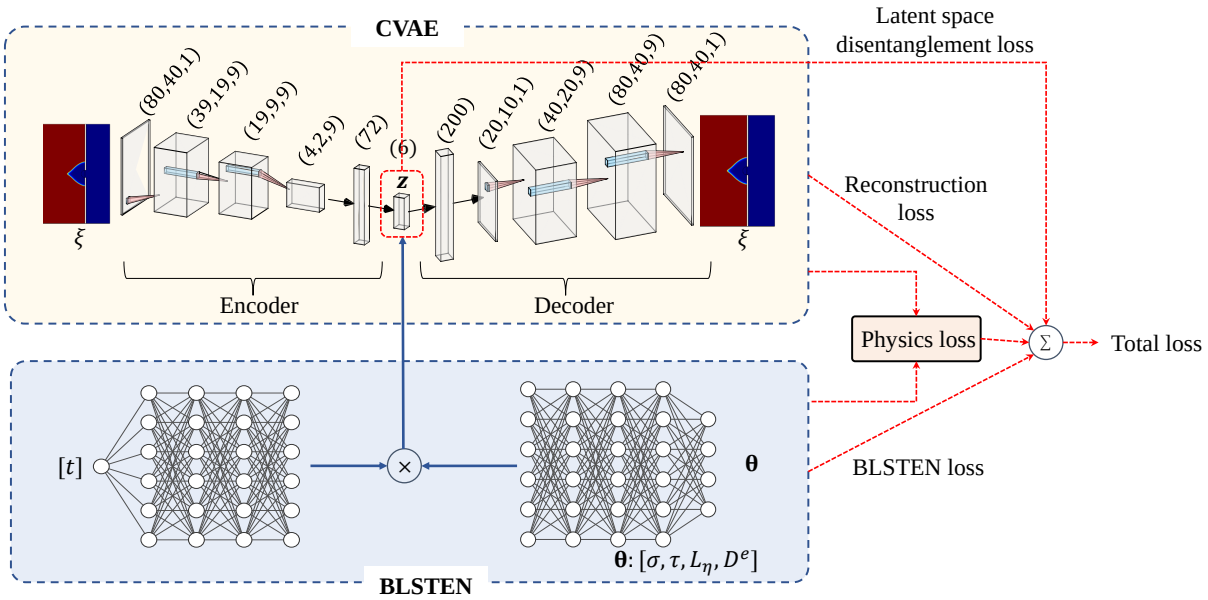

Figure 3.4. Schematic of the proposed general neural network architecture.

The output from the 2D convolutional layers is then flattened and passed to a dense variational layer with a trainable posterior mean field. The output of the encoder is a random latent vector $\mathbf{z}$

$$\mathbf{z} \sim q_{\Phi}(\mathbf{z}|\xi), \tag{3.5}$$

where Φ represents the encoder weights.

The second component of the autoencoder architecture is the decoder $p_{\Psi}(\xi|\mathbf{z})$ which takes the latent vector and maps it back to the full original dimension. The decoder consists of three 2D convolutional layers with a kernel size of 3, stride of 2, and 9 filters, except for the last one which had a single filter to match the original corrosion image. The output of the decoder is a matrix corresponding to a reconstruction of the original image

$$\hat{\xi} \sim p_{\Psi}(\xi|\mathbf{z}), \tag{3.6}$$

where Ψ represents the decoder weights.

Following this formulation, the loss function for the CVAE model corresponds to the

negative evidence lower bound (ELBO), given by

$$\mathscr{L}_i^{VAE} = -\mathbf{E}_{\mathbf{z}\sim q_\Phi(\mathbf{z}|\xi_i)}[\log p_\Psi(\xi_i|\mathbf{z})] + \beta \mathbf{KL}(q_\Phi(\mathbf{z}|\xi_i) \,||\, p(\mathbf{z})), \tag{3.7}$$

where the subscript i represents the loss associated with the i-th training sample, $\mathbf{KL}(\cdot)$ is the Kullback–Leibler (KL) divergence, $p(\mathbf{z})$ is assumed to be a spherical multivariate standard distribution, and β is a parameter used to weigh the contribution of the KL divergence term. The first term in Eq. (3.7) represents the reconstruction loss and the second term controls the level of latent space disentanglement, as described in [23]. As shown in Fig. 3.4, this loss term will be combined with other loss terms to co-train the CVAE along with the BLSTEN model (see the detailed description in the subsequent section).

3.3.2 Bayesian Latent Space Time Evolution Network

A separate Bayesian multilayer perceptron network (known as the Bayesian Latent Space Time Evolution Network or BLSTEN) is used to model the time evolution of the pitting corrosion phenomenon in the latent space. The CVAE and the BLSTEN are both trained concurrently. The BLSTEN architecture is based on DeepONet [97] and is shown in Fig. 3.4. DeepONet leverages the concept of neural networks as universal operator approximators (based on the universal nonlinear operator approximation theorem introduced by Chen and Chen [31]). As depicted in Fig. 3.4, the DeepONet consists of

- a branch network (i.e., $g_\lambda^B(\mathbf{\Theta})$) that encodes the discrete input function space and,
- a trunk network (i.e., $g_\nu^T(t)$) that encodes the domain of the output functions.

where the mechanical load and the environmental factors $\mathbf{\Theta} = [\sigma, \tau, L_\eta, D^e]$ are the normal stress, shear stress, reaction constant, and diffusion coefficient. This architecture is desirable here because the objective is to construct the neural network as an operator that models the latent space vector over a function space representing different scenarios (e.g., loading cases) to

evaluate the corrosion evolution over time. The trunk is a deterministic neural network while the branch is a fully Bayesian neural network. The rationale behind this architectural choice was that it is expected that the majority of the network epistemic uncertainty will be associated with the model-form error coming from the parametric portion of the model because it is known that the network's functional form will only be an approximation of the true underlying solution. Both the trunk and branch are multilayer perceptrons (MLP) with 3 fully connected layers, with 6 units each, and a swish activation function. Unlike a traditional neural network which learns to predict point estimates, a Bayesian Neural Network learns the posterior distribution, $P(w|\mathscr{D})$, over the weights given an assumed prior distribution, $P(w)$ following Bayes theorem as

$$P(w|\mathscr{D}) = \frac{P(\mathscr{D}|w)P(w)}{\int P(\mathscr{D}|w')P(w')\mathrm{d}w'}, \tag{3.8}$$

where w are the model weights to be estimated, $\mathscr{D}$ represents the training data, and $P(\mathscr{D}|w)$ is the likelihood of observing $\mathscr{D}$ for given weights w.

As described in [18], obtaining the exact predictive posterior distribution is intractable for neural networks of any practical size due to the challenge of computing the term in the denominator of Bayes theorem. A common approach for approximating the predictive posterior is to rely on variational inference, as described in Refs. [67, 57]. In this formulation, we begin by minimizing the KL divergence between a variational posterior distribution $q(w\|\mu)$ and the desired posterior distribution $P(w|\mathscr{D})$. The KL divergence term is defined as

$$\mathbf{KL}(q(w|\mu)||P(w|\mathscr{D})) = \int q(w|\mu)\log\left(\frac{q(w|\mu)}{P(w|\mathscr{D})}\right)\mathrm{d}w, \tag{3.9}$$

where μ are the parameters of the variational distribution $q(w|\mu)$.

This formulation leads to the familiar problem of minimizing the variational free energy or maximizing the expected lower bound (ELBO) which consists of two terms: a KL distance between the variational distribution and the weights prior distribution (effectively acting as a

complexity cost) and the negative log-likelihood term that effectively captures the reconstruction loss term. The total loss term is defined as

$$\mathscr{H}(\mathscr{D},\mu) = \mathbf{KL}[q(w|\mu)\|P(w)] - \mathbf{E}_{q(w\|\mu)}[\log P(\mathscr{D}|w)]. \tag{3.10}$$

This formulation is used to train the network by employing the Bayes by the Backprop algorithm, as described in [18]. In practice, the loss function is approximated by employing Monte Carlo sampling such that the loss over a batch of size n is computed as

$$\mathscr{H}(\mathscr{D},\mu) \approx \sum_{i}^{n} \log q(w^{(i)}|\mu) - \log P(w^{(i)}) - \log P(\mathscr{D}|(w^{(i)}), \tag{3.11}$$

where $w^{(i)}$ represents the i-th Monte Carlo sample drawn from the variational posterior $q(w|\mu)$. In this way, the network can be trained more or less as a traditional neural network using the tools available in Tensorflow and Tensorflow Probability [39]. Specifically, a dense variational layer with a Gaussian mean posterior field is used in Tensorflow to keep track of the variational posterior distribution. Thus, the loss term $\mathscr{H}$ is internally added by Tensorflow during training.

The inputs to the network are the set of parameters $\boldsymbol{\Theta}$, which contains the applied normal (σ) and shear (τ) stress, the reaction constant (L_η), and the diffusion coefficient (D^e). In addition to the parameter vector $\boldsymbol{\Theta}$, the time vector is also included as part of the input. A new latent vector sample is obtained from the BLSTEN as

$$\tilde{\mathbf{z}} \sim g_\Pi(\tilde{\mathbf{z}}|\boldsymbol{\Theta},t) = g_\lambda^B(\boldsymbol{\Theta}) g_\nu^T(t), \tag{3.12}$$

where $g_\lambda^B(\boldsymbol{\Theta})$ and $g_\nu^T(t)$ are the branch and trunk networks, respectively, and $\Pi : [\lambda, \nu]$ are the network weights.

The fact that pitting corrosion is an irreversible process was implemented into the

architecture by constraining the corrosion rate to be negative via a physics loss term

$$\mathscr{L}_i^{PHYS} = \left[\mathbf{ReLU}\left(\frac{d\xi}{dt}\right)_i\right]^2, \tag{3.13}$$

where **ReLU** is the rectified linear unit function which is non-zero only for positive values. The corrosion rate can be obtained via autodifferentiation from the decoder and the BLSTEN as

$$\frac{d\xi}{dt} = \frac{\partial \xi}{\partial \tilde{\mathbf{z}}}\frac{\partial \tilde{\mathbf{z}}}{\partial t} = \frac{\partial p_\Psi(\xi|\tilde{\mathbf{z}})}{\partial g_\Pi(\tilde{\mathbf{z}}|\boldsymbol{\Theta},t)}\frac{\partial g_\Pi(\tilde{\mathbf{z}}|\boldsymbol{\Theta},t)}{\partial t}. \tag{3.14}$$

Lastly, the output from the encoder and the BLSTEN have to be reconciled. This result is achieved by minimizing the negative log-likelihood as

$$\mathscr{L}_i^{BLSTEN} = -\mathbf{E}_{\mathbf{z}\sim q_\Phi(\mathbf{z}|\xi_i)}[\log g_\Pi(\mathbf{z}|\boldsymbol{\Theta},t)]. \tag{3.15}$$

The total loss that combines the above loss terms as illustrated in Fig. 3.4 is computed over the N training samples as

$$\mathscr{L} = \frac{1}{N}\sum_i^N(\alpha\mathscr{L}_i^{VAE} + \gamma\mathscr{L}_i^{BLSTEN} + \phi\mathscr{L}_i^{PHYS}), \tag{3.16}$$

where $\alpha = 500$, $\gamma = 1$, and $\phi = 1$ are the weights used to scale the different loss terms to have roughly the same order of magnitude. The values were determined based on trial and error until it was observed that all the terms were converging to similar orders of magnitude. A more systematic strategy could be used in the future to address this challenge such as gradient surgery for multi-task learning [158] or competitive loss functions [160].

The networks are trained using the Adam optimizer with a learning rate set to 10^{-4}. Next, we use a numerical example to demonstrate the efficacy of the proposed physics-constrained surrogate model.

3.4 CNN-GP-NARX surrogate model results

3.4.1 Data preparation

Due to the lack of availability of measurement data and the challenges associated with creating long-term corrosion experiments (which is beyond the scope of this initial study), all data used for training and validating the framework is generated by the proposed calibrated high-fidelity phase-field model. The dataset used to train a surrogate model needs to seek as much information as possible with a moderate computational cost.

Four parameters—external normal stress, external shear stress, reaction constant, and diffusion coefficient—are chosen as the input parameters to the surrogate model. External load is the mechanical load applied to the top and bottom surface of the plate structure, which is tensile stress or compressive stress in the model. The reaction constant describes the rate of electrochemical reaction in the system. The diffusion coefficient represents the ratio of flux density to the negative of the concentration gradient in direction of diffusion. These four parameters are considered as major driving factors for the corrosion process. The ranges of chosen parameters are determined based on the calibration results given in Section 2.3.6 Then, a Sobol sampling technique is used to obtain a low discrepancy quasi-random sequence of the model parameters, which are inputs of the training data. For each training data set of inputs (external load, reaction constant, and diffusion coefficient), 200-time steps of the high-fidelity phase-field simulation are executed, and 200 corrosion morphology images are obtained. In total, 51,000 corrosion morphology images are generated from the 255 simulations.

The whole model is overall complex and deep learned, such that more simulations for the train and validation is desirable. Given that each simulation costs more than 40 minutes on our workstation, 255 simulations are completed in total. 10 random selected simulations are used as the final test set for the whole surrogate model, combining CNN-autoencoder and GP-NARX to check the multi-step prediction ability in the image space. This set has never been presented to the neural network before testing. They are in neither the encoder-decoder training process, nor

the GP-NARX training process.

The CNN-autoencoder part is trained with randomly selected 90% of total 245×200 images and validated with the rest 10%. The data dimension after compression is 6×245×200. As explained in Section 3.2, the features are down-sampled by every third time step, leading to a 6×245×66 dimension. The GP-NARX model predicts the features of the next time step based on the 5 previous time steps. Therefore, the data are sliced into multiple 6-time-steps pieces where the first five serve as a part of the input of the GP-NARX model and the last serves as the output. 90% of slices are randomly selected as the training set and the rest are for the validation. There is still little overlap for the training and validation sets in the encoder-decoder part and GP-NARX part because the GP-NARX models are dynamic models while the CNN-based encoder-decoder model is static.

3.4.2 Low dimension features representation of phase-field results

A CNN-autoencoder is trained together with the decoder. Images with 80 by 40 pixels are compressed with the autoencoder to only six features in the latent space. Then the six features are used to reconstruct the original images. The dimensionality reduction rate which is calculated as the dimension after compression divided by the dimension before compression, is about 0.19%. The encoder decoder model is later tested on a validation set which is not seen by the model. Figure 3.5 shows the results comparison between the original images and the reconstructed images.

Although the dimension is reduced significantly with a dimensionality reduction rate less than 1%, the overall error due to dimension reduction is negligible. The first row shows the original corrosion morphology from different time step results of dynamic phase-field model. The second row show the images reconstructed with the six features after encoder. The third row shows the error between the original images and the reconstructed images as well as the error percentages. We can notice that the overall error value is close to zero in the area. The most error concentrates on the interface area, as regions away from the interface are constant

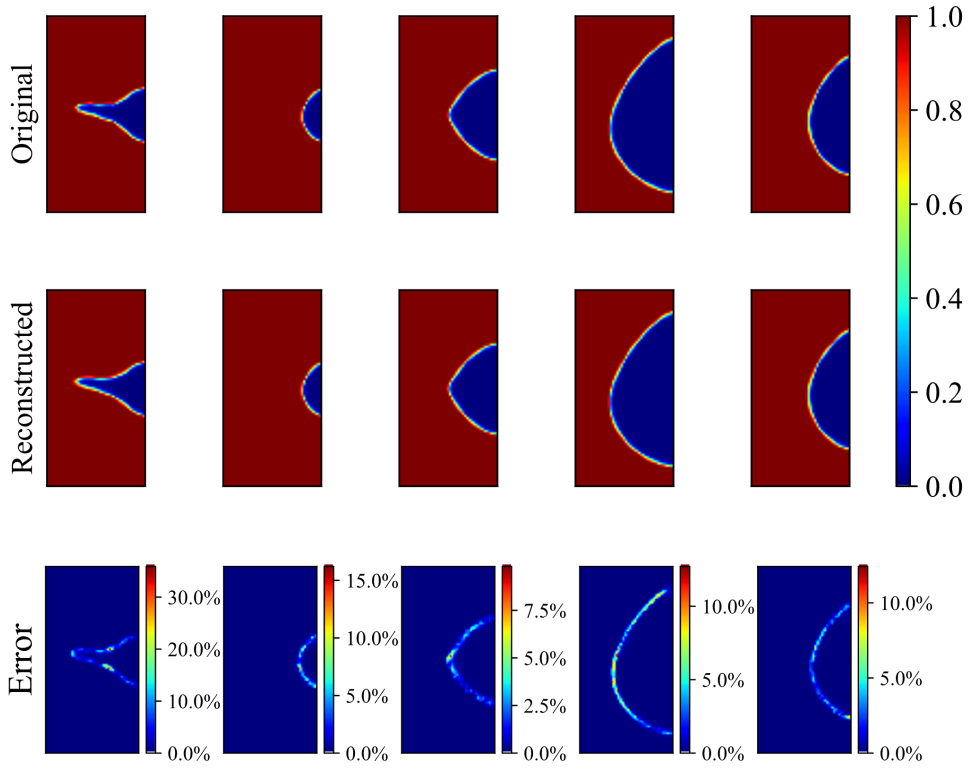

Figure 3.5. Comparison and error of reconstructed figure from latent space

(either zero or one) while the order parameter changes between zero and one in the interface. The encoder-decoder model can accurately capture the constant regions and has good ability to compress the changing regions. Notice that the highest-error region is only a very small fraction of the whole surface.

A sharper interface would lead to larger error in the interface. For a flat morphology, the maximum error at the interface is within ten percent. For sharper interface, the maximum error at the interface is about 30%. One possible reason for this is that there are more flat morphology images than sharp morphology images. The dynamic corrosion results are extracted from the phase-field simulation at each time step and each time step has the same length. During the corrosion evolution process, the sharp interface lasts for very short time while flat interface lasts for a long time. This is also related to the crack initiation that will be discussed later. Therefore, there would be far more images with a flat interface than that with sharp interface. Given more

training data for flat interfaces, less error for flat interface can be explained. The other reason is that a sharp morphology is more complex than that of flat interface. As a result, there is more error for more complex image, if both are compressed to the same number of features.

3.4.3 GP-NARX prediction results

Like CNN-autoencoder, ten percent and ninety percent data from the 245 simulations are served as training and validation datasets. The GP is trained with down-sampled data. Each input contains features from the previous five time steps with six dimensions in the latent space for each time step and the four parameters. Therefore, the dimension of the inputs for each GP-NARX model is 34 in total. Each output contains the features for the next step, which is six dimensions. Additional ten simulations data is used as the testing dataset.

Figure 3.6 shows the result of one-step ahead prediction of the trained GP-NARX models. Random samples from validation set are predicted and the prediction results are plotted with true values. We can see that the prediction is very accurate for features 1 to 5. The predicted value and the true value are very close, and the points are distributed more uniformly. Most samples of feature 6 concentrate on small values near zero. Most values are within 0 and 0.03. Such small change might indicate that the feature 6 is not making a significant difference most of the time but there are some large values exists as well. Some predictions are slightly off the diagonal line, but overall, the prediction is still accurate. To further evaluate the performance of the model, the more challenging multi-step ahead prediction is also implemented. True feature values of the first five steps in the down sampled data and four parameters are used as the initial input and then the predicted data is used as the part of input to predict the features of the following time step. This equates to predicting sixty steps with the first five steps in the down-sampled data. To account for the epistemic uncertainties in the GP model, the predicted mean (i.e., μ_{jk} in Equation 3.3) is not directly used as part of the input for the next step. Instead, samples of a Gaussian distribution with predicted mean and variance are used as the part of the input for the next step. 1000 realizations are predicted with the same initial input for each simulation in the

testing dataset.

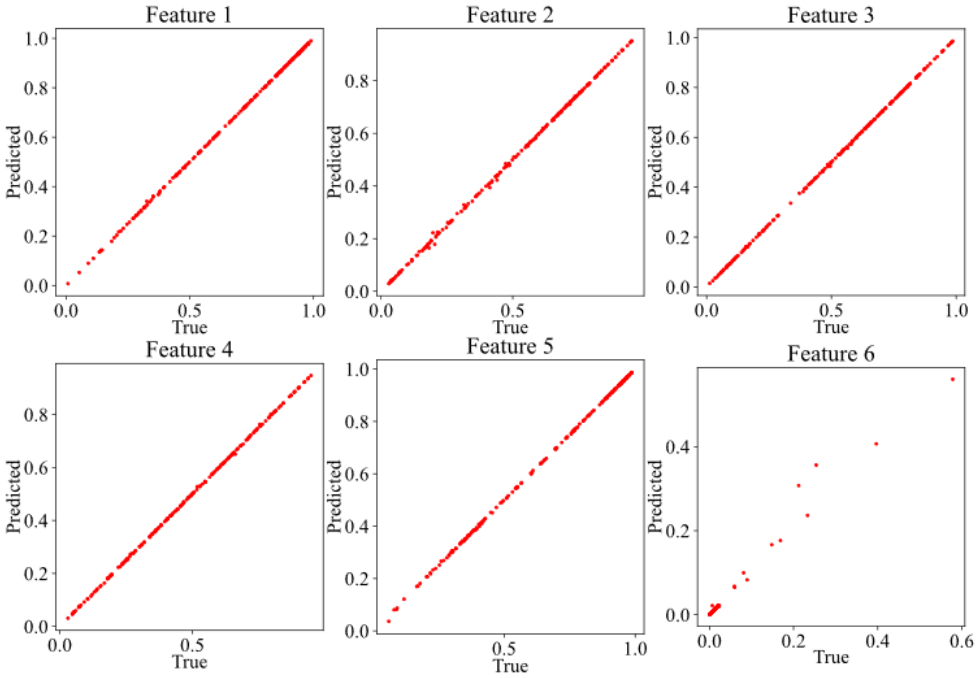

Figure 3.6. One-step-ahead prediction result in the latent space

Two different cases are chosen to plot as the representative of the testing dataset. The input parameters for case (a) and case (b) of the phase-field model are 19.14 and -30.86 MPa for the shear stress, 9.18 and 34.18 MPa for normal stress, 7.13 and 2.23 for reaction constant, and 2.06 and 4.46 for diffusion coefficient, respectively. Figure 3.7 (a) and (b) show the results of multi-step prediction of six features after compression in case (a) and case (b). We can see that the prediction is accurate for all six features for case (a). The narrow confidence interval shows that the model is confident about the prediction. Although the mean value of prediction for feature 4 slightly deviates from the true value, the true value is still within the 90 percent confidence interval. One interesting observation is that certain level of scatter is found before 2 years and getting smaller after 2 years for feature 6. This is probably because there is larger prediction uncertainty in the region before 2 years than its counterpart after 2 years in the trained GP-NARX model. At the beginning of the prediction, the model might not be so confident given such small values of inputs in that region. As the values continue to feed in, the prediction enters

a region where the model is more accurate and with less uncertainty.

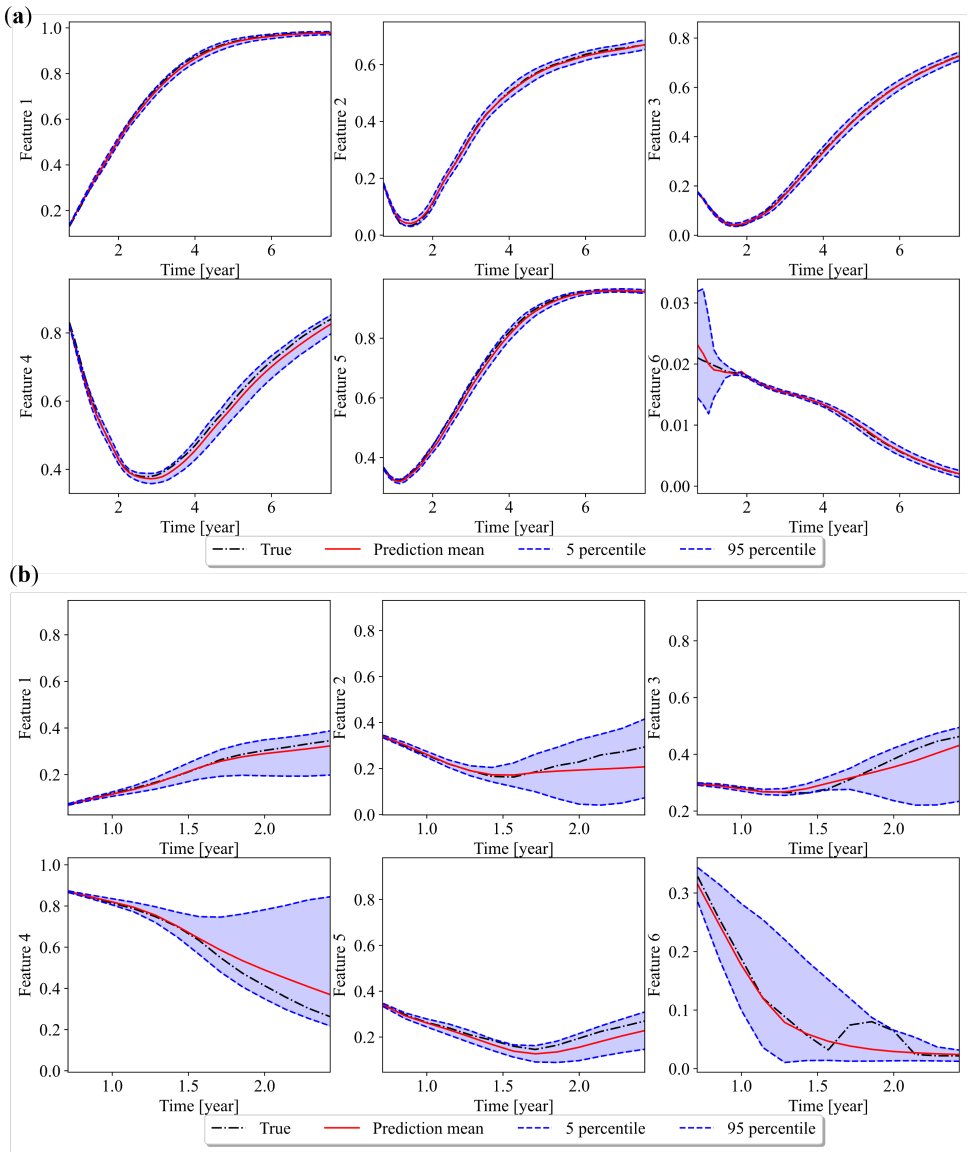

Figure 3.7. Multi-step ahead prediction result of case (a) and (b) in the latent space

Figure 3.7 (b) shows the prediction results for case (b). The mean prediction is not so accurate after 1.5 years. The confidence interval is wider than the prediction of case (a), which indicates that there is larger uncertainty in the prediction. During the multiple-step prediction, the error of prediction at single step can propagate to the next step and accumulates to larger error. Given there are more uncertainties in the prediction, the uncertainties accumulate resulting

in large confidence interval. Although the mean of prediction for case (b) is not as precise as case (a), the true value is still within 90 percent confidence interval, which indicates that the GP-NARX model can effectively capture the uncertainty in the prediction. There is also some non-linearity after 1.5 years for feature 6 and our model does not capture it properly. This might be related to the distribution of feature 6 as most numbers concentrates on small values less than 0.03 as described before in current section . Therefore, there are few samples in the range of 0.03-0.1 in the training set, or even the whole data set, leading to a poor prediction for the non-linear pattern in this range.

The difference between prediction results of case (a) and case (b) also shows the importance of quantifying the epistemic uncertainty of the surrogate model prediction, since it is difficult for a machine learning model to accurately predict the response for all regions. Based on the uncertainty quantification of the machine learning model prediction, we can then adaptively refine the surrogate model to ensure it is accurate in important regions.

3.4.4 Mapping GP-NARX predictions to corrosion morphology

The predicted results by the GP-NARX models in the latent space then are transformed back to corrosion morphology images using the CNN decoder. Two types of mean predictions are considered. For the first type, the surrogate model prediction uncertainty is considered in the prediction. 1000 realizations of corrosion morphology images for case (a) and case (b) are obtained from decoder at each time step. The mean of each pixel is then computed based on the uncertainty propagation and is plotted. It is referred to as the predicted mean. For the second type, the uncertainty in the surrogate model prediction is not considered. The mean (μ_{jk}) of GP-NARX model prediction is directly decoded and plotted. This is referred to as the decoded GP mean. Since the decoder is a nonlinear transformation, there is a difference between the two results. Figure 3.8 shows the accuracy comparison with the underlying true values for the two studied cases.

The results show that prediction results of the proposed CNN-GP-NARX surrogate model

are accurate. Like the GP-NARX prediction results in the latent space discussed above, the overall prediction for case (a) after decoder remains very accurate. The errors for both predicted mean and decoded GP mean are small. For case (b), the overall prediction is still accurate. The general morphology and corrosion area can be captured. But both the predicted mean and decoded GP mean slightly underestimate the evolution of the corrosion when the morphology gets sharp, and the corrosion depth grows rapidly. Furthermore, we can notice that the prediction mean is more accurate than the decoded GP mean from the error plot. This indicates that the error of the GP model mean prediction can be compensated by the GP model variance prediction through uncertainty propagation and the nonlinear transformer, decoder. Overall, the surrogate model can give accurate predictions for different corrosion morphologies and corrosion area.

Figure 3.9 plots the 5-th percentile and 95-th percentile images obtained from the 1000 corrosion morphology images decoded from the latent space after uncertainty propagation. For case (a), the 5-th percentile, mean and 95-th percentile are quite close to each other. This corresponds to a high confidence in the GP prediction result in the latent space. For case (b), the 5-th percentile shows the largest corrosion area as well as the corrosion depth with a similar corrosion morphology as the mean. The 95-th percentile shows the least corrosion area and the corrosion depth with a different morphology. This is also consistent with the wide confidence interval in the GP results in latent space. The comparison also shows the epistemic uncertainty (wide confidence interval) in the GP prediction results represent different corrosion evolution processes, i.e., different corrosion evolution speed with different corrosion morphologies. The uncertainty propagation process can thus reasonably capture the uncertainty in the prediction, as evidenced that the true value is contained in the prediction confidence interval.

3.5 CVAE-BLSTEN surrogate model results

Two variations of the physical constraint were considered. In the first version, the monotonic constraint in Eq. (3.13) was enforced on a pixel-by-pixel basis, while in the second

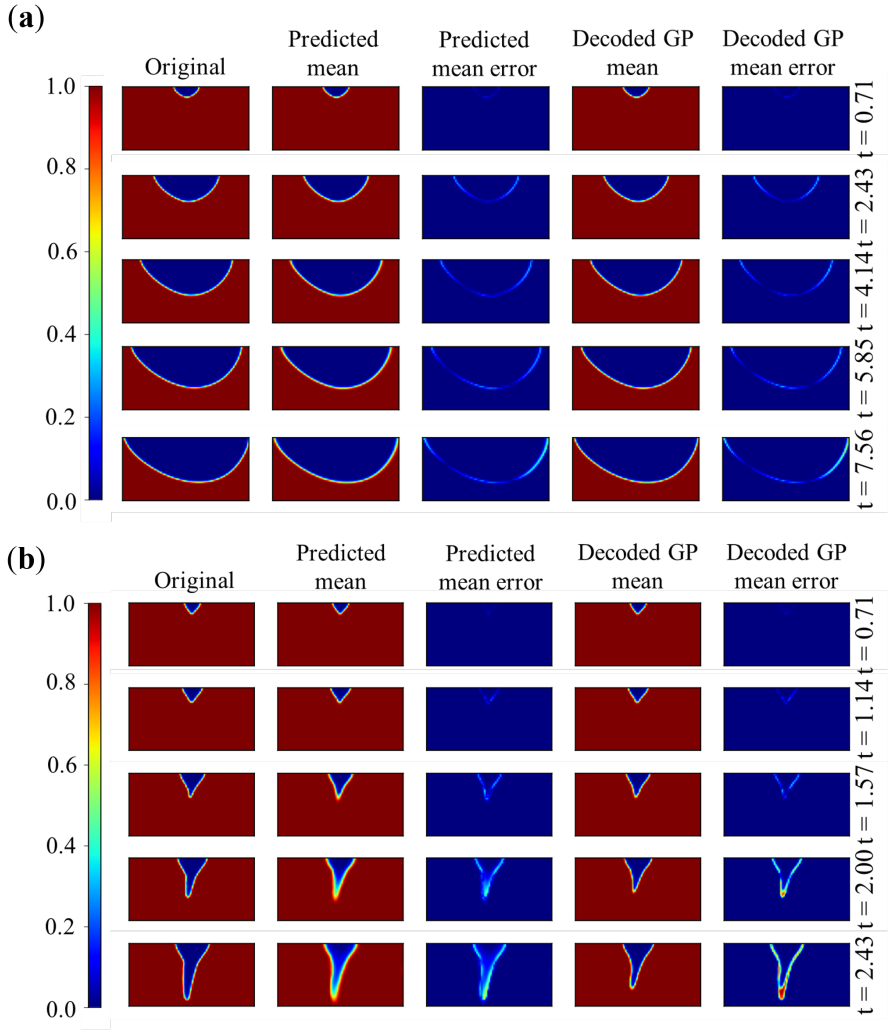

Figure 3.8. Multi-step ahead prediction result of case (a) and (b) in the image space

version, the constraint was enforced on the total corrosion (by summing the corrosion rate across all pixels). The reason for considering these two cases was that while the pixel-by-pixel approach captures the correct physics, it is prone to evolve spurious corrosion patterns originating from noisy predictions. The total corrosion constraint allows for small corrections of small spurious pixels while still encouraging the correct physics. An example of this behavior is shown in Fig. 3.10, where it can be seen that the pixel constraint allows a spurious corrosion pattern to grow discontinuously while the total corrosion constraint does not suffer from this. The two approaches were compared with the CNN-GP-NARX approach by computing the mean squared

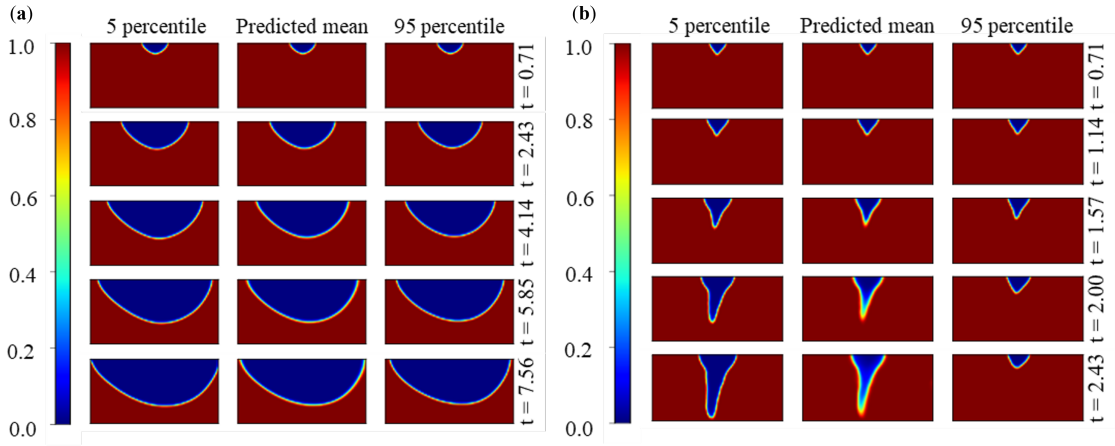

Figure 3.9. Multi-step ahead prediction distribution of case (a) and (b) in the image space

error (MSE) of the mean predictions across all test cases. Fig. 3.11 shows the MSE as a function of time and Table 3.1 presents the average of the MSE across time. As illustrated, the overall error of the BLSTEN-VAE approach is smaller than that of the CNN-GP-NARX approach. In particular, the BLSTEN-VAE approach with a physics constraint on the total corrosion results in a significant reduction in error. One observation is that the error of the BLSTEN-VAE approach is relatively flat across time while the CNN-GP-NARX's error tends to grow with time. This result is a consequence of the autoregressive approach used in the time evolution mechanism of the NARX algorithm which tends to accumulate error due to its recursive predictions. The BLSTEN algorithm is not autoregressive and, as a result, does not accumulate significant error with time.

Table 3.1. Average MSE of all test cases across 200 time steps for each method.

Method	Average MSE
CNN-GP-NARX	0.0125
BLSTEN-VAE - pixel	0.0084
BLSTEN-VAE - total	0.0066

One particular example that was hard to predict for the CNN-GP-NARX approach was case 251 with $\boldsymbol{\Theta} = [37.89, 6.05, 8.97, 4.76]$. Fig. 3.12 illustrates the results for case 251 for the

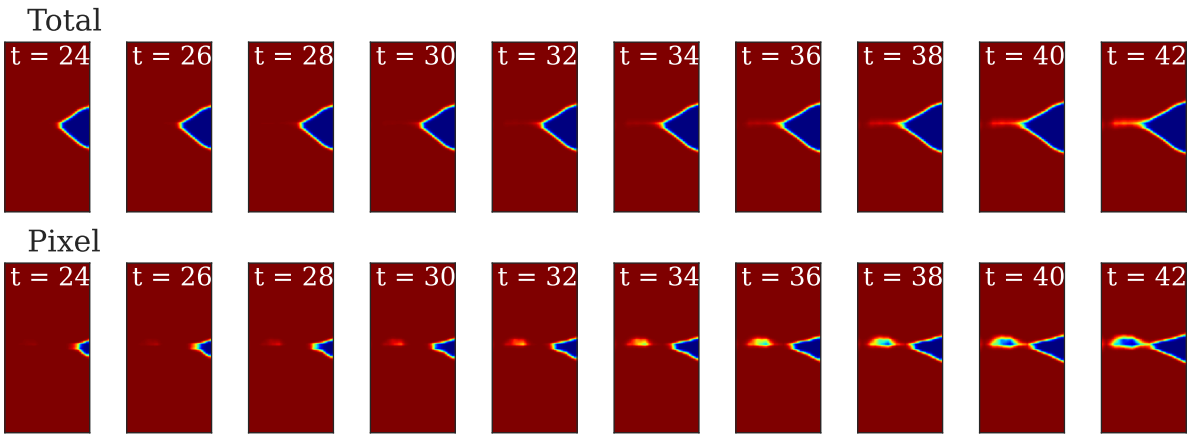

Figure 3.10. Example of corrosion pattern evolution with pixel-by-pixel constraint (bottom) and total corrosion constraint (top). Simulation time step is indicated in figure.

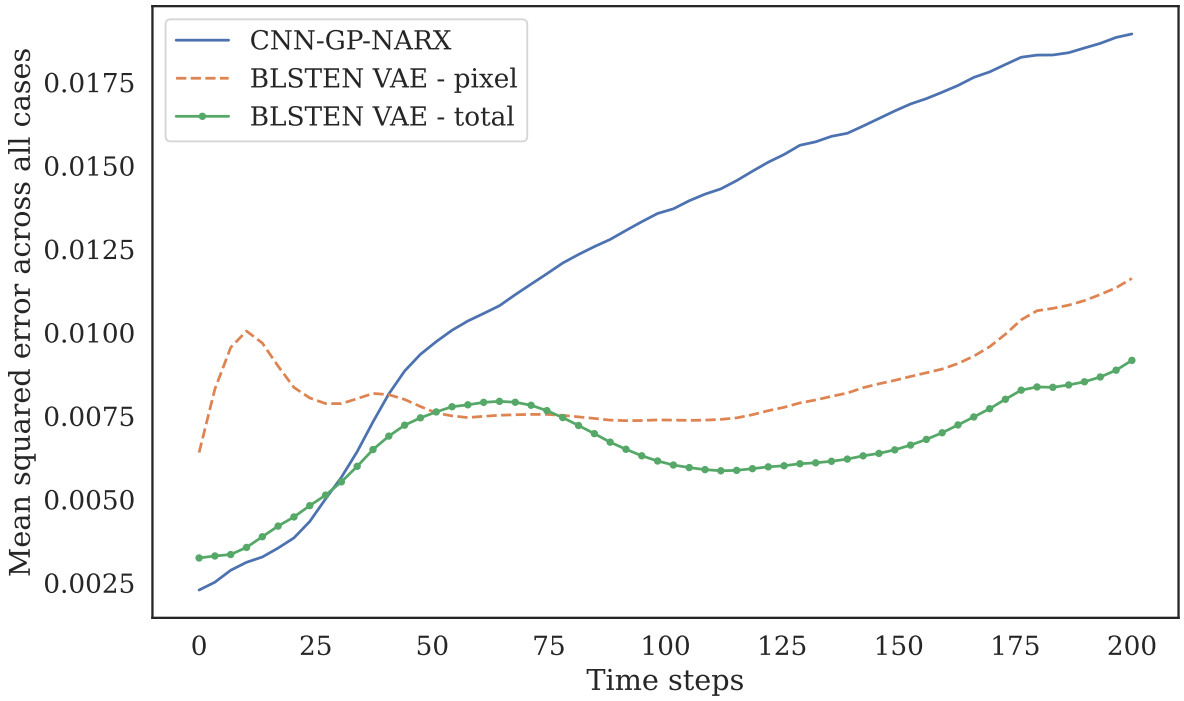

Figure 3.11. Comparison of MSE as a function of time for different methods.

CNN-GP-NARX approach and the BLSTEN-VAE (with the total corrosion constraint). To show the confidence interval bounds, the edges from the truth data were extracted using a Canny edge detection algorithm [20] and the predicted confidence interval was drawn around it. As shown, the CNN-GP-NARX prediction is fuzzy around the edges, and this epistemic uncertainty is expressed

in large 95% level confidence intervals. The area between the two-sided confidence interval is shaded in Fig. 3.12 to represent the boundaries of the predicted corrosion. The BLSTEN-VAE results show a much narrower confidence interval around the true boundary as well as a mean prediction that is much closer to the actual image. A similar behavior can be observed for cases 246 with $\boldsymbol{\Theta} = [44.14, 46.68, 4.68, 3.26]$ and 248 with $\boldsymbol{\Theta} = [-30.86, 34.18, 2.23, 4.46]$ which are presented in Fig. 3.13 and 3.14, respectively. These cases were chosen because they were challenging to predict and are representative of the three types of corrosion shapes observed. These results demonstrate that the BLSTEN-VAE approach is robust at predicting a variety of corrosion shapes with relatively high confidence.

3.6 Epistemic uncertainty propagation

Because of more economic computation cost, the CNN-GP-NARX model is selected for further probabilistic study in this thesis. Figure 3.15 gives an overview of the proposed accelerated corrosion-to-cracking simulation framework. As shown in Step 1 of Figure 3.15, a calibrated high-fidelity phase-field simulation model is used to generate corrosion morphology images for different training samples of external loads, reaction constant, and diffusion coefficient. These four parameters—mechanical normal stress, mechanical shear stress, reaction constant, and diffusion coefficient—in addition to the initial morphology, represent the different environmental conditions for the structure in service. The results of the simulation are corrosion morphology images over time. Then, the high-dimensional corrosion morphology images are mapped into low-dimensional data in latent space with a convolutional neural network (CNN) autoencoder (see Step 2 in Figure 3.15). Next, a Gaussian process regression model with a nonlinear autoregressive model with exogenous inputs, named GP-NARX, is utilized to learn the corrosion evolution dynamics in the latent space. GP-NARX is chosen because it can capture the uncertainty of the surrogate model prediction in a closed form, facilitating uncertainty quantification of the overall surrogate model prediction performance later. After that, the low-dimensional prediction results

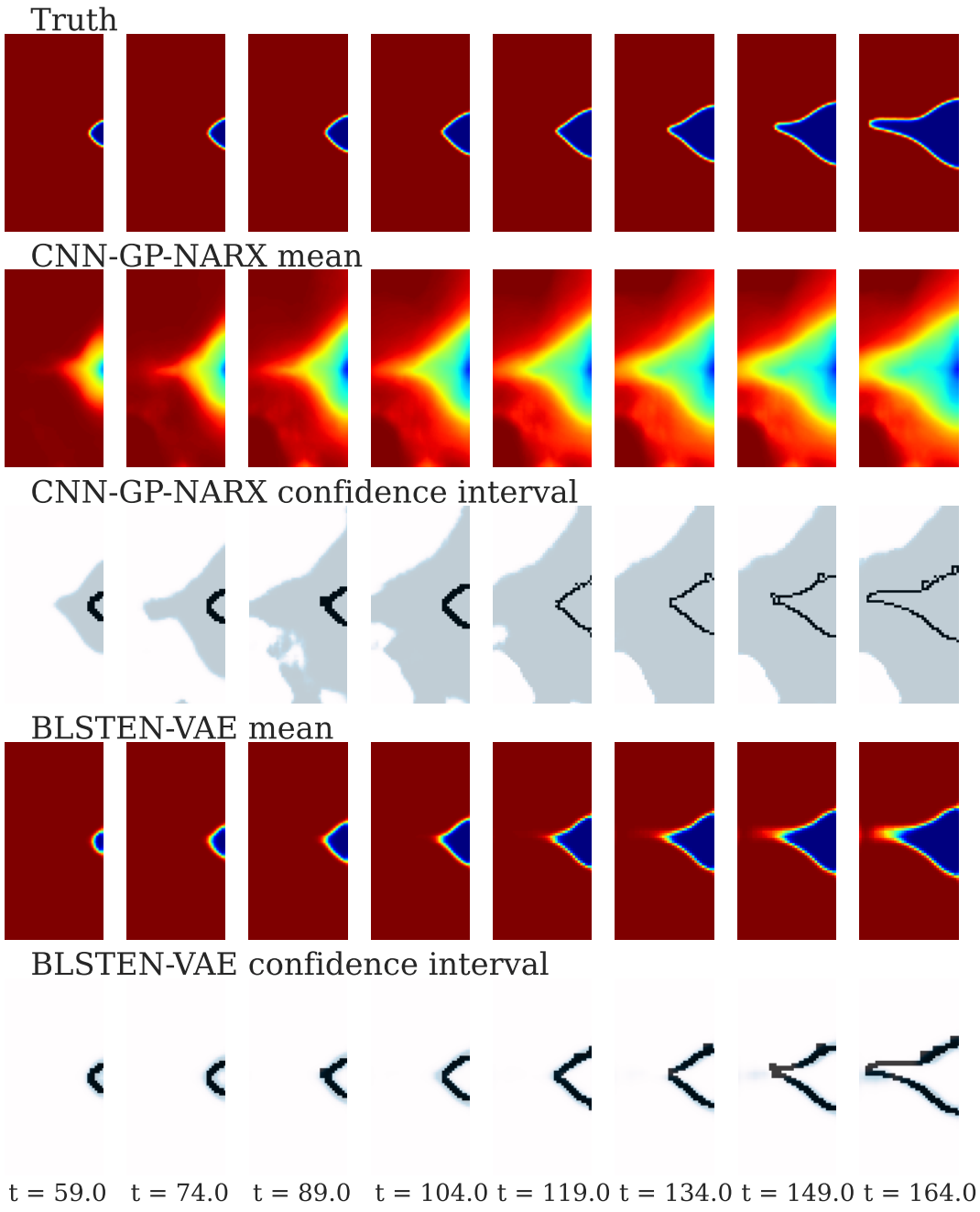

Figure 3.12. Results for test case 251. Shown: simulation reference (first), CNN-GP-NARX mean prediction (second), CNN-GP-NARX 95% confidence interval (third), BLSTEN-VAE mean prediction (fourth), and BLSTEN-VAE 95% confidence interval. Simulation time step is indicated at the bottom.

in the latent space are decompressed to the original high-dimensional corrosion morphology images with decoder trained together with autoencoder. Afterwards, the surrogate model is used

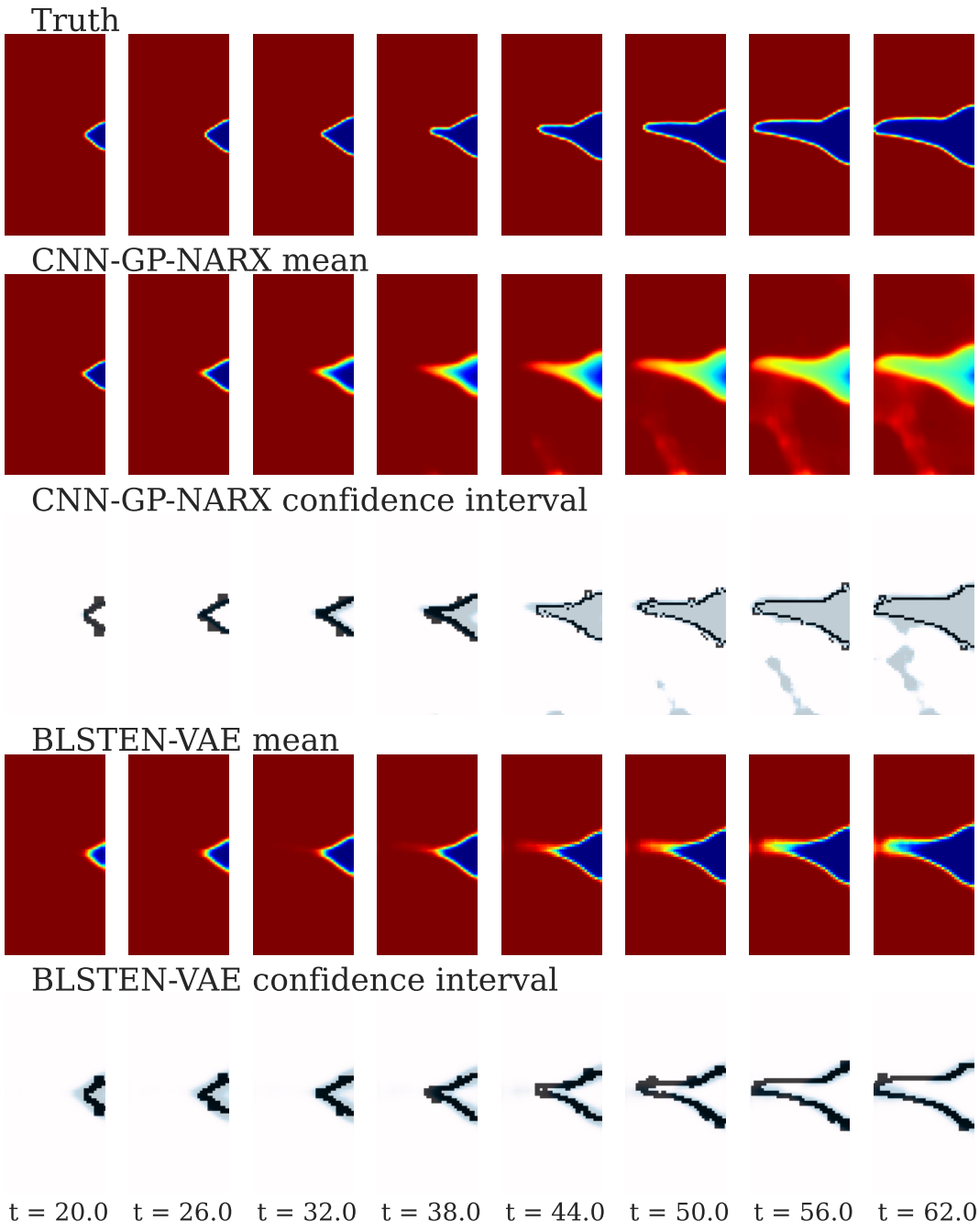

Figure 3.13. Results for test case 246. Shown: simulation reference (first), CNN-GP-NARX mean prediction (second), CNN-GP-NARX 95% confidence interval (third), BLSTEN-VAE mean prediction (fourth), and BLSTEN-VAE 95% confidence interval. Simulation time step is indicated at the bottom.

to complete Monte-Carlo simulations to quantify the uncertainty in the crack initiation time caused by the surrogate model uncertainty as Figure 3.15 shows in Step 3. Such uncertainties in

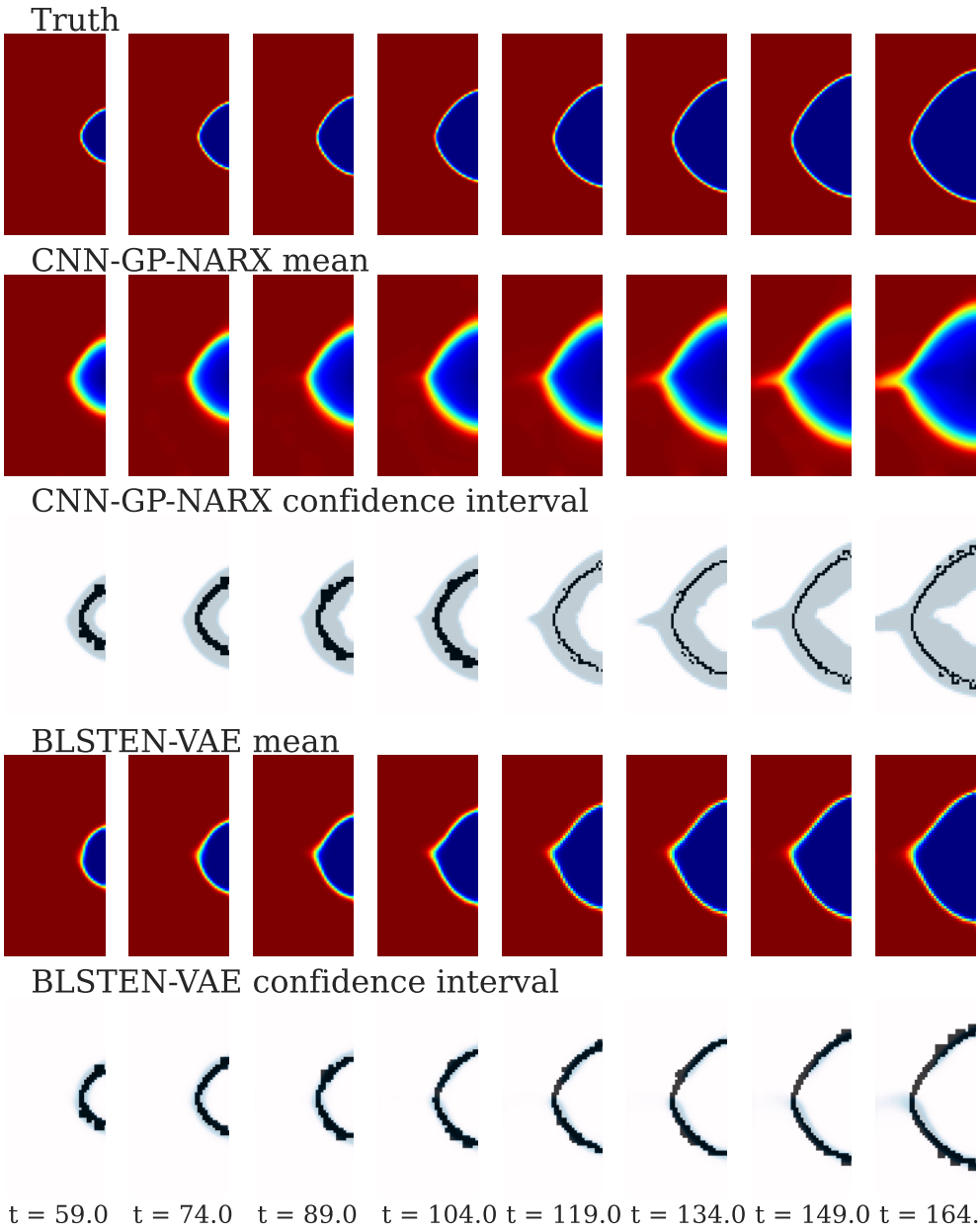

Figure 3.14. Results for test case 248. Shown: simulation reference (first), CNN-GP-NARX mean prediction (second), CNN-GP-NARX 95% confidence interval (third), BLSTEN-VAE mean prediction (fourth), and BLSTEN-VAE 95% confidence interval. Simulation time step is indicated at the bottom.

the latent space originally are propagated into the morphology space. Proposed SCC initiation criterion is then implemented on the Monte-Carlo simulation results to get the probability distribution function of the crack initiation time. With the highly efficient simulation capability,

the proposed framework can be extended to incorporate many other uncertainty sources in the future, such as uncertainty in crack initiation stage, uncertainty in the load condition, etc.

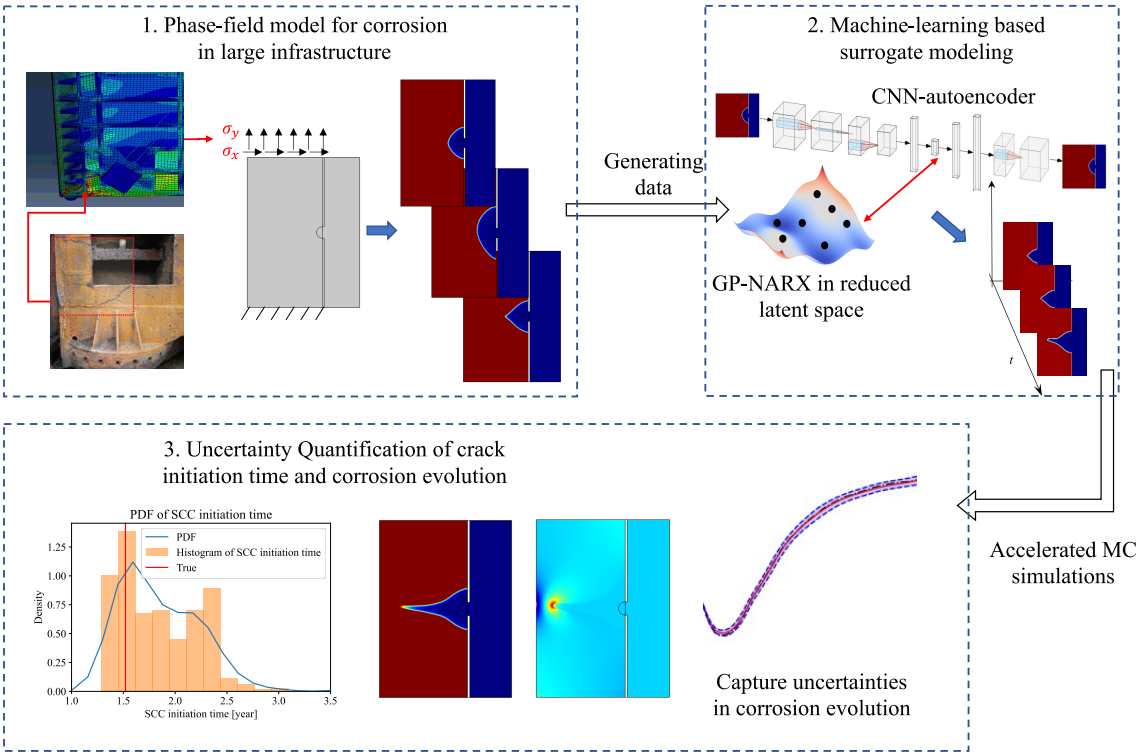

Figure 3.15. Overview of the proposed surrogate model-accelerated probabilistic analysis framework for corrosion-to-cracking prediction in large structures

The above presented CNN-GP-NARX based surrogate modeling method is hundreds of times faster than the traditional high-fidelity simulation of pitting-to-cracking process. In order to compare prediction performance to the original high-fidelity simulation, it is necessary to quantify the uncertainty in the surrogate model prediction. In this work, the uncertainty quantification of surrogate model prediction is computed directly using Monte Carlo simulation (MCS) since the constructed surrogate model can run very efficiently. In MCS, a large number of MCS samples are first generated for the initial steps of the GP-NARX models. The initial samples are then propagated to the latent responses at later time steps, by following the NARX framework discussed above. The generated latent-space samples at each time step are then transformed back to corrosion morphology images using CNN autoencoder. For each corrosion

morphology image, the crack initialization behaviors are analyzed using the method presented in Sec. 2.3. Based on that, we obtain statistical information about whether, when, and where the corrosion damage triggers the crack initiation.

Stress based SCC initiation criterion is applied to further propagate the uncertainty in the corrosion morphology prediction to SCC initiation time and location. To show the SCC initiation prediction for different cases, case (c) as Figure 3.16 shows is added as there is no SCC initiation in case (a). The input parameters of the phase-field model for case (b) and case (c) are -30.86 and -24.61 MPa for the shear stress, 34.18 and 12.30 MPa for normal stress, 2.23 and 0.39 for reaction constant, and 4.46 and 1.76 for diffusion coefficient, respectively. Figure 3.17 shows the probability density function and cumulative density function of the crack initiation time and location for case (b) and case (c).

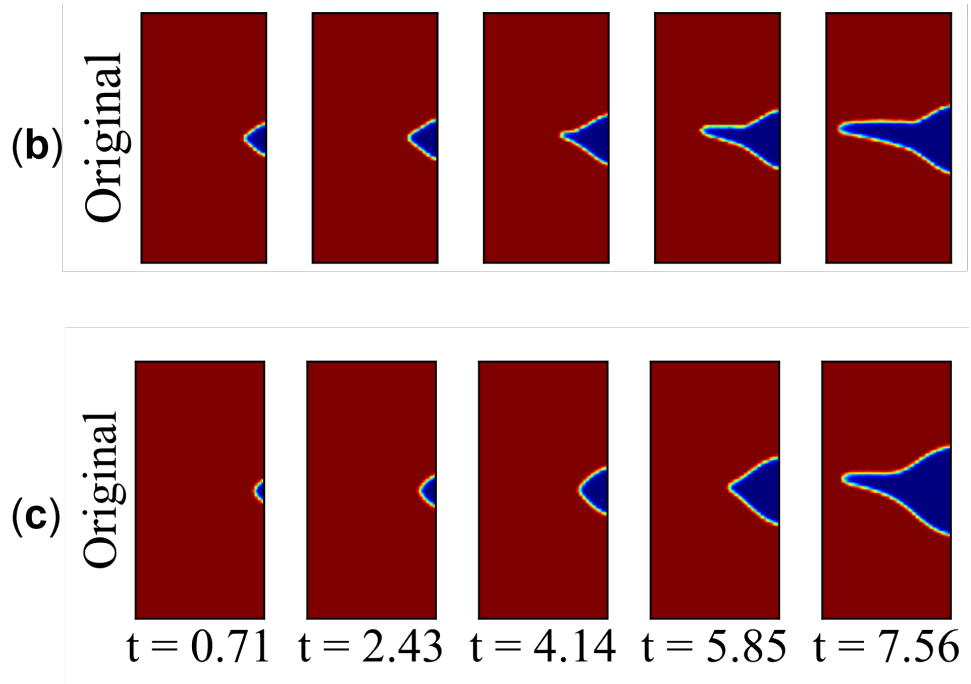

Figure 3.16. Corrosion evolution images for case (b) and (c)

The prediction of SCC initiation time and location is accurate for case (b) as the predicted values with the largest probability densities are very close to the true value. For case (c), the predicted SCC initiation time is conservative while the predicted location is still accurate. We

can find that the average SCC initiation time is earlier than the true value for case (c). Comparing the distributions of case (b) and (c), it may be seen that the distribution of SCC initiation time is more concentrated for the case (b). One reason could be that and the reaction constant and the stress acting on case (b) is larger than that of case (c), resulting a faster corrosion rate. When the corrosion speed is faster, the potential SCC initiation and propagation is also faster. Therefore, the time range of SCC initiation time is also smaller in the faster case, i.e., the SCC initiation time is more concentrated for case (b) than case (c) in MCS. The SCC initiation location distribution shows that the SCC initiation location is also more concentrated at certain area for case (b) than case (c).

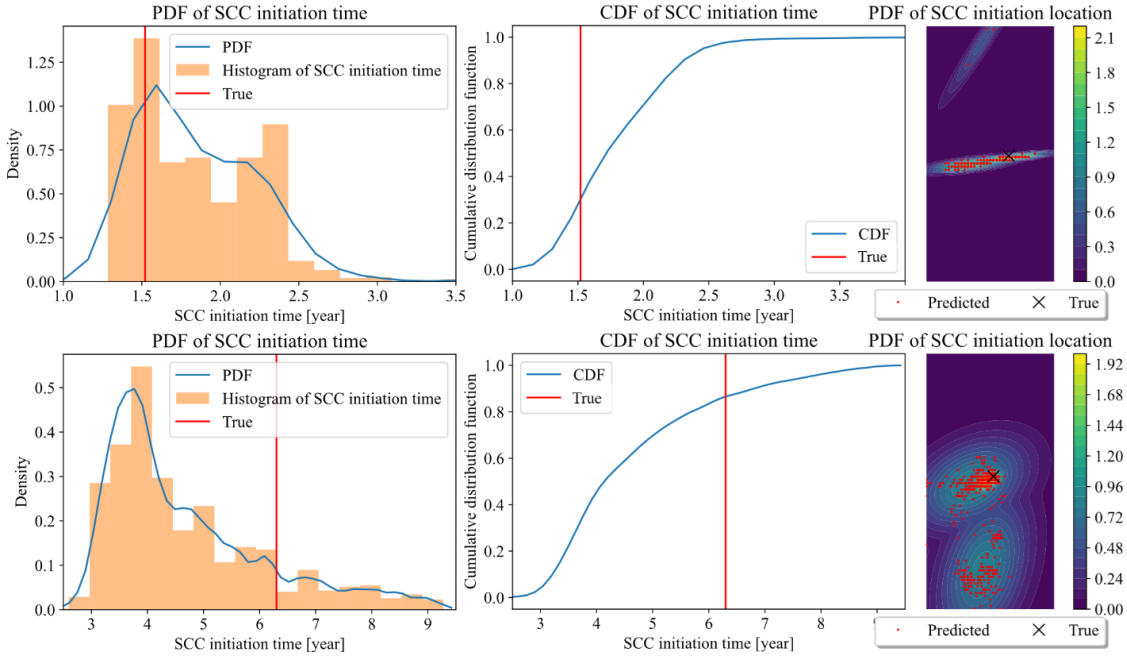

Figure 3.17. SCC initiation time and location distribution for case (b) and case (c)

3.7 Conclusions

The proposed surrogate models, i.e., CNN-GP-NARX and VAE-BLSTEN can accurately predict the corrosion evolution. The proposed surrogate modeling methods reduces the computational cost significantly, which enables much more rapid predictive assessments. It

also accurately captures the interface, which is the material boundary in the corrosion process. A novel combination of an operator learner (i.e., BLSTEN) and a nonlinear dimensionality reduction technique (i.e., VAE) with a constraint based on the physical phenomenon of irreversible corrosion growth to construct a surrogate model that can be used to forecast corrosion shape. The VAE-BLSTEN approach was demonstrated to be more accurate, robust and more computationally-expensive than the established CNN-GP-NARX algorithm by avoiding error accumulation inherent in autoregressive models and through the introduction of physics-inspired constraints.

A computational framework for probabilistic analysis of corrosion-to-crack transitions is developed and explored with CNN-GP-NARX. The epistemic uncertainty in the surrogate model is propagated to crack initiation time and location, such that the distribution of crack initiation time and location is calculated. The proposed framework can also consider other uncertainty sources in the future.

3.8 Remarks

Material for this chapter was published in the following articles:

[1] **Guofeng Qian**, Karnpiwat Tantratian, Lei Chen, Zhen Hu, and Michael D Todd. A probabilistic computational framework for the prediction of corrosion-induced cracking in large structures. *Scientific Reports*, 12(1):20898, 2022.

[2] David A Najera-Flores, **Guofeng Qian**, Zhen Hu, and Michael D Todd. Corrosion morphology prediction of civil infrastructure using a physics-constrained machine learning method. *Mechanical Systems and Signal Processing*, 200:110515, 2023

Chapter 4

Corrosion Reliability Analysis with Adaptive Surrogate Modeling

4.1 Abstract

Stress corrosion cracking (SCC) initiation is usually simulated at the mesoscale, and these computations are usually expensive. This is made more computationally challenging or impossible when such simulations are coupled with a macroscale structural model required for reliability analysis, due to the sources of aleatory uncertainty from both scales. This work tackles this computational barrier to perform physics-based corrosion reliability analysis of large structures using mesoscale simulations via a novel, adaptive surrogate modeling framework. A global surrogate model of the structure is first constructed from a finite element (FE) mechanical model to propagate various sources of input uncertainty at the macroscale to the local stress responses. After that, a mesoscale surrogate model is constructed from phase-field (PF) simulations to predict the failure probability of a given location by accounting for uncertainty in both the macroscale and mesoscale models. In order to guarantee the accuracy of the mesoscale surrogate model and reduce the number of PF simulations, an adaptive surrogate modeling method is proposed using adaptive importance sampling (IS) and active learning to refine iteratively the surrogate model in critical regions. Corrosion reliability analysis of a miter gate structure is adopted to demonstrate the efficacy of the proposed method. The result shows that the proposed framework can efficiently and accurately generate a failure probability map for a large structure

like a miter gate based on computationally expensive mesoscale PF simulations. In addition, the proposed method is more accurate and converges faster than existing surrogate model-based reliability analysis algorithms.

4.2 Introduction

SCC is a crack initiation and propagation process under tensile stress at the surface of the material in a corrosive environment. SCC in infrastructure is dangerous because it can lead to unexpected brittle failure. Multiple failures of large structures have occurred because of SCC, such as the roof collapse at the Uster indoor swimming pool in Switzerland [155], partial collapse of the Berlin Congress Hall [66], the failure of a pre-stressed concrete bridge in Slovenia [152], and the collapse of a railway overpass at Berghausen, Germany [34].

On one hand, SCC initiation is influenced by the mechanical load state. On the other hand, the electrochemical behavior is also influenced by environmental conditions like the contact water/fluid chemistry, the temperature, and other environmental or operational factors [3]. SCC and corrosion are almost impossible to gauge accurately in a deterministic sense because of the inevitable variability in all these factors. However, probabilistic studies together with a physics-informed degradation model can provide a reasonable estimation of damage status and the remaining useful life of the structures [162].

Most corrosion reliability analyses use corrosion growth models based on empirical formulas [79, 139, 163, 140, 26]. One advantage of such empirical formula-based models is that they usually require little computational effort to evaluate, which facilitates reliability analysis of large civil infrastructure. The empirical model-based SCC reliability analysis methods, however, have two major limitations. First, it is difficult to properly propagate uncertainty from reasonable uncertainty sources to system-level functional reliability assessment with such models, since there is no physical meaning in most terms of the empirical formulas. Second, empirical models require historical data to calibrate and construct. For large civil infrastructures such the as miter

gates studied in this work, such historical data are very difficult to find or not even available. In this situation, it is more desirable to develop a physics-based reliability analysis method using computer simulations constructed according to physical laws, which could be more readily updated if validation data become available.

The PF model approach has been used in the literature to simulate pitting corrosion and SCC initiation [7, 98]. It shows great potential and flexibility in simulating the morphological evolution of the pitting corrosion process and SCC initiation process [72]. The model involves multiple coupled partial differential equations (PDEs) including the Allen-Cahn equation describing phase transition and the Cahn-Hilliard equation describing the evolution of the molar concentration of metal atoms [90]. The PF model considers the influence of mechanical stress by coupling a stress equilibrium PDE into the model [98, 118]. Nevertheless, the model is intrinsically computationally expensive as it consists of multiple coupled PDEs. It is still computationally prohibitive to use the PF model directly–coupled PDE simulation itself is time-consuming–for reliability analysis, which usually requires thousands of runs of the full system model. In addition, the PF model is a mesoscale model while the system (i.e., miter gates in this work) is at the macroscale, resulting in a complex multi-scale problem. A new reliability analysis framework is needed to incorporate the local mesoscale modeling into the global macroscale simulation while keeping a reasonable computational cost for system reliability analysis of large civil structures (such a miter gates) with respect to the SCC failure mode.

This work aims to develop a physics-based corrosion reliability analysis method using multi-scale simulations and adaptive surrogate modeling. To achieve this goal, the PF corrosion model and global FE model are developed for a typical miter gates. Then, Gaussian process regression (GPR)-based surrogate models are constructed for both the local corrosion model and global FE model to accelerate the modeling process. After that, an adaptive surrogate modeling technique incorporating IS is proposed to efficiently compute the failure probability of any given stress condition. Based on this, the multi-scale surrogate models are integrated to evaluate efficiently the failure probability at any location on a miter gate due to SCC. The results show that

the proposed reliability analysis method successfully generates a risk map over the entire miter gate structure with a reasonable computational cost. The proposed adaptive surrogate modeling method shows fast convergence compared to the existing method. The main contributions of this work can be therefore summarized as (1) a novel framework that connects a macroscale structural analysis model with mesoscale PF-based SCC analysis model for corrosion reliability analysis of large civil infrastructure; (2) an adaptive surrogate modeling method that integrates Gaussian mixture model, importance sampling, and surrogate modeling-based on active learning to efficiently construct surrogate models for corrosion reliability analysis; (3) integration of surrogate models of multi-scale simulations for reliability analysis at macroscale using mesoscale analysis under uncertainty; and (4) application and demonstration of the proposed methods using the practical application of a miter gate, for which corrosion is a common problem.

The remainder of this chapter is organized as follows: Section 2 presents a literature survey of the current status of corrosion reliability analysis and introduces a PF-based pitting corrosion simulation model. Section 3 describes the proposed surrogate modeling method for corrosion reliability analysis. Section 4 uses a practical application example of a miter gate to demonstrate the proposed framework. Finally, Section 5 concludes and discusses the presented work.

4.3 Background

4.3.1 Literature survey of probabilistic SCC simulation

As shown in Fig. 4.1, the whole evolution process of stress corrosion cracking damage may be broadly classified into four stages, namely (1) corrosion initiation, (2) corrosion growth, (3) pit-to-SCC transition, and (4) crack propagation.

In the past decades, numerous models have been developed for corrosion damage modeling in these different stages. The corrosion initiation stage (i.e., stage 1 in Fig. 4.1) is described by the time till the local corrosion initiates. Corrosion initiation time for steel is found to be

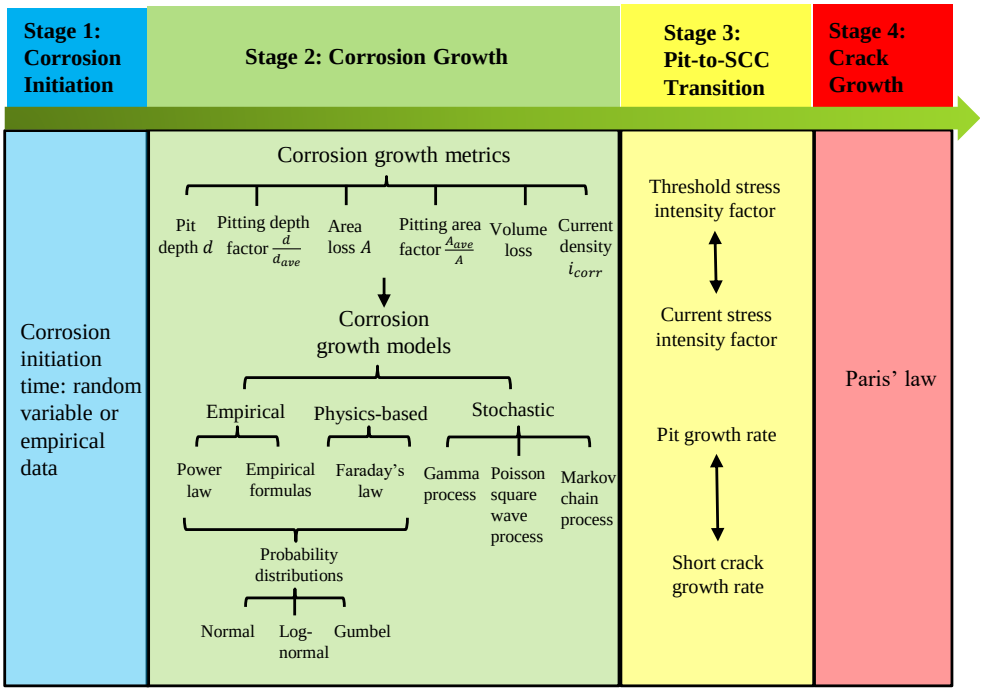

Figure 4.1. Four stages in stress corrosion cracking

dependent on temperature, the concentration of metal cation, and the potential drop across the interface [83, 85]. The detailed electrochemical mechanism of corrosion initiation, however, is not well understood yet. Due to the lack of a physics-based model, the corrosion initiation time is usually assumed to be a random variable based on historical or experimental data [132, 142]. Particularly, in reinforced concrete structures, corrosion is assumed to initiate when the chloride concentration on the steel surface is greater than the chloride threshold [125].

In the second stage, corrosion growth is represented with different metrics as shown in Fig. 4.1. Pit depth represents the maximum depth of a local corrosion site. The corresponding pitting depth factor is defined as the pit depth divided by the average penetration based on uniform corrosion [56]. The cross-sectional area loss is often used to describe the corrosion growth of reinforcement steel in reinforced concrete structures. The associated pitting area factor is defined as the ratio between the minimum cross-sectional area and the area based on uniform corrosion [163]. Volume loss is another commonly used metric for corrosion growth. Most corrosion is considered an electrochemical process. The corrosion current density describes the

amount of charge per unit of time that flows through a unit area of a chosen cross-section. The corrosion current density is also called corrosion rate and is related to the thickness reduction rate in uniform corrosion [50]. Pitting corrosion current density is defined by multiplying a coefficient and the maximum pit depth. It is usually approximated with a linear relation with current density [138].

Pitting corrosion growth models in general can be broadly classified into empirical, physics-based, and stochastic models as depicted in Fig. 4.1. Empirical models are usually developed based on historical observations rather than physics theories. For instance, power-law models have been proposed to characterize the variability of corrosion growth [79]. The time-variant corrosion depth is modeled as a constant power of time. Besides, there are various empirical formulas describing the evolution of the pitting depth factor [139], the pitting area factor [163], and the corrosion current density [140]. The environmental factors that might influence corrosion growth are also considered in some empirical equations [26]. For the physics-based model, Faraday's law is one of the most widely used. In Faraday's law, the pit is assumed to grow at a constant volumetric rate as follows [65]

$$\frac{dV_o}{dt} = \frac{MI_{\rho^0}}{nF_r\omega}\exp\left(\frac{-\Delta H}{RT}\right), \tag{4.1}$$

where V_o is the volume of the metal, M is the molecular weight, n is the valence, F_r is the Faraday's constant, I_{ρ^0} is the pitting current coefficient, ω is the density, ΔH is the activation enthalpy, R is the universal gas constant, and T is the absolute temperature. The exponential term is introduced to take the effect of temperature into consideration.

To account for uncertainty in empirical models and physics-based models introduced above, model parameters of aforementioned models are usually modeled as random variables represented by probability distributions such as normal, lognormal, Weibull, and Gumbel [55, 125, 132]. Besides describing the corrosion growth metric as a determined function of random variables, we can also use stochastic processes for probabilistic corrosion modeling. The

commonly used stochastic process models include the Gamma process, Poisson square wave process, Markov chain process, and other stochastic processes [55, 14, 147, 119].

The third stage is the transition from pit to stress corrosion cracking initiation. There are two criteria used to describe this process. The transition process is actually a competition between pit growth and cracks growth. One criterion is to compare the current stress intensity factor approximated from the empirical formula with the threshold stress intensity factor [142]. The other criterion is to compare the pit growth rate from the corrosion growth model with the crack growth rate based on Paris' law assuming that the current pit shape is a short crack [132]. After the transition stage, the crack propagation model is assumed governed by Paris' law [142].

Pitting corrosion reliability analysis in different kinds of structures are studied in recent years. Among the 50 reviewed papers, 27 applications are about reinforced concrete structures and pipelines, and 5 studies are applied to complex steel structures such as aircraft structures, ships, or offshore structures. Almost no application concerns about large inland waterway steel infrastructures, such as miter gates, which are the focus of this work. Furthermore, most corrosion growth models used in corrosion reliability studies are empirical formulas. Even though Faraday's law is based on physical principles rather than empirical data, as mentioned above, it does not consider the dynamic nature of equilibrium or the activation energy barrier in an electrochemical system. More advanced physics-based corrosion growth models need to be incorporated for predicting corrosion growth and the potential SCC initiation, although a more complicated simulation model will bear greater computational costs in reliability analysis.

Aiming to analyze corrosion damage of miter gates, we have developed a physics-based SCC simulation model using the PF method in our previous research [118]. In the following section, we first briefly review the developed high-fidelity SCC simulation model. After that, we discuss how the developed model is applied to the corrosion reliability analysis of miter gates and the associated challenges that are addressed by the proposed method in this work.

4.3.2 PF simulation of corrosion

The localized corrosion process is considered to start from the local breakage of the passive film which is generated naturally on the surface of the metal, protecting the metal from corrosion, as shown in Fig. 4.2. As the metal is corroded, the metal cations (M^+) and the electrons are produced. The metal cations are further diffused into the electrolyte and electrons will move to the cathodic area. There is always mechanical loading during the service life for most infrastructures. Nonetheless, mechanical loading changes the chemical potential of the electrode (metal), affecting the corrosion process.

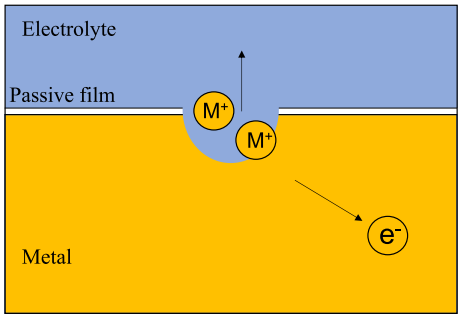

Figure 4.2. Schematics of stress corrosion

PF simulation

A continuous PF parameter ξ is used to describe the interface between electrolyte and electrode. The evolution of ξ is dependent on two parts: the interface energy and the electrode reaction. The electrode reaction rate is described by the classic Butler-Volmer kinetics. The influence of mechanical stress on corrosion is taken into consideration by the change to the generalized chemical potential. The PF equation proposed by Qian et al. [118] is applied as Eq. (4.2) below

$$\frac{\partial \xi}{\partial t} = -L_\sigma \left(g'(\xi) - \kappa \nabla^2 \xi \right) - L_\eta h'(\xi) \left(\exp \frac{(1-\alpha)\eta_a}{RT} - \bar{c}_+ \exp \frac{-\alpha n F_r \eta_a}{RT} \right), \tag{4.2}$$

where $\xi = \bar{c}$ is the order parameter physically corresponding to the dimensionless concentration

of the metal such that $\xi = 1$ in the metal and $\xi = 0$ in the electrolyte solution. L_σ represents the interfacial mobility and L_η represents the reaction coefficient which can be calibrated by the experimental data. η_a represents the activation over-potential. R is molar gas constant. T is the temperature. F_r is Faraday's constant.

On the other hand, corrosion also changes the strain distribution as fully corroded metal ("liquid") cannot support stress. The equivalent elastic strain tensor considering the solid-liquid interface is modified as Eq. (4.3)

$$\varepsilon^{eq} = p(\xi)\varepsilon^e_{ij} = p(\xi)\left\{\frac{1}{2}\left(\frac{\partial v_i}{\partial x_j} + \frac{\partial v_j}{\partial x_i}\right)\right\}(i,j = 1,2,3), \tag{4.3}$$

where v_i and v_j are displacement components, $p(\xi)$ is an interpolation function to smooth the discontinuity in the interface and also satisfies $p(0) = 0$ and $p(1) = 1$. Note that the Eqs. (4.2) and (4.3) are fully coupled, which means that the corrosion behavior and the stress or strain response in the system are fully coupled. Combining Eq. (4.2), Eq. (4.3), and the Nernst-Plank equation, we may get the major governing equations for the PF simulation for corrosion.

Pit-to-crack transition

As the pitting corrosion grows, SCC might initiate due to stress concentration [100] under some load conditions. The proposed PF simulation can also capture SCC initiation process as shown in Fig. 4.3 because we coupled mechanical stress in Eq. (4.2) to induce the influence of stress on corrosion. As corrosion depth gets larger and the morphology gets sharper, the stress concentration on the tip location is more severe than the surrounding area, leading to a sharper morphology and stronger stress concentration and higher likelihood of SCC initiation.

The SCC initiation criterion is applied based on the von Mises yield criterion. The pit-to-crack transition is assumed to happen when the stress in the structure reaches the von Mises yield criterion. The concentrated stress level at the pit tip location is approximated by the

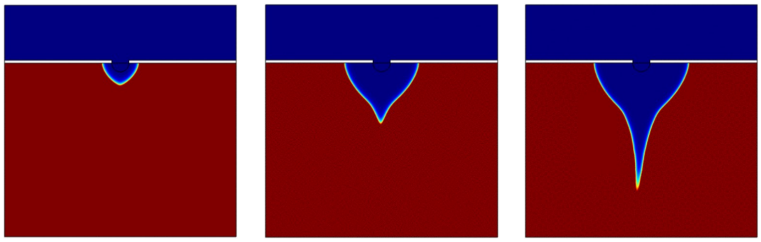

Figure 4.3. Pit evolution and pit-to-crack transition

stress concentration Eq. (4.4) [118].

$$\sigma_x = \sigma_{norm}\left(1+2\sqrt{\frac{c_d}{\rho}}\right), \tag{4.4}$$

where c_d represents corrosion depth and ρ represents the curvature radius at the bottom of corrosion pits. Both curvature radius ρ and corrosion depth a are calculated from the corrosion morphology.

4.3.3 Corrosion reliability analysis of miter gates using physics-based simulations

As shown in Fig. 4.4, pitting corrosion is one of the most common and significant deterioration types for miter gates operated in inland waterways. SCC could be initiated under tensile stress during the operation, which can lead to abrupt and unexpected failure of components. Additionally, other types of damage modes can also evolve when SCC initiates, leading to multiple damage modes and cascading failures. Corrosion reliability analysis using physics-based simulation allows us to forecast the damage evolution of miter gates, and thus proactively prevent failures through risk-informed maintenance optimization and planning.

In order to use the physics-based PF simulation model at the mesoscale (see Sec. 4.3.2) for reliability analysis of miter gates, a macroscale structural analysis simulation model is needed to predict the stress response of the miter gate under different load conditions. To this end, a high-fidelity FE model of the Greenup miter gate has been developed as shown in Fig. 4.5. This FE model has been validated in the pristine condition with strain sensor readings in previous

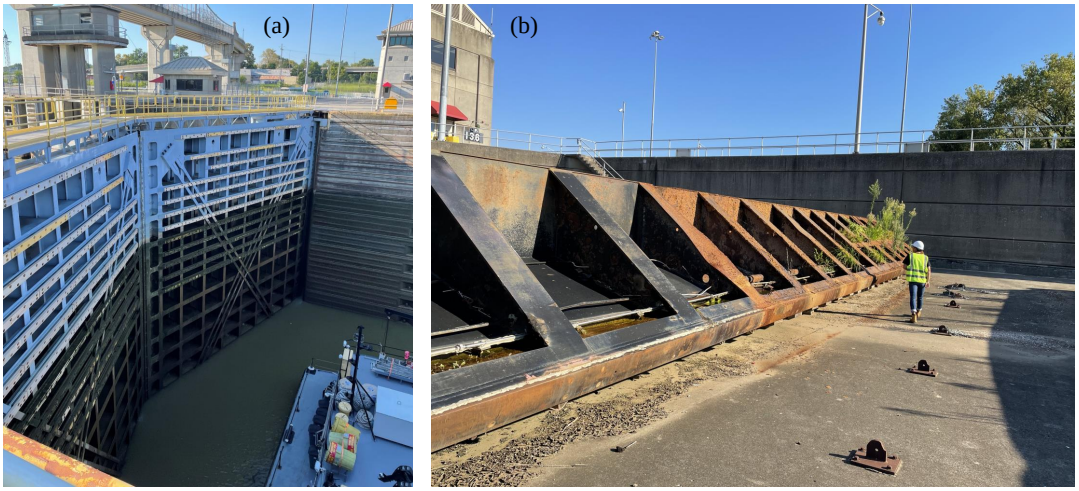

Figure 4.4. (a) A miter gate in operation; (b) A retired miter gate with serious corrosion

studies [44]. The whole miter gate is discretized into 64919 shell elements in ABAQUS. The 4-node, reduced integration shear element is used. To keep the most information about the stress field, the stress response at the single integration point in each element is extracted and saved. 64919 integration point locations, denoted as Ω_d, are fixed since the FE model mesh remains the same.

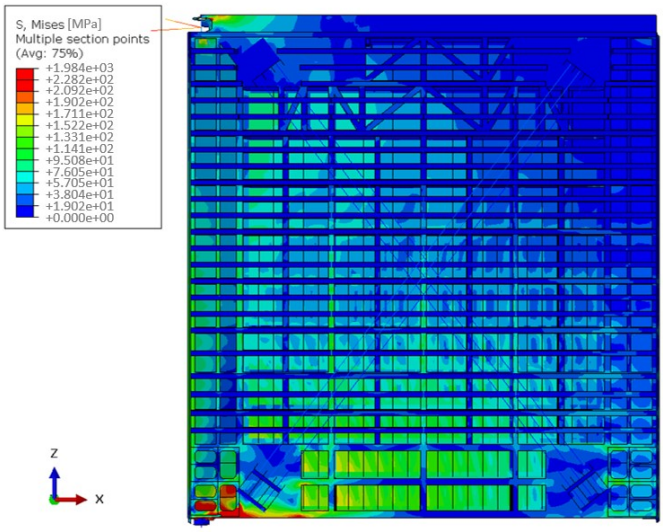

Figure 4.5. The FE model of the Greenup miter gate

The predicted stress response at these 64919 fixed locations $\mathbf{d} = [d_x,\ d_y,\ d_z] \in \Omega_d$ from

the macroscale structural analysis model can be mathematically represented as

$$[S_x,\ S_y,\ S_z] = F(A,\ \mathbf{V},\ \mathbf{d}), \forall \mathbf{d} \in \Omega_d, \tag{4.5}$$

where $\mathbf{d}$ represents any given point/location in the fixed location/point set Ω_d as defined above, $\mathbf{V} = [V_u, V_d]$, V_u and V_d are respectively the upstream and downstream hydraulic water heads, S_x, S_y, S_z are stress responses in three directions as indicated in Fig. 4.5, $F(\cdot)$ stands for the high-fidelity FE model, and A is the gap length representing a loss of contact between the gate and the wall quoin block near the bottom of the gate. The gap length is one of the common damage modes that are related to corrosion in the long term. It can lead to load redistribution on the gate and is usually determined based on inspection data by USACE engineers [157] or through structural health monitoring.

For any given location on the gate, the local corrosion growth is simulated as a two-dimensional plate using the PF model summarized in Sec. 4.3.2. As illustrated in Fig. 4.6, the right side of the plate is fixed and the left side is subjected to normal and shear stress. The interface is covered with a passive film that can stop the corrosion process except in the middle breakage area. The mechanical stress load as well as the reaction constant and the diffusion coefficient from the environment are the major factors that affect the corrosion behavior [118]. Based on the SCC initiation criterion presented in Sec. 4.3.2 and the macroscale structural analysis model, we define the SCC initiation time T_c at a given location $\mathbf{d} \in \Omega_d$ on the miter gate as

$$T_c(\mathbf{d}) = P_a(F(A,\ \mathbf{V},\ \mathbf{d}),\ \theta), \tag{4.6}$$

where $P_a(\cdot)$ represents PF simulation model, θ is a vector of PF model parameters including the reaction constant and the diffusion coefficient.

In miter gate corrosion reliability analysis, the failure event is defined as the SCC initiation time being less than a time of interest T_e, i.e., $T_c < T_e$. For a given spatial location $\mathbf{d} \in \Omega_d$ on the

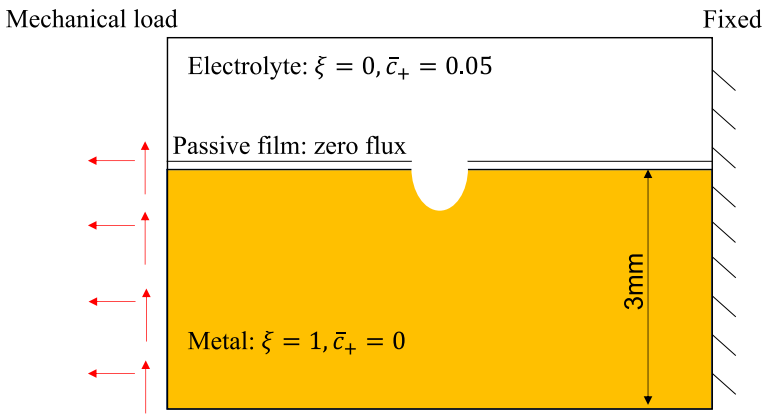

Figure 4.6. The implementation of PF corrosion model

gate, the task of reliability analysis is therefore to compute the following probability of failure

$$\begin{aligned} p_f(\mathbf{d}) &= \Pr\{T_c(\mathbf{d}) = P_a(F(A,\, \mathbf{V},\, \mathbf{d}),\, \theta) \leq T_e\} \\ &= \iiint\limits_{P_a(F(A,\, \mathbf{V},\, \mathbf{d}),\, \theta) \leq T_e} f_A(a) f_{\mathbf{V}}(\mathbf{v}) f_\theta(\theta) da\mathbf{dv}d\theta, \end{aligned} \tag{4.7}$$

where A, $\mathbf{V}$, and θ are random variables that may affect the SCC initiation time, $f_A(a)$, $f_{\mathbf{V}}(\mathbf{v})$, and $f_\theta(\theta)$ are respectively the probability density function (PDF) of the random variables.

Note that the PF model parameters θ are greatly influenced by the water level $\mathbf{V}$ due to the difference in the corrosion mechanism for under-water and above-water scenarios. Different statistical distributions should be used for these two different scenarios. In this work, when a location $\mathbf{d} \in \Omega_d$ is under the water line, θ is represented as θ_{ud}. Otherwise, it is represented as θ_{ab}. Based on this representation, for spatial locations $\mathbf{d} \in \Omega_d$ of the miter gate on the downstream side, the probability of failure given in Eq. (4.7) is rewritten as

$$p_f(\mathbf{d}) = \begin{cases} \Pr\{P_a(F(A,\, \mathbf{V},\, \mathbf{d}),\, \theta_{ud}) < T_e\}, \text{ if } V_l > d_y \\ \Pr\{P_a(F(A,\, \mathbf{V},\, \mathbf{d}),\, \theta_{ab}) < T_e\}, \text{ if } V_l \leq d_y \end{cases}. \tag{4.8}$$

The above equation can be further written as

$$\begin{aligned} p_f(\mathbf{d}) = &\Pr\{T_c(\mathbf{d}) = P_a(F(A,\, \mathbf{V},\, \mathbf{d}),\, \theta) \leq T_e | V_l > d_y\} \Pr\{V_l > d_y\} \\ &+ \Pr\{T_c(\mathbf{d}) = P_a(F(A,\, \mathbf{V},\, \mathbf{d}),\, \theta) \leq T_e | V_l \leq d_y\} \Pr\{V_l \leq d_y\}. \end{aligned} \tag{4.9}$$

The probability of failure for locations on the upstream side can be defined similarly to the above equations. Directly solving the probability of failure given in Eq. (4.9) is computationally challenging due to the integration given in Eq. (4.7) and the computationally expensive PF simulation model $P_a(\cdot)$. More specifically, due to the coupled partial differential equations, each simulation of the PF model takes more than 40 minutes on an Intel Xeon W-2155 workstation with a 3.30 GHz CPU, 10 cores / 20 threads, and 256 GB RAM. It would require years to solve Eq. (4.9) if the high-fidelity PF simulation model is employed directly. Moreover, the physics-based PF simulation is at the mesoscale (i.e., millimeters or smaller) while the miter gate structure is at the macroscale (i.e., meters), reliability analysis of the whole miter gate requires the evaluation of Eq. (4.9) thousands of times. This adds an additional layer of challenge to the corrosion reliability analysis of miter gates.

In order to tackle this computational barrier and make it possible to perform physics-based corrosion reliability analysis of large structures using localized mesoscale simulations, we propose a novel adaptive surrogate modeling framework in the next section by considering various uncertainty resources in macroscale and mesoscale simulations simultaneously through surrogate models. In what follows, the proposed method is explained in detail.

4.4 Proposed Method for Physics-Based Corrosion Reliability Analysis of Miter Gates

4.4.1 Overview of the proposed method

Fig. 4.7 shows an overview of the workflow for corrosion reliability analysis of miter gates. As illustrated in this figure, the overall analysis consists of two parts. One is the global

simulation of the macroscale miter gate. The other one is the local simulation for the mesoscale corrosion simulation. They are connected by mechanical stress which is the output of the miter gate model and the input of the corrosion model.

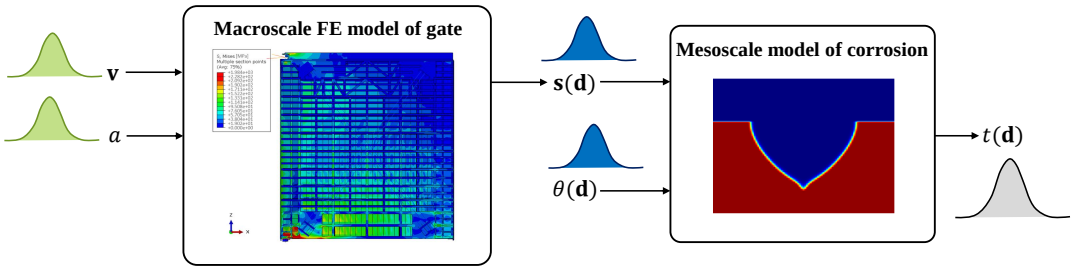

Figure 4.7. The schematic representation of proposed method

In order to overcome the computational challenges mentioned in Sec. 4.3.3, we employ a surrogate modeling-based reliability analysis method. One way of constructing surrogate modeling is to treat the overall simulation as illustrated in Fig. 4.7 as a black-box model with $\mathbf{v}$, a, and θ as inputs and $T_c(\mathbf{d})$ as the output (see the mathematical model given in Eq. (4.9)). This approach, however, is applicable only if we are interested in the SCC initiation time at a particular location. It could be computationally expensive if the corrosion reliability of all the locations on the gate needs to be analyzed. To address this issue, we construct two different surrogate models by separating the analyses and uncertainty sources at two different length scales (i.e., macroscale and mesoscale) according to the analysis flow given in Fig. 4.7. More specifically, the following two types of surrogate models are constructed:

- **Global surrogate model for the macroscale structural analysis**: a global surrogate model is constructed for the structural analysis at the macroscale. The uncertainty sources from the hydraulic water head $\mathbf{v}$ and the gap length a are propagated to the stress response at any location of the miter gate through the global surrogate model.

- **Local surrogate model for mesoscale reliability analysis**: a local surrogate model is developed to replace the mesoscale PF analysis model. For any given stress condition, the

local surrogate model predicts the localized corrosion reliability analysis by considering the uncertainty sources in the model parameters of the PF simulation model.

The differences between the global surrogate model and the local surrogate model are: (1) the global surrogate model is accurate in the whole analysis domain of interest so that the surrogate model can accurately predict the stress response of the full miter gate for any given water level conditions and gap length; and (2) the local surrogate model is only accurate in certain regions (e.g., near the limit state) that are important for reliability analysis, since we usually are only concerned about the accuracy of the limit-state function in reliability analysis [105]. The local surrogate model enables us to significantly reduce the required effort in training the surrogate model without sacrificing the accuracy of reliability analysis. After the training of the two types of surrogate models, they are integrated together through mechanical stress to enable efficient corrosion reliability analysis for any location on the miter gate. To construct these two types of surrogate models, we first rewrite the probability of failure given in Eq. (4.9) as follows

$$\begin{aligned} p_f(\mathbf{s}|\text{Under water}) &= \Pr\{P_a(\mathbf{s},\ \theta_{ud}) \leq T_e\}, \\ p_f(\mathbf{s}|\text{Above water}) &= \Pr\{P_a(\mathbf{s},\ \theta_{ab}) \leq T_e\}, \end{aligned} \tag{4.10}$$

where $p_f(\mathbf{s}|\text{Under water})$ and $p_f(\mathbf{s}|\text{Above water})$ are respectively the probability of failure for the under-water and above-water scenarios for a given stress condition $\mathbf{s}$.

The probability of failure $p_f(\mathbf{d})$ for a given location $\mathbf{d} \in \Omega_d$ on the downstream side is then given by

$$\begin{aligned} p_f(\mathbf{d}) = \Pr\{V_l \leq d_y\} \int\int p_f(\mathbf{s}(a,\ \mathbf{v},\ \mathbf{d})|\text{Above water}) f_A(a) f_{V|\text{Ab}}(\mathbf{v}|\text{Ab}) da\mathbf{dv} \\ + \Pr\{V_l > d_y\} \int\int p_f(\mathbf{s}(a,\ \mathbf{v},\ \mathbf{d})|\text{Under water}) f_A(a) f_{V|\text{Ud}}(\mathbf{v}|\text{Ud}) da\mathbf{dv}, \end{aligned} \tag{4.11}$$

in which $\mathbf{s}(a,\ \mathbf{v},\ \mathbf{d})$ is the stress vector at location $\mathbf{d}$ for given gap length a and water levels $\mathbf{v}$, $f_{V|\text{Ab}}(\mathbf{v}|\text{Ab})$ and $f_{V|\text{Ud}}(\mathbf{v}|\text{Ud})$ are respectively the PDFs of the water levels on the gate given that

the location of interest d_y is above-water or under-water.

The probability of failure for locations on the upstream side can be analyzed similarly using Eqs. (4.10) and (4.11). In Eq. (4.11),

- $\mathbf{s}(a,\ \mathbf{v},\ \mathbf{d})$ is predicted using the global surrogate model (see Sec. 4.4.2),
- and $p_f(\mathbf{s}(a,\ \mathbf{v},\ \mathbf{d})|\text{Above water})$ and $p_f(\mathbf{s}(a,\ \mathbf{v},\ \mathbf{d})|\text{Under water})$ (i.e., Eq. (4.10)) are estimated using the local surrogate model based on the predicted stress response from the global surrogate (see Sec. 4.4.3).

In the subsequent sections, we will explain how the surrogate models are constructed for the macroscale structural analysis and for reliability analysis using the mesoscale PF simulation model.

4.4.2 Surrogate modeling of macroscale structural analysis model

For given gap length a and hydra-static load $\mathbf{v}$, we define the stress response of the miter gate as $\mathbf{s}(\mathbf{w}) = [\mathbf{s}_{(1)}(\mathbf{w}), \mathbf{s}_{(2)}(\mathbf{w}), ..., \mathbf{s}_{(N_d)}(\mathbf{w})]^T = [F(a,\mathbf{v},\mathbf{d}_1), F(a,\mathbf{v},\mathbf{d}_2), ..., F(a,\mathbf{v},\mathbf{d}_{N_d})]^T \in \mathbb{R}_{N_d\times 3}$, where $\mathbf{w} = [a,\mathbf{v}]$ are the inputs of the macroscale structural analysis model, $\mathbf{d}_i \in \Omega_d$ is the i-th spatial location, $\mathbf{s}_{(i)}(\mathbf{w}) = [s_{(i,x)}(\mathbf{w}),\ s_{(i,y)}(\mathbf{w}),\ s_{(i,z)}(\mathbf{w})]^T \in \mathbb{R}_{3\times 1},\ i = 1, \cdots,\ N_d$, are the three-component stress responses at the i-th spatial location, and N_d is the total number of spatial locations on the gate or the number of locations in set Ω_d. In order to construct a surrogate model for the macroscale model, we first generate N training samples for the inputs using the Sobol sampling technique and denote the training samples as $\mathbf{w}_t = [\mathbf{w}_1, \mathbf{w}_2, ..., \mathbf{w}_N]$. Using the N training samples as inputs to the physics-based simulations and taking the stress response in the x-direction as an example, we have a data matrix as

$$\mathbf{s}_{t,x} = [\mathbf{s}_x(\mathbf{w}_1), \mathbf{s}_x(\mathbf{w}_2), ..., \mathbf{s}_x(\mathbf{w}_N)] \in \mathbb{R}_{N_d\times N}, \tag{4.12}$$

where $\mathbf{s}_x(\mathbf{w}_k) = [s_{(1,x)}(\mathbf{w}_k),\ s_{(2,x)}(\mathbf{w}_k),\ \cdots,\ s_{(N_d,x)}(\mathbf{w}_k)]^T \in \mathbb{R}_{N_d \times 1},\ k = 1, \cdots, N$, are the stress responses in the x direction for input sample $\mathbf{w}_k$.

The data matrix $\mathbf{s}_{t,x}$ is computationally burdensome for surrogate modeling when N_d and N are large. Based on the fact that the stress responses for the adjacent elements are often similar to each other, dimension reduction techniques such as auto-encoding, principal component analysis, or singular value decomposition (SVD), may be employed to map the high-dimensional stress response to low-dimensional latent response [150, 149]. In this work, $\mathbf{s}_{t,x}$ is decomposed with SVD as [150] Γ

$$\mathbf{s}_{t,x} = \mathbf{W}\Gamma\mathbf{Z}^T, \tag{4.13}$$

where $\mathbf{W}$ is a $N_d \times N_d$ orthogonal matrix, $\mathbf{Z}$ is a $N \times N$ orthogonal matrix, and Γ is a $N_d \times N$ diagonal matrix with decreasing diagonal elements $= [\eta_1, \eta_2, ..., \eta_r]$, with $r = \min(N_d, N)$. The first N_c terms in are selected to maintain 98% of the total variance.

Based on the decomposition using SVD and define $= \mathbf{W}\Gamma$, we can then reconstruct $\mathbf{s}_x(\mathbf{w}_k), \forall k = 1 \cdots N$, as

$$\mathbf{s}_x(\mathbf{w}_k) \approx \sum_{j=1}^{N_c} \gamma_{kj}\mathbf{Z}_{x,j} \in \mathbb{R}_{N_d \times 1}, \forall k = 1 \cdots N, \tag{4.14}$$

where $\gamma_{kj}, \forall j = 1, ..., N_c$ are the latent responses corresponds to $\mathbf{s}_x(\mathbf{w}_k)$, and $\mathbf{Z}_{x,j}, \forall j = 1, ..., N_c$ are the basis functions. They are obtained based on the eigenvalues and eigenvectors given in Eq. (4.13). More details about the decomposition are available in Ref. [149, 150].

After mapping the stress response into latent responses, in this work, we use the Gaussian process regression (GPR) model to build the surrogate models that connect inputs $\mathbf{w} = [a, \mathbf{v}]$ with the latent responses, and then map the latent responses to response of the macroscale structural analysis model using Eq. (4.14). Such a global surrogate modeling strategy has also been employed in the literature and more details can be found in Refs. [61, 68, 74]. After surrogate

modeling, the stress response in the x-direction for any new input $\mathbf{w} = [a, \mathbf{v}]$ can be predicted as

$$\hat{\mathbf{s}}_x(\mathbf{w}) = [\hat{s}_{(1,x)}(\mathbf{w}),\ \hat{s}_{(2,x)}(\mathbf{w}), \cdots,\ \hat{s}_{(N_d,x)}(\mathbf{w})] = \sum_{j=1}^{N_c} \hat{g}_{x,j}(a, \mathbf{v})\mathbf{Z}_{x,j} + \varepsilon_x, \tag{4.15}$$

where $\hat{\mathbf{s}}_x(\mathbf{w})$ is the predicted stress response for the set of locations in Ω_d, $\hat{\gamma}_j = \hat{g}_{x,j}(a, \mathbf{v})$ is the GPR surrogate model prediction of the j-th latent response, and ε_x is the residual error of the prediction.

The surrogate models of stress responses in the other two directions (i.e., y and z directions) can be constructed similarly. In addition, it worth noting that the above surrogate modeling method can only predict the stress responses for the fixed locations $\mathbf{d} \in \Omega_d$. If we want to predict the stress response for locations that does not belong to Ω_d, a certain interpolation or approximation needs to be performed. After the training of the global surrogate model for the macroscale structural analysis model, the prediction accuracy of the model is verified using validation data. If the accuracy cannot satisfy the requirement, more training data are added and the above process is repeated to retrain the model. Next, we will discuss how to train a local surrogate model for reliability analysis at the mesoscale level.

4.4.3 Adaptive surrogate modeling for corrosion reliability analysis at mesoscale

The goal of the local surrogate modeling is to efficiently predict $p_f(\mathbf{s}|\text{Under water})$ and $p_f(\mathbf{s}|\text{Above water})$ for any given stress $\mathbf{s}$ (see Eq. (4.10)). Even though $p_f(\mathbf{s}|\text{Under water})$ is used as an example in this section to explain the proposed adaptive surrogate modeling method, the method is also applied to compute $p_f(\mathbf{s}|\text{Above water})$.

Motivated by overcoming the computational challenges in reliability analysis, various adaptive surrogate modeling methods have been proposed in the past [43, 69, 16, 154, 13]. This type of method is also called "active learning" in recent years in the literature. The basic idea of adaptive surrogate modeling is to add the most informative training points for surrogate

modeling over iterations with the goal to reduce the required number of training points without sacrificing accuracy. Since surrogate models can be used for different purposes, such as reliability analysis, Bayesian calibration, and optimization, the strategy of adaptive surrogate modeling will change with the ultimate goal of the surrogate modeling. For reliability analysis, we are mainly concerned about the accuracy of the limit state. Adaptive surrogate modeling for reliability analysis therefore usually adds more training points in local regions that are close to the limit state. In order to compute $p_f(\mathbf{s}|\text{Under water})$, we construct a GPR surrogate model for the following limit state function

$$T(\mathbf{s}, \theta_{ud}) = P_a(\mathbf{s}, \theta_{ud}) - T_e, \tag{4.16}$$

where $P_a(\mathbf{s}, \theta_{ud})$ is the PF simulation model given in Eq. (4.6).

To facilitate the construction of the GPR surrogate model using the adaptive surrogate modeling method, we first transform θ_{ud} into standard normal random variables as $u_i = \Phi^{-1}(F_{\theta,i}(\theta_{ud,i})), \forall i = 1, \cdots, N_\theta$, where N_θ is the number of random variables in the SCC model, $F_{\theta,i}(\theta_{ud,i})$ is the cumulative density function (CDF) of the i-th random variable, and $\Phi^{-1}(\cdot)$ is the inverse CDF function of a standard normal random variable. Based on this transformation, we can rewrite Eq. (4.16) as

$$G(\mathbf{s}, \mathbf{u}) = P_a(\mathbf{s}, F_\theta^{-1}(\Phi(\mathbf{u}))) - T_e. \tag{4.17}$$

in which $F_\theta^{-1}(\cdot)$ stands for the inverse CDF function of θ_{ud}.

$p_f(\mathbf{s}|\text{Under water})$ can be computed based on Eq. (4.17) as

$$p_f(\mathbf{s}|\text{Under Water}) = \Pr\{G(\mathbf{s},\ \mathbf{u}) \leq 0\} = \Pr\{P_a(\mathbf{s},\ F_\theta^{-1}(\Phi(\mathbf{u}))) - T_e) \leq 0\}. \tag{4.18}$$

In the proposed adaptive surrogate modeling method for reliability analysis at mesoscale, we start with a set of training points $\alpha_t = [\mathbf{s}_t, \mathbf{u}_t]$ and corresponding response $\mathbf{y}_t$ of the limit-state

function, where $\mathbf{y}_t = G(\mathbf{s}_t, \mathbf{u}_t)$. Based on training points α_t and $\mathbf{y}_t$, a GPR surrogate model is constructed as $\Im \overset{\Delta}{=} \hat{G}(\mathbf{s}, \mathbf{U}|\alpha_t, \mathbf{y}_t) \sim \mathcal{N}(\mu_{\hat{G}}(\mathbf{s}, \mathbf{U}), \sigma^2_{\hat{G}}(\mathbf{s}, \mathbf{U}))$. Using the surrogate model $\Im$, Eq. (4.18) can be approximated using Monte-Carlo simulation as

$$\begin{aligned} p_f(\mathbf{s}|\text{Under Water}; \Im) &= \int_{\Omega_{\mathbf{u}}} I(\mu_{\hat{G}}(\mathbf{s},\, \mathbf{u})) f_{\mathbf{u}}(\mathbf{u}) \mathbf{du}, \\ &\approx \frac{1}{N_{MCS}} \sum_{i=1}^{N_{MCS}} I(\mu_{\hat{G}}(\mathbf{s},\, \mathbf{u}^{(i)})), \end{aligned} \tag{4.19}$$

where $\Omega_{\mathbf{u}}$ is the domain of $\mathbf{u}$, $I(\mu_{\hat{G}}(\mathbf{s},\, \mathbf{u}))$ is an indicator function with $I(\mu_{\hat{G}}(\mathbf{s},\, \mathbf{u})) = 1$, if $\mu_{\hat{G}}(\mathbf{s},\, \mathbf{u}) \leq 0$; $I(\mu_{\hat{G}}(\mathbf{s},\, \mathbf{u})) = 0$, otherwise, $f_{\mathbf{u}}(\mathbf{u})$ is the joint PDF of random variables $\mathbf{u}$, and $\mathbf{u}^{(i)}$, $i = 1, \cdots, N_{MCS}$ are the MCS samples.

Due to the surrogate modeling uncertainty of $\Im$, Eq. (4.19) could give an estimation of $p_f(\mathbf{s}|\text{Under water})$ with a very large error. The accuracy of Eq. (4.19) can be improved by refining $\Im$ in critical regions. One way of doing that is to employ the adaptive Kriging Monte Carlo simulation (AK-MCS) method [43, 16], which adaptively identifies new training points for refining the surrogate model using the learning function

$$\Lambda(\mathbf{u}) = \frac{\left|\mu_{\hat{G}}(\mathbf{s}, \mathbf{u})\right|}{\sigma_{\hat{G}}(\mathbf{s}, \mathbf{u})}, \tag{4.20}$$

where $\mu_{\hat{G}}(\mathbf{s}, \mathbf{u})$ and $\sigma_{\hat{G}}(\mathbf{s}, \mathbf{u})$ are respectively the mean and standard deviation of the surrogate model prediction as mentioned above for given $\mathbf{u}$.

While results of past applications have shown that AK-MCS can drastically reduce the required number of training points for surrogate-based reliability analysis, its performance can be further improved. In this chapter, we propose a new adaptive surrogate modeling method for mesoscale simulation by making the following two contributions:

- Integrating adaptive importance sampling (IS) method with the Gaussian mixture model (GMM) and adaptive surrogate modeling. It is inspired by the Meta-IS method presented

in [41] and is more robust than the original Meta-IS method for the studied problem in this work. In the proposed method, the GMM model is used in conjunction with surrogate model to inform IS, while IS is used in turn to guide the refinement of the surrogate model.

- Defining convergence criterion for the proposed adaptive surrogate modeling method based on IS and GMM directly from reliability analysis perspective by analyzing the maximum reliability estimation error.

In what follows, we explain these two main components of the proposed adaptive surrogate modeling method in details.

Adaptive surrogate modeling at mesoscale based on IS and GMM

In IS, the expectation of the indicator function given in Eq. (4.19) is computed based on a different statistical distribution which favors the failure boundary, instead of the original standard normal distribution [53]. An essential element of the IS method is an instrumental density $h(\mathbf{u})$, which is assumed to dominate $I(\mu_{\hat{G}}(\mathbf{s},\,\mathbf{u}))f_{\mathbf{u}}(\mathbf{u})$. For any given instrumental density function $h(\mathbf{u})$, the probability of failure defined in Eq. (4.19) may be rewritten as follows

$$\begin{aligned} p_f(\mathbf{s}|\text{Under Water};\Im) &= \int_{\Omega_{\mathbf{U}}} I(\mu_{\hat{G}}(\mathbf{s},\mathbf{u}))\frac{f_{\mathbf{u}}(\mathbf{u})}{h(\mathbf{u})}h(\mathbf{u})\mathbf{du} \\ &\approx \frac{1}{N_{IS}}\sum_{i=1}^{N_{IS}} I(\mu_{\hat{G}}(\mathbf{s},\mathbf{u}_{IS}^{(i)}))\frac{f_{\mathbf{u}}(\mathbf{u}_{IS}^{(i)})}{h(\mathbf{u}_{IS}^{(i)})}, \end{aligned} \tag{4.21}$$

where $\mathbf{u}_{IS}^{(i)},\ i=1,\cdots,N_{IS}$ are the importance samples generated from the instrumental density $h(\mathbf{u})$.

The instrumental density function $h(\mathbf{u})$ could affect the accuracy of reliability analysis. The optimal instrumental density can be obtained when the variance of the IS estimator is zero. In theory, the optimal instrumental density is given by

$$h^*(\mathbf{u}) = \frac{I(G(\mathbf{s},\mathbf{u}))f_{\mathbf{u}}(\mathbf{u})}{\int I(G(\mathbf{s},\mathbf{u}))f_{\mathbf{u}}(\mathbf{u})\mathbf{du}}. \tag{4.22}$$

However, the integration in the denominator representing the probability of failure is hard to know in practice, which makes it challenging to identify the optimal instrumental density function. To tackle this issue, the surrogate model-based optimal instrumental density proposed by [41] is employed. Using the surrogate model $\Im$, the approximate optimal instrumental density function is given by

$$\hat{h}^*(\mathbf{u}|\Im) = \frac{\varphi(\mathbf{u}|\Im) f_{\mathbf{u}}(\mathbf{u})}{\int \varphi(\mathbf{u}|\Im) f_{\mathbf{u}}(\mathbf{u}) \mathbf{du}} \propto \varphi(\mathbf{u}|\Im) f_{\mathbf{u}}(\mathbf{u}), \tag{4.23}$$

where $\varphi(\mathbf{u}|\Im)$ is a probabilistic classification function defined as

$$\varphi(\mathbf{u}|\Im) = \Phi\left(\frac{0 - \mu_{\hat{G}}(\mathbf{s},\mathbf{u})}{\sigma_{\hat{G}}(\mathbf{s},\mathbf{u})}\right), \tag{4.24}$$

in which $\Phi(\cdot)$ is the CDF of a standard normal distribution.

As shown in Eq. (4.23), the problem of identifying the optimal instrumental density function becomes to be a Bayesian inference problem. Assume that N_{MCS} number of MCS samples are generated for random variables $\mathbf{u}$, we then compute the probabilistic classification probabilities for these samples using Eq. (4.24) as $\varphi(\mathbf{u}^{(i)}|\Im), \forall i = 1, \cdots, N_{MCS}$. Based on the computed likelihood functions, in this work, we solve Eq. (4.24) using the particle filtering method. We first compute the weight of each particle as

$$w(\mathbf{u}^{(i)}|\Im) = \frac{\varphi(\mathbf{u}^{(i)}|\Im)}{\sum_{j=1}^{N_{IS}} \varphi(\mathbf{u}^{(j)}|\Im)} = \frac{\Phi\left(\frac{-\mu_{\hat{G}}(\mathbf{s}^{(i)},\mathbf{u}^{(i)})}{\sigma_{\hat{G}}(\mathbf{s}^{(i)},\mathbf{u}^{(i)})}\right)}{\sum_{j=1}^{N_{IS}} \Phi\left(\frac{-\mu_{\hat{G}}(\mathbf{s}^{(j)},\mathbf{u}^{(j)})}{\sigma_{\hat{G}}(\mathbf{s}^{(j)},\mathbf{u}^{(j)})}\right)}. \tag{4.25}$$

After that, we obtain the posterior samples using the re-sampling method according to the weights as follows

$$p(\mathbf{u}^{(i)}|\Im) = \sum_{i=1}^{N_{IS}} w(\mathbf{u}^{(i)}|\Im)\delta(\mathbf{u}^{(i)}), \tag{4.26}$$

where $\Im$ represents current surrogate model as mentioned above and $\delta(\cdot)$ is a delta function.

Since the PDF of the instrumental density function is needed for the calculation of the probability of failure based on IS, we then approximate $h(\mathbf{u})$ as a GMM based on the posterior samples as

$$\hat{h}^*(\mathbf{u}|\Im) \approx \sum_{k=1}^{Q} \lambda_k \phi(\mathbf{u},\, \mu_k,\, \mathbf{\Sigma}_k), \tag{4.27}$$

where Q is the number of Gaussian components, μ_k is the mean value vector of the i-th Gaussian component, and $\mathbf{\Sigma}_k$ is the covariance of the i-th Gaussian component, $\phi(\cdot)$ is the probability density function of a standard normal random variable.

Once we have the GMM model, it is used to generate the importance samples denoted as $\mathbf{u}_{IS}^{(i)},\ i = 1,\ \cdots,\ N_{IS}$, where N_{IS} is the number of importance samples. Using the importance samples and the surrogate model $\Im$, Eq. (4.21) is computed by

$$p_f(\mathbf{s}|\text{Under Water};\Im) \approx \frac{1}{N_{IS}} \sum_{i=0}^{N_{IS}} I(\mu_{\hat{G}}(\mathbf{s},\mathbf{u}_{IS}^{(i)})) \frac{f_{\mathbf{u}}(\mathbf{u}_{IS}^{(i)})}{\sum_{k=1}^{Q} \lambda_k \phi(\mathbf{u}_{IS}^{(i)}, \mu_k, \mathbf{\Sigma}_k)}. \tag{4.28}$$

Due to the prediction uncertainty of $\Im$, Eq. (4.28) may not estimate the failure probability accurately. In order to check the accuracy of the prediction, in the next subsection, we further propose a convergence criterion directly from reliability analysis perspective to determine when and at what input to refine the surrogate model.

Convergence criterion and reliability estimation error analysis

We first partition the importance samples into two groups using Eq. (4.20). More specifically, we first compute $\Lambda(\mathbf{u}_{IS}^{(i)}), \forall i = 1,\ \cdots,\ N_{IS}$. Since $\Lambda(\mathbf{u}_{IS}^{(i)})$ measures the distance between the mean prediction and the limit state divided by the standard deviation of the prediction, it quantifies how confident the prediction is about the sign of the limit state function. A small value of $\Lambda(\mathbf{u}_{IS}^{(i)})$ means that the prediction of a sample $\mathbf{u}_{IS}^{(i)}$ is more likely to cause an error in the reliability prediction. Based on this, we have the first group of samples $\mathbf{u}_{G1} \triangleq \{\mathbf{u}_{IS}^{(i)} | \Lambda(\mathbf{u}_{IS}^{(i)}) > 2,\ \forall i = 1, \cdots, N_{IS}\}$ contains the samples with $\Lambda(\mathbf{u}_{IS}^{(i)})$ values greater than 2, while the other group

$\mathbf{u}_{G2} \triangleq \{\mathbf{u}_{IS}^{(i)} | \Lambda(\mathbf{u}_{IS}^{(i)}) \leq 2,\ \forall i = 1, \cdots, N_{IS}\}$ contains the remaining importance samples [42, 69]. Based on this partition, we have the failure probability given in Eq. (4.28) as

$$\hat{p}_f(\mathbf{s}|\text{Under Water}; \Im) = \frac{\overbrace{\sum_{i=1}^{N_{G1}} I(\mu_{\hat{G}}(\mathbf{s},\, \mathbf{u}_{G1}^{(i)}))\chi(\mathbf{u}_{G1}^{(i)})}^{\text{Group 1}} + \overbrace{\sum_{j=1}^{N_{G2}} I(\mu_{\hat{G}}(\mathbf{s},\, \mathbf{u}_{G2}^{(j)}))\chi(\mathbf{u}_{G2}^{(j)})}^{\text{Group 2}}}{N_{IS}}, \tag{4.29}$$

where $\chi(\mathbf{u}) = \frac{f_U(\mathbf{u})}{\sum_{k=1}^{Q} \lambda_k \phi(\mathbf{u}, \mu_k, \blacksquare_k)}$ is the sample weight in IS, N_{G1} and N_{G2} are respectively the number of importance samples in group 1 and group 2.

For the sake of explanation, we further define

$$\hat{N}_{f1} = \sum_{i=1}^{N_{G1}} I(\mu_{\hat{G}}(\mathbf{s},\, \mathbf{u}_{G1}^{(i)}))\chi(\mathbf{u}_{G1}^{(i)});\ \hat{N}_{f2} = \sum_{j=1}^{N_{G2}} I(\mu_{\hat{G}}(\mathbf{s},\, \mathbf{u}_{G2}^{(j)}))\chi(\mathbf{u}_{G2}^{(j)}). \tag{4.30}$$

Based on the above definition and if $N_{G2} > 0$, the error of the probability of failure estimation can be computed as $\hat{N}_{f1}$

$$\xi = \frac{\left| \hat{N}_{f2} - \sum_{j=1}^{N_{G2}} I(\hat{G}(\mathbf{s},\, \mathbf{u}_{G2}^{(j)}|\alpha_t, \mathbf{y}_t))\chi(\mathbf{u}_{G2}^{(j)}) \right|}{\hat{N}_{f1} + \sum_{j=1}^{N_{G2}} I(\hat{G}(\mathbf{s},\, \mathbf{u}_{G2}^{(j)}|\alpha_t, \mathbf{y}_t))\chi(\mathbf{u}_{G2}^{(j)})} \times 100\%, \tag{4.31}$$

where $\hat{G}(\mathbf{s},\, \mathbf{u}_{G2}^{(j)}|\alpha_t, \mathbf{y}_t)$ stands for the prediction from surrogate model $\Im$ as Eq. (4.17) shows.

For $\sum_{j=1}^{N_{G2}} I(\hat{G}_T(\mathbf{s},\, \mathbf{u}_{G2}^{(j)}|\alpha_t, \mathbf{y}_t))\chi(\mathbf{u}_{G2}^{(j)})$, it is bounded by

$$0 \leq \sum_{j=1}^{N_{G2}} I(\hat{G}_T(\mathbf{s}, \mathbf{u}_{G2}^{(j)}|\alpha_t, \mathbf{y}_t))\chi(\mathbf{u}_{G2}^{(j)}) \leq \sum_{j=1}^{N_{G2}} \chi(\mathbf{u}_{G2}^{(j)}). \tag{4.32}$$

We, therefore, have a conservative estimate of the maximum error of failure probability

estimation as

$$\xi_{\max} = \max_{N_u \in [0,\ \sum_{j=1}^{N_{G2}} \chi(\mathbf{u}_{G2}^{(j)})]} \left\{ \frac{\left|\hat{N}_{f2} - N_u\right|}{\hat{N}_{f1} + N_u} \right\} \times 100\%, \text{ if } N_{G2} > 0. \tag{4.33}$$

The algorithm stops when the maximum error defined in Eq. (4.33) is less than the requirement (i.e., 5% in this work). If the maximum error requirement is not satisfied, a new training point $\mathbf{u}_{new}$ is identified as

$$\mathbf{u}_{new} = \underset{\mathbf{u} \in \mathbf{u}_{IS}^{(i)},\ i=1,\cdots,N_{IS}}{\arg\min} \left\{ \Lambda(\mathbf{u}) \right\}. \tag{4.34}$$

Together with the fixed values of $\mathbf{s}$ as the input, a new training sample of the inputs is obtained as $\alpha_{new} = [\mathbf{s},\ \mathbf{u}_{new}]$. The corresponding response is obtained as $y_{new} = G(\mathbf{s}, \mathbf{u}_{new})$. After that the training dataset is updated as $\alpha_t = [\alpha_t; \alpha_{new}], \mathbf{y}_t = [\mathbf{y}_t; y_{new}]$. With the updated training dataset, the surrogate model $\Im$ is updated. The above process from Eqs. (4.16) through (4.34) is repeated until the accuracy requirement of the maximum error is satisfied. Once the accuracy requirement is satisfied, we obtain the estimate of $p_f(\mathbf{s}|\text{Under water})$ using Eq. (4.28).

Fig. 4.8 summarizes the overall procedure of computing the probability of failure for given stress s using the proposed adaptive surrogate modeling method.

Note that even though the proposed method is explained using $p_f(\mathbf{s}|\text{Under water})$, it is also applied to estimate $p_f(\mathbf{s}|\text{Above water})$. Next, we discuss how to integrate the global surrogate model at the macroscale with the adaptive surrogate model at the mesoscale for pitting corrosion reliability analysis of miter gates at any spatial location using the macroscale structural analysis and mesoscale PF-based pitting corrosion simulation.

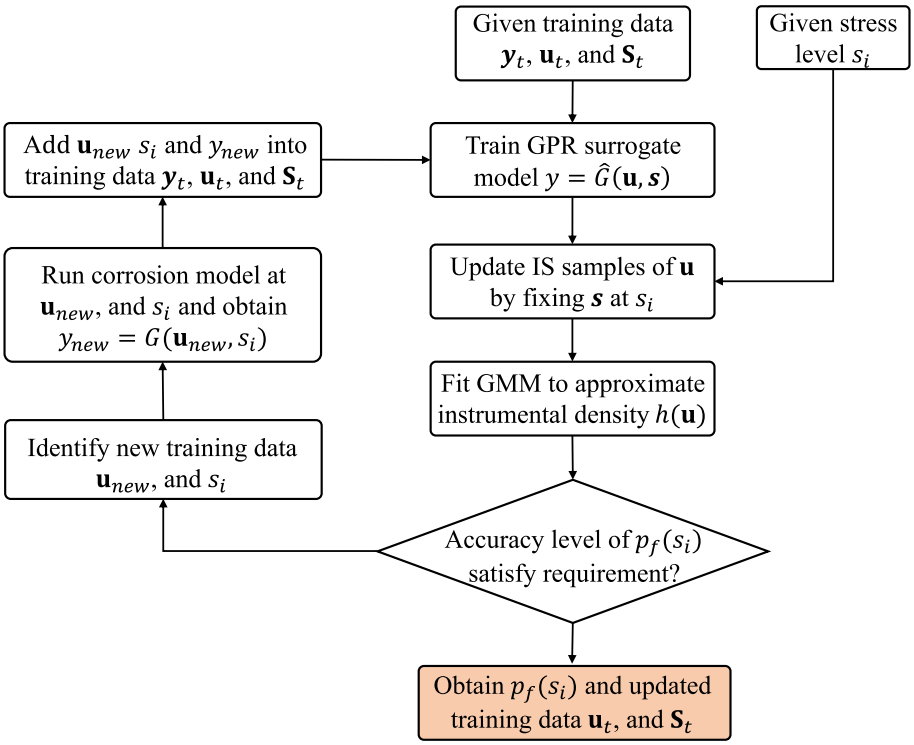

Figure 4.8. Algorithm 1: compute $p_f(s_i)$ for any given stress level s_i

4.4.4 Integration of the macroscale global surrogate model and mesoscale local surrogate model for corrosion reliability analysis

The multi-scale surrogate models are established to capture the uncertainties from different length scales such as gap length a and the hydraulic water heads $\mathbf{v}$ at the macroscale and the electrochemical parameters θ at the mesoscale. Even though the adaptive surrogate modeling method presented in Sec. 4.4.3 drastically reduces the required computational effort to estimate the failure probability given any stress $\mathbf{s}$, it is still computationally very challenging to directly use it for pitting corrosion reliability analysis of the whole miter gate. The challenge stems from the fact that there are thousands of spatial locations on the gate (N_d given in Sec. 4.4.2 is a very large number) and the stress response could have thousands of possible realizations for any given location $\mathbf{d} \in \Omega_d$ due to uncertainty in a and $\mathbf{v}$.

To address this challenge in the integration, we first generate N_s samples for the stress

level using the Sobol sampling technique as illustrated in Fig. 4.9. For each stress sample $\mathbf{s}^{(i)}, i = 1, \cdots, N_s$, the adaptive surrogate modeling method developed in Sec. 4.4.3 is implemented to estimate $p_f(\mathbf{s}^{(i)}|\text{Under water}), \forall i = 1, \cdots, N_s$ and $p_f(\mathbf{s}^{(i)}|\text{Above water}), \forall i = 1, \cdots, N_s$. Note that a common training dataset $\alpha_t, \mathbf{y}_t$ is updated as illustrated in Fig. 4.9 during the process to reuse the data across different stress levels. After that, surrogate models $\hat{p}_{f,ud}(\mathbf{s}) = G_{ud}(\mathbf{s})$ and $\hat{p}_{f,ab}(\mathbf{s}) = G_{ab}(\mathbf{s})$ are constructed respectively for the under-water and above-water scenarios of the failure probability as a function of stress $\mathbf{s}$. With these two surrogate models, we then efficiently predict the pitting corrosion reliability for any location on the gate. To do that, we first generate MCS samples of $\mathbf{v}$ and a as $\{a^{(k)}, \mathbf{v}^{(k)};\ \forall k = 1, \cdots, N_M\}$. We then obtain the samples of stress response for any given location $\mathbf{d}_i \in \Omega_d, i = 1, \cdots, N_d$ using surrogate model constructed in Sec. 4.4.2 as

$$\begin{aligned}
\hat{s}_{(i,x)}(\mathbf{w}^{(k)}) &= \sum_{j=1}^{N_c} \hat{g}_{x,j}(a^{(k)}, \mathbf{v}^{(k)}) \mathbf{Z}_{x,j}(\mathbf{d}_i) + \varepsilon_{x,i}, \forall i = 1, \cdots, N_d;\ k = 1, \cdots, N_M, \\
\hat{s}_{(i,y)}(\mathbf{w}^{(k)}) &= \sum_{j=1}^{N_c} \hat{g}_{y,j}(a^{(k)}, \mathbf{v}^{(k)}) \mathbf{Z}_{y,j}(\mathbf{d}_i) + \varepsilon_{y,i}, \forall i = 1, \cdots, N_d;\ k = 1, \cdots, N_M,
\end{aligned} \tag{4.35}$$

where $\mathbf{w}^{(k)} = [a^{(k)}, \mathbf{v}^{(k)}]$.

The failure probability at location $\mathbf{d}_i \in \Omega_d, i = 1, \cdots, N_d$ is then computed as

$$p_f(\mathbf{d}_i) = \frac{1}{N_M} \sum_{k=1}^{N_M} \hat{p}_{f,w}(\mathbf{s}(\mathbf{d}_i,\ k)), \forall i = 1, \cdots, N_d \tag{4.36}$$

where $\hat{p}_{f,w}(\mathbf{s}(\mathbf{d}_i,\ k))$ is given by

$$\hat{p}_{f,w}(\mathbf{s}(\mathbf{d}_i,\ k)) = \begin{cases} \hat{p}_{f,ud}(\mathbf{s}(\mathbf{d}_i,\ k)), \text{if } v_l^{(k)} > d_y \\ \hat{p}_{f,ab}(\mathbf{s}(\mathbf{d}_i,\ k)),\ \text{if } v_l^{(k)} \leq d_y \end{cases}. \tag{4.37}$$

With Eqs. (4.35) through (4.37), the macroscale global surrogate model and mesoscale local surrogate model are integrated into the proposed algorithm and the uncertainties from

different scales are taken into consideration. This allows us to efficiently predict the failure probability of pitting corrosion for any location on the gate. Fig. 4.9 summarizes the overall implementation procedure for the integration of these two types of surrogate models for reliability analysis.

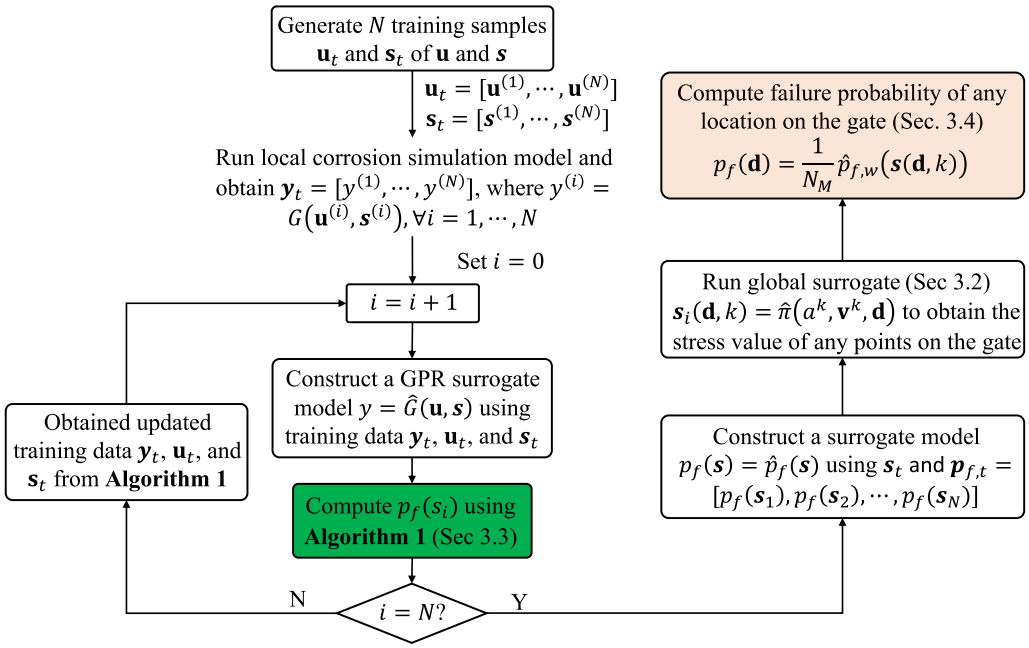

Figure 4.9. The flowchart of proposed method

4.4.5 Summary of implementation procedure

Algorithm 1 presents the pseudo-code of the proposed method for estimating $p_f(\mathbf{s}_i)$ for any given stress level $\mathbf{s}_i$. Following that, Algorithm 2 summarizes how Algorithm 1 is integrated with the overall framework to accomplish corrosion risk assessment using physics-based multi-scale simulations.

Next, we will use a practical miter gate application example to demonstrate the proposed framework.

Algorithm 1: Compute $p_f(\mathbf{s}_i)$ for any given stress level $\mathbf{s}_i$

Data: $[\mathbf{s}_t, \mathbf{u}_t], \mathbf{y}_t$
Result: Updated $[\mathbf{s}_t, \mathbf{u}_t], \mathbf{y}_t$
while $\xi^m < 5\%$ **do**
  Train GPR surrogate model $y = \hat{G}(\mathbf{s}, \mathbf{u})$ based on current $[\mathbf{s}_t, \mathbf{u}_t], \mathbf{y}_t$;
  Fix $\mathbf{s}$ at s_i, compute weight of each particle $w(\mathrm{u}^{(i)}|\Im)$ with Eq. (4.25);
  Obtain posterior samples $p(\mathrm{u}^{(i)}|\Im)$ with Eq. (4.26);
  Fit a Gaussian mixture model to get the PDF of $\hat{h}^*(\mathbf{u})$;
  Compute $p_f(s_i)$ with Eq. (4.28);
  Compute learning function $\Lambda(\mathbf{u})$ with Eq. (4.20);
  Identify $\mathrm{u}_{new} = \min_{\mathbf{u}} \Lambda(\mathbf{u})$;
  Compute $y_{new} = G(s_i, \mathrm{u}_{new})$;
  Add $[s_i, \mathrm{u}_{new}], y_{new}$ to the training data $[\mathbf{s}_t, \mathbf{u}_t], \mathbf{y}_t$;
  Divide the updated samples into group 1 and group 2 by Λ value;
  if $\Lambda(\mathbf{u}^i) > 2$ **then**
    $\Lambda(\mathbf{u}^i) \in$ group 1;
    Compute $\hat{N}_{G1}$
  else
    $\Lambda(\mathbf{u}^i) \in$ group 2;
    Compute $\hat{N}_{G2}$
  end
  Compute ξ^m with Eq. (4.33);
end

Algorithm 2: Integration of macroscale global surrogate and mesoscale local surrogate for corrosion reliability analysis of miter gates

Generate N input samples $[\mathbf{s}_t, \mathbf{u}_t]$;
Run local corrosion simulation and obtain $\mathbf{y}_t = [y^{(1)}, y^{(2)}, ..., y^{(N)}]$ where $y^{(i)} = G(\mathbf{u}^{(i)}, \mathbf{s}^{(i)})$;
for $i = 0$ *to* N **do**
  Train GPR surrogate model $y = \hat{G}(\mathbf{s}, \mathbf{u})$ based on current $[\mathbf{s}_t, \mathbf{u}_t], \mathbf{y}_t$;
  Compute $p_f(s_i)$ using Algorithm 1;
  Update training data $[\mathbf{s}_t, \mathbf{u}_t], \mathbf{y}_t$ from Algorithm 1;
end
Construct a surrogate model $p_f(\mathbf{s}) = \hat{p}_f(\mathbf{s})$ using $\mathbf{s}_t$ and $p_{f,t} = [p_f(\mathbf{s}_1), p_f(\mathbf{s}_2), ..., p_f(\mathbf{s}_N)]$;
Run global surrogate $\mathbf{s}_i(\mathbf{d}, k) = \hat{\pi}(a^k, \mathbf{v}^k, \mathbf{d})$ to obtain the stress response of on the miter gate;
Compute failure probability of any location on the gate $p_f(\mathbf{d})$ with Eq. (4.36);

4.5 Case Study

4.5.1 Problem statement

The US Army Corps of Engineers (USACE) owns and operates over two hundred navigational locks in the United States. As of 2017, more than half of the assets had been in service for more than 50 years [49]. Pitting corrosion is one of the most significant deterioration types on miter gates [49], which are the operation gates keeping the water level on both sides of the lock as shown in Fig. 4.10.

Figure 4.10. A lock with miter gates for inland waterway navigation.

To conduct the failure probability prediction of miter gates with respect to pitting corrosion, different uncertainty sources in different time scales need to be considered. The water level on the downstream side of the lock keeps changing from the lower water level to the higher water level or vice versa in every operation. Additionally, the water level on the upstream side is also changing slowly depending on the water level management of the whole waterway. In our study,

the downstream and upstream water levels are respectively modeled as Weibull and Gaussian distribution as shown in Table 4.1. The reaction coefficient and the diffusion coefficient θ are also changing with the chemicals in the water as well as the temperature during a long time in service. They are modeled as Gaussian distributions. A failure is defined as the time to SCC initiation being less than a time length of interest T_e, which is two years in our study.

Table 4.1. Sources of uncertainty and their proposed statistical distributions

Variable Name	Uncertainty Sources	Distribution Type	Distribution Parameter
Upstream Water Level (v_1)	Waterway elevation management	Gaussian	$\mu = 600$, $\sigma = 50$
Downstream Water Level (v_2)	Navigational lock operation	Weibull	$a = 2$, $b = 50$
Reaction Constant (θ_1)	Chemicals in water and temperature	Gaussian	$\mu = 5.5$, $\sigma = 1.5$
Diffusion Coefficient (θ_2)	Chemicals in water and temperature	Gaussian	$\mu = 2.6$, $\sigma = 0.75$

In our previous study, a high-fidelity FE model has been developed as depicted in Fig. 4.5. Based on this information, we perform corrosion reliability analysis for a miter gate by employing the method proposed in Sec. 4.4.

4.5.2 Global surrogate modeling of the strain response of the miter gate

In order to construct a global surrogate for the strain response of the miter gate, 1000 training samples of gap length and water level combinations are generated. FE simulations are then conducted using these training samples as inputs. Based on that, a surrogate model of the miter gate strain response is built using the method presented in Sec. 4.4.2. In this work, 9 features are employed to represent the strain response since they can account for 95% of the eigenvalue information (see Eq. (4.14)).

For illustration, the first six features (accounting for 90% of the eigenvalue information)

of the strain response obtained through singular value decomposition are shown in Fig. 4.11. One interesting observation is that some features, like the second and the third features, almost only capture the local response from the gap. The local response due to the gap is separated and well-captured by the singular value decomposition method used in this study. Since a similar approach has been adopted in our previous study, we refer interested readers to our previous study for details [149, 157]. Fig. 4.12 presents the prediction of the strain response from the trained surrogate model for a given gap length and water level combination. Only a two-dimensional plot is plotted for better visualization of the point cloud of the surrogate model prediction.

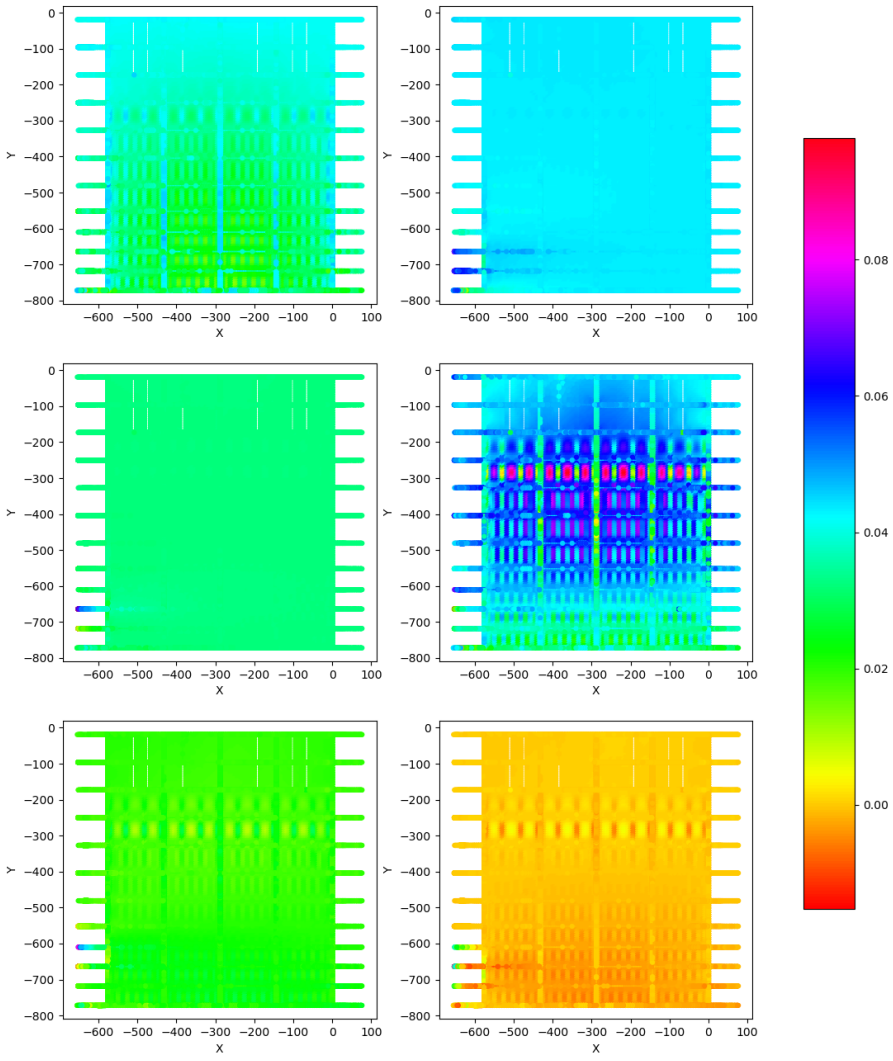

Figure 4.11. First six features of the strain response of the miter gate

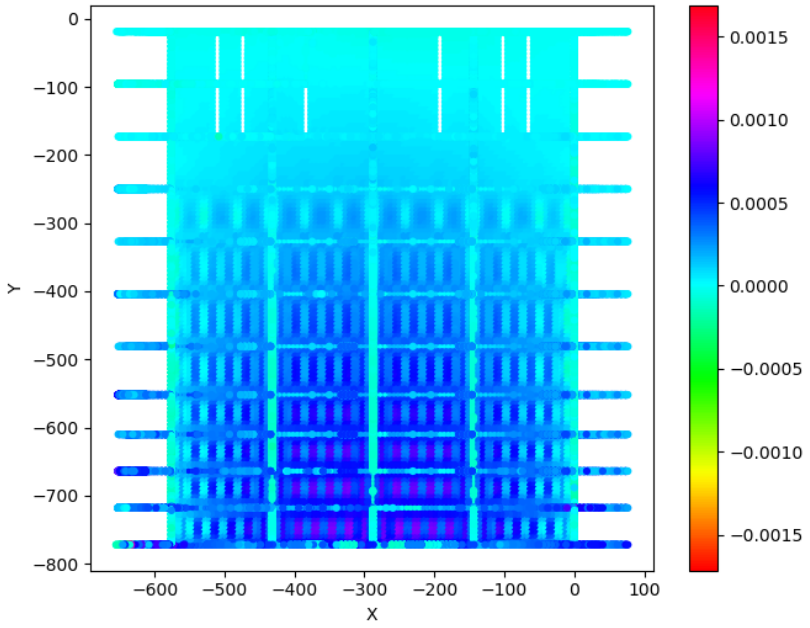

Figure 4.12. Predicted strain response of miter gate using global surrogate model

4.5.3 Adaptive local surrogate modeling of PF model for corrosion reliability analysis

Since a single run of the PF-based corrosion simulation takes over half an hour on our benchmark workstation, it is computationally impossible for us to verify the effectiveness of the proposed framework if the original PF model is used. In order to overcome this issue in the case study, a GPR surrogate model of the PF model is constructed in this section and is used as the original model for the purpose of verifying and comparing the performance of different methods including the proposed adaptive surrogate modeling in Sec. 4.4.3, the existing AK-MCS method, and MCS.

According to the algorithm presented in Sec. 4.4.3, we first generate 64 samples of $\mathbf{u}_t$, $\mathbf{s}_t$ and $\mathbf{y}_t$. Based on the initial samples, an initial GPR surrogate model $\hat{G}(\mathbf{s},\mathbf{u})$ is constructed. After that, the joint PDF of the approximated instrumental density $\hat{h}^*(\mathbf{u})$ for IS is sequentially updated to identify new training points for the refinement of the surrogate model. Fig. 4.13 shows some

examples of the updating of $\hat{h}^*(\mathbf{u})$ over iterations for three different stress level conditions. For each subplot in Fig. 4.13, the horizontal axis is the reaction constant denoted by u_1 and the vertical axis is the diffusion coefficient denoted by u_2. We can see that for $\mathbf{s}_5$, the distribution of u_1 concentrates around -1 after several iterations and continues to concentrate on a small range around -2.2. For $\mathbf{s}_{10}$, u_1 spreads to a small range around -0.5 and concentrates on an area near 1. For $\mathbf{s}_{15}$, u_1 concentrates on a range between -0.5 and 2 after 10 iterations and spreads to two narrow ranges at about 0 and 1. For different stress conditions, the proposed adaptive surrogate modeling algorithm can iteratively refine the different areas of the whole surrogate. Note that for different $\mathbf{s}_i$, the distribution of u_1 concentrates on narrow ranges while the distribution of u_2 remains a wide range after updating. This is because the influence from the reaction constant is more significant than that from the diffusion coefficient in our case.

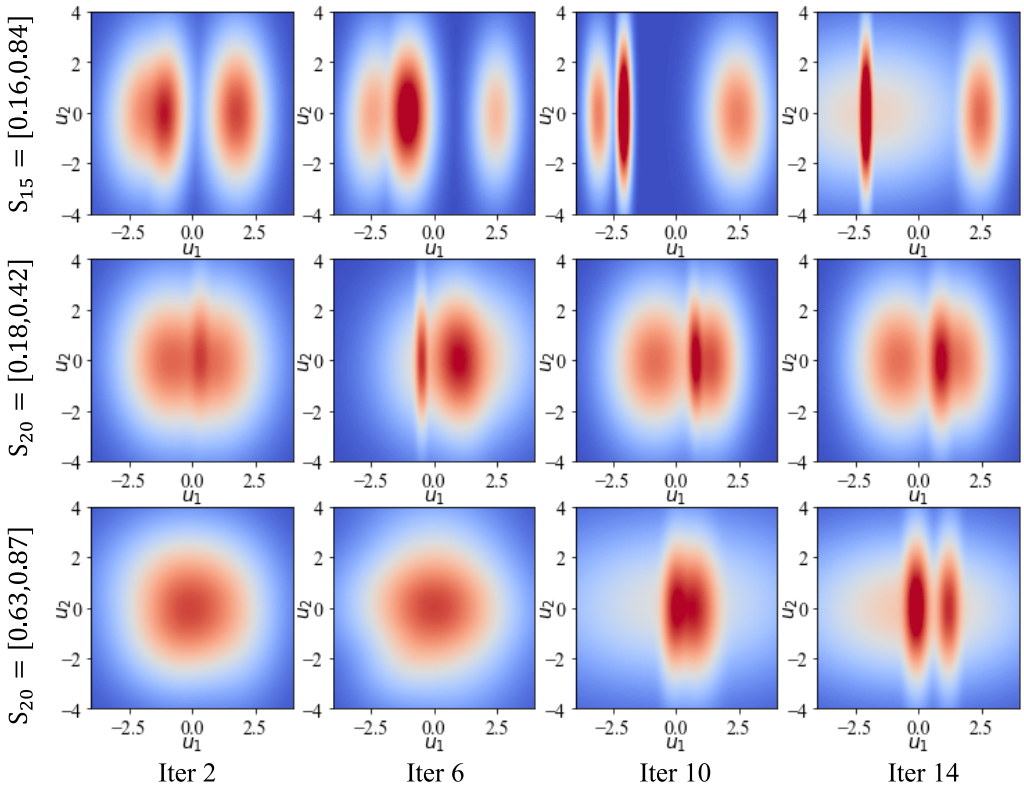

Figure 4.13. The joint PDF updating of u

Fig. 4.14 shows the convergence history of $p_f(\mathbf{s}_i)$ for different stress-level conditions.

We can notice that the proposed algorithm can converge quickly to a stable failure probability value for different stress conditions.

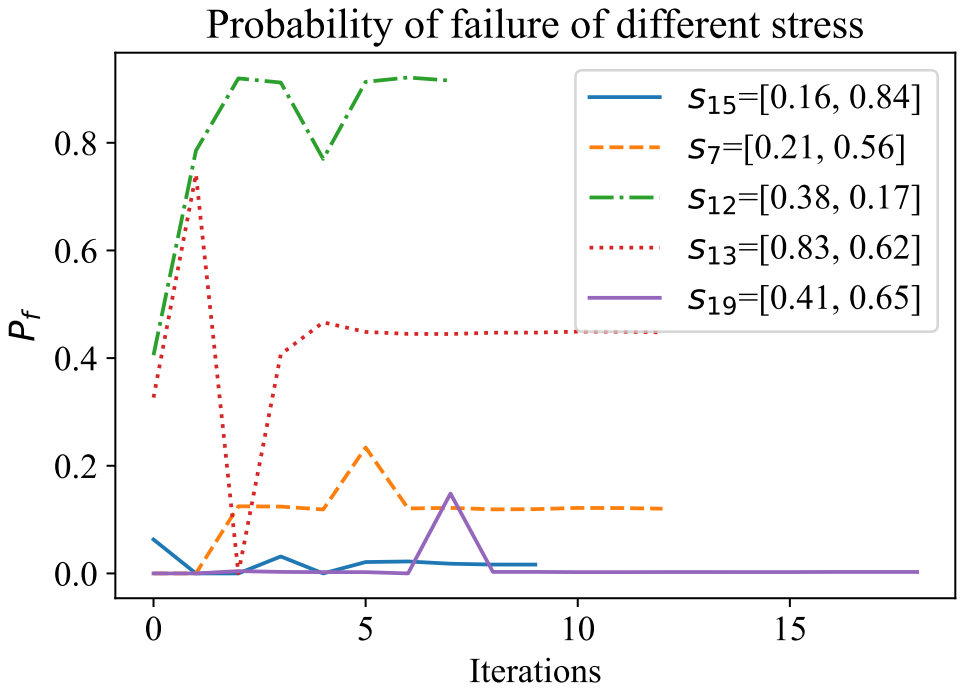

Figure 4.14. Convergence history of probability of failure for different $\mathbf{s}_i$

4.5.4 Comparison with the AK-MCS method

The proposed adaptive surrogate modeling for local surrogate modeling is also compared to the AK-MCS method [43]. Table 4.2 lists the number of function evaluations needed to converge for different stress conditions. As shown in this table, the proposed method needs far fewer functions than the AK-MCS method. Although the proposed method includes an extra step for Gaussian mixture modeling and IS, the overall computation cost has been significantly reduced since the required computational effort of the complex simulation for each new sampling point is much higher than the extra computational time introduced by GMM.

Table 4.2. The number of function evaluations needed by the proposed method and AK-MCS for different stress conditions

Stress Conditions	Proposed Method	AK-MCS
$s_0 = [0.1, 0]$	13	55
$s_1 = [0.55, 0.45]$	5	132
$s_2 = [0.775, 0.225]$	6	220
$s_3 = [0.325, 0.675]$	10	25
$s_4 = [0.438, 0.338]$	5	36
$s_5 = [0.887, 0.787]$	11	28
$s_6 = [0.662, 0.113]$	4	29
$s_7 = [0.212, 0.563]$	18	26
$s_8 = [0.269, 0.281]$	10	66
$s_9 = [0.719, 0.731]$	6	27
$s_{10} = [0.944, 0.056]$	13	30

4.5.5 Miter gate pitting corrosion reliability analysis

Fig. 4.15(a) depicts the failure probability value of each stress condition obtained using the adaptive local surrogate modeling method. Based on this, a surrogate model $\hat{p}_f(\mathbf{s})$ is trained as shown in Fig. 4.15 (b). After that, by integrating the global surrogate model with the adaptive local surrogate, the failure probability of any location $\hat{p}_f(\mathbf{d})$ on the miter gate can be calculated. Fig. 4.16 (a) shows the resulting corrosion failure probability map obtained using the proposed method. As shown in this figure, near the bottom of the gate has a high failure probability while above the water level has a very low failure probability. This is very similar to the corrosion pattern we found on multiple miter gates in the real-world as shown in Fig. 4.16 (b). There are two main reasons for this. First, the mechanical load under normal working conditions leads to a greater stress value at the bottom of the gate, which can contribute to the failure event we defined here. However, this failure probability map has a different distribution pattern from the stress distribution above the water level. This can be explained by the other reason, which is that $\mathbf{u}$, which are the reaction constant and the diffusion coefficient, in this case, has different distribution in the above-water-level part and under-water-level part. The reaction constant and the diffusion coefficient are much lower for the above-water level locations than those under-water level

locations. This is attributed to the fact that the electrochemical reactions for the metal in the water and the air are different. Therefore, the failure probability map has small values for all the above-water-level parts.

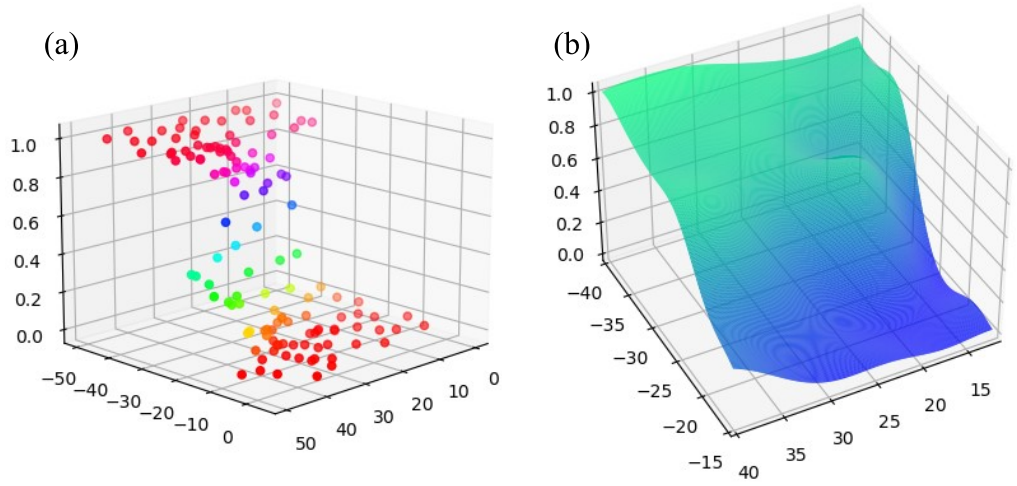

Figure 4.15. Training points of failure probability of given stress (a) and surrogate model surface (b)

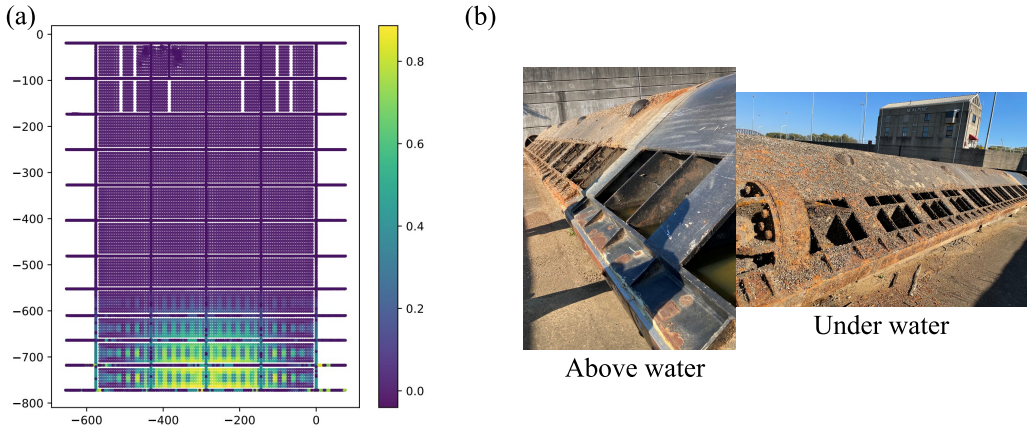

Figure 4.16. Probability of failure on miter gate (a) and different parts of a real-world corroded miter gate (b)

4.6 Conclusions

this work proposes a physics-based corrosion reliability analysis method. The proposed method connects the mesoscale corrosion simulation to the macroscale mechanical simulation by mechanical stress, enabling the reliability analysis for the whole structure based on high-fidelity models. The SCC initiation risk map for the entire structure is generated with the proposed method. The uncertainties from different scales and sources are well-considered in the reliability analysis with the multi-scale simulations. Moreover, the local adaptive surrogate modeling method can reduce the number of iterations needed for the performance function, which can save a significant amount of computational cost. This approach combines the advantages of AK-MCS and IS. The idea for this is to reduce the evaluation times in surrogate modeling. Instead of refining the model in the whole design space which can be expensive, the adaptive surrogate modeling refines the model by adding a new sample point sequentially from the important samples identified with instrumental density function to the design of experiments. The best next sample point is determined by the learning function. This adaptive surrogate modeling method is compared with the existing AK-MCS method and the result shows the proposed method can significantly further reduce the number of evaluations.

The proposed method uses an existing two-dimensional PF simulation for the local corrosion simulation. This can be improved by using a three-dimensional simulation and achieving a better connection with the macroscale mechanical stress simulation. The interaction between mesoscale corrosion simulation and global mechanical stress simulation is not fully-coupled in the current method. The global influence of the corroded location on mechanical stress is not considered based on the assumption that the pitting corrosion and the SCC deterioration are local. These topics are worth investigating in our future work.

4.7 Remarks

Material for this chapter was published in the following articles:

[1] **Guofeng Qian**, Zhen Hu, and Michael D Todd. Physics-based corrosion reliability analysis of miter gates using multi-scale simulations and adaptive surrogate modeling. *Mechanical Systems and Signal Processing*, 200:110619, 2023.

[2] **Guofeng Qian**, Zhen Hu, and Michael D Todd. Physics-based corrosion reliability analysis of miter gates using multi-scale simulations. *In Society for Experimental Mechanics Annual Conference and Exposition*, pages 101–105. Springer, 2023.

Chapter 5

Pitting Corrosion Diagnosis and Prognosis in Civil infrastructure

5.1 Abstract

Physics-based high-fidelity pitting corrosion simulation models have been successful in predicting the evolution of pit morphology for given mechanical and environmental conditions. However, applying such models for pitting corrosion diagnostics and prognostics in large civil infrastructures is very challenging, primarily due to the impracticality of measuring individual pits. this work overcomes this challenge by bridging the gap between physics-based pitting corrosion simulation and vision-based pitting corrosion inspection of large civil infrastructures. The framework proposed in this work consists of four main modules, namely mesoscale pitting corrosion simulation using the phase-field method, macro-scale structural analysis, pitting corrosion detection using machine learning, and updating physics-based simulation models based on pitting corrosion detection. It begins with the development of a forward simulation framework to predict the evolution of pitting corrosion on large civil infrastructures using multi-scale analysis. A convolutional neural network (CNN)-based pit detection method is created in parallel to autonomously identify and extract pitting corrosion observations from corrosion inspection images. Finally, an approximate Bayesian computation numerical framework is proposed to update three key model parameters in the forward pitting corrosion simulation model using the detection results from the trained CNN model. The updated multi-scale simulation model can

then be used for pitting corrosion prognostics. A practical application example of miter gates is used to demonstrate the effectiveness of the proposed framework.

5.2 Introduction

Corrosion stands out as a prevalent form of deterioration in large infrastructures within inland navigation systems [46] as Figure 5.1 shows. The corrosion pits exhibit variations in both their shapes and depths. Notably, pitting corrosion, recognized as the most destructive type of corrosion [3], poses a unique challenge due to its localized nature, making detection difficult while potentially leading to severe consequences for structural integrity [159]. Moreover, the initiation and propagation of cracks, as shown in Figure 5.1, can result from pitting corrosion [36]. In the context of large civil infrastructures, the presence of varying mechanical loads, a common working condition, significantly influences the growth of pitting corrosion [115]. Therefore, the imperative development of a comprehensive diagnosis and prognosis framework for addressing pitting corrosion in civil infrastructure is underscored.

Many data-driven methods necessitate historical failure data, as statistical algorithms lack an understanding of physical failure mechanisms. Nevertheless, acquiring such failure data is frequently challenging for civil infrastructure, and generating it through reasonable approaches proves to be a formidable task. Faced with these constraints, there is a notable inclination towards physics-based prognostics for civil infrastructure. Another noteworthy distinction lies in the fact that the Data-Driven approach heavily relies on measurements, with minimal consideration of underlying physics. In contrast, the model-based approach can provide estimates even in the absence of measurements. Furthermore, when diagnostic information becomes available, the model can be refined or updated based on this additional information.

Computational models for pitting corrosion, such as cellular automata (CA), peridynamics (PD), and phase field (PF), have been established, with the PF model being particularly popular due to its versatility and capacity to encompass various factors in pitting corrosion simulation

Figure 5.1. Pitting corrosion images on miter gates [77] (Courtesy of Brian Eick)

[9, 118]. Nevertheless, these models, relying on the solution of partial differential equations, come with a computational cost. To mitigate this, accelerated surrogate models utilizing machine learning algorithms have been introduced [103, 104]. These surrogates enable rapid predictions and probabilistic analyses for pitting corrosion. Notably, however, these models have not been effectively integrated or updated with real-world measurements.

To overcome these limitations, we present a comprehensive framework for diagnosing pitting corrosion in civil infrastructure, leveraging strain measurements and images. Following the diagnosis, we conduct prognostics with the model updated based on the diagnostic results. Surrogate models are implemented to accelerate physics-based simulations, enabling swift

predictions. Additionally, we establish a link between mesoscale corrosion simulation and macroscale structure simulation through a multi-scale approach.

5.3 Corrosion Diagnostics and Prognostics Framework

5.3.1 Overview of the Proposed Framework

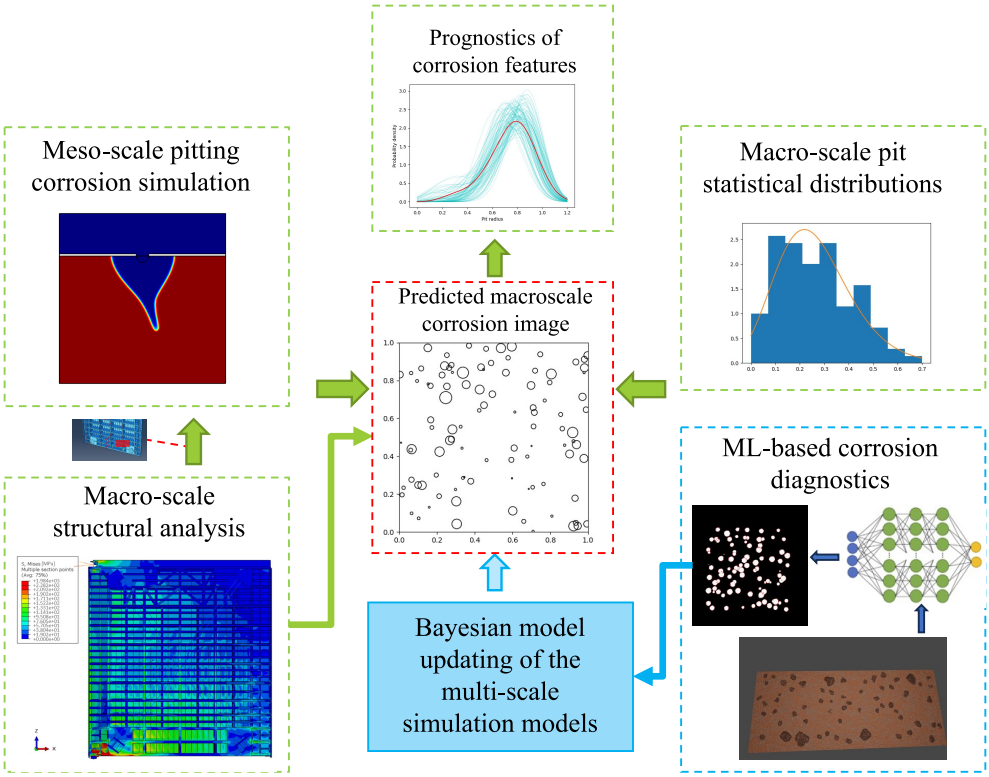

Figure 5.2. Corrosion diagnostics and prognostics scheme

The proposed framework comprises three main components, as illustrated in Figure 5.2. On the left side, a meso-scale pitting corrosion simulation incorporates mechanical input from macro-scale structural analysis. The upper right section introduces a macro-level pit initiation statistical model, presenting a multi-scale pitting corrosion simulation approach for predicting pitting corrosion on large structures. Synthetic images are then utilized to measure corrosion location and radius through a machine learning-based corrosion detection algorithm, depicted in the lower right blue box. The detection outcomes play a crucial role in updating the three

key parameters in the forward simulation via the proposed approximate Bayesian computation framework. Subsequently, pitting corrosion prognosis is conducted using the updated parameters through a multi-scale prediction model.

5.3.2 Multi-Scale Simulation for Pitting Corrosion Prediction

Mesoscale pitting simulation under dynamic loads

The loading conditions on the structures or components frequently display stochastic fluctuations over time, characterized by non-stationary statistical behaviors. The mechanical load is generated by the Karhunen–Loève expansion based on the water level history data as illustrated in the paper [115]. The authors implemented phase-field method described in Sec. 2.3 on a two-dimensional plate subjected to dynamic normal stress and shear stress, applied to one side of the plate. Pitting corrosion initiates and propagates from the top center region. The single pit metastable evolution model simulates the corrosion morphology evolution under altering mechanical load history, $\mathbf{y}_{1,k}$, and static reaction coefficient, θ. The corrosion evolution displayed varying growth speeds, directions, and shapes. This simulation highlights the substantial influence of dynamic loads on the corrosion process. The corrosion morphology Ω_k at time t_k can be obtained by the simulation as Equation 5.1 shows.

$$\Omega_k = \mathscr{G}\left(\mathbf{y}_{1:k}, \Omega_0, \theta, T_{ini}\right), \tag{5.1}$$

where $\mathscr{G}(\cdot)$ represents the physics-based phase-field simulation, $\mathbf{y}_{1:k}$ is the stress from time t_1 to t_k, Ω_0 is the corrosion morphology at time t_0, T_{ini} is the pit initiation time of a certain pit, and θ is the environmental coefficient.

Macroscale structural analysis

The principal load acting on the miter gate structure is the hydrostatic pressure under different water elevations from both sides. Over years of service, a common form of deterioration involves the development of gaps between the lock wall and the quoin block. The model is

specifically developed for stress analysis and boundary contact analysis. Under a specified water level v_k and gap length a_k, the strain response of the macro structure at spatial location d, denoted as $\mathbf{s}_{d,k}$, is simulated using a linear and elastic Finite Element (FE) model consisting of 64,919 4-node reduced integration shell elements. To enhance accuracy, strain measurements are employed to update the overall stress response of the structure [150]. This step is mathematically represented by Equation 5.2.

$$\mathbf{s}_{d,k} = \mathscr{F}(a_k, v_k, d), \tag{5.2}$$

where $\mathscr{F}$ is the FE analysis model. Based on the FE model, a reduced-order, Gaussian process regression model for strain analysis was developed using principle component analysis to predict strain gauges [149]. The implementation of the reduced-order model significantly reduces the computation time from over 2 minutes to less than 1 second for a single simulation, thereby facilitating rapid predictions of the macro structural stress response. The Equation 5.2 can be represented with Equation 5.3.

$$\hat{s}_{d,k} = \hat{\mathscr{F}}(a_k, v_k, d), \tag{5.3}$$

where the $\hat{\mathscr{F}}(\cdot)$ is the surrogate model of the FE analysis model.

Macro-scale Pitting Corrosion Feature Prediction Using multi-scale Simulation

To facilitate the simulation of multiple pit evolutions on the macro structure, we introduce a multi-scale simulation approach that establishes a connection between mesoscale single pit simulations and the macroscale structure.

For simulating multiple pits based on the behavior of a single pit at the local level, obtaining information about multiple pit initiation times and locations is crucial. Pit initiation stems from the breakdown of the local passive film, a process involving intricate mechanisms of nucleation and early propagation, currently under active research [51, 83, 84, 86, 87].

Given the complexity of these mechanisms, we resort to statistical information to describe this stage. The passive film breakdown event is modeled as a nonhomogeneous Poisson process [12], and the Weibull distribution has been identified as a suitable fit for the pit initiation time distribution [11, 89]. In this study, we generate pit initiation times for the p-th pit, denoted as $T_{ini,p}$, using the Weibull distribution with parameters λ and η, as shown in Equation 5.4.

$$T_{ini,p} \sim W(\lambda, \eta), \tag{5.4}$$

The number of pits N_k at t_k can be calculated with $T_{ini,p}$ by

$$N_k = \sum_{p=1}^{N_p} \mathbb{1}_{T_{ini,p} <= t_k}(T_{ini,p}), \tag{5.5}$$

where $\mathbb{1}(\cdot)$ is the indicator function that equals to 1 if $T_{ini,p} <= t_k$ else 0, N_p is the maximum number of pits that can be initiated within the time of interest N_t. N_p is influenced by material, environmental factors as well as the initiation mechanism. In this study, we select this value according to the measurement results of the steel components in a bulk carrier by Paik et al [113] as the long-term pitting corrosion measurements on infrastructures are extremely limited.

Furthermore, we have identified that the spatial distribution of corrosion pits displays characteristics of both randomness and regular spacing, as observed in the research by Cawley et al. [27]. The local pit locations are generated using a joint uniform distribution. It's important to note that, in this study, we have not accounted for the influence of mechanical stress on the pit nucleation stage. The procedure of the multi-scale simuation is shown in Figure 5.3.

With the ability to simulate multiple pits at the local level, the local stress response history obtained from macroscale structural analysis at specific locations is employed as the mechanical load input for the local corrosion model. Notably, due to the gradual nature of corrosion, the dynamic load on corrosion is generated with a 15-minute interval water level history, consistent with the water level monitoring data. Therefore, changes in water level are

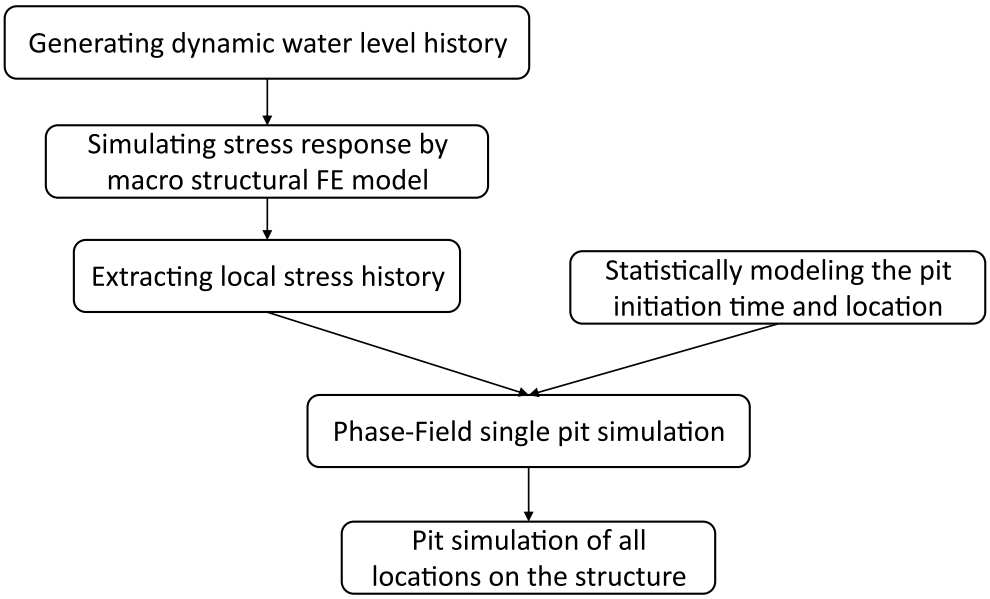

Figure 5.3. Flowchart for proposed multi-scale pitting corrosion simulation

considered pseudo-static in relation to the stress response. Consequently, the stress response, denoted as $\mathbf{y}_{1,k}$, is simulated multiple times for each time step of the mechanical load history, as shown in Equation 5.6, thus generating the stress load history for the macro structure.

$$\mathbf{y}_{1,k} = \hat{\mathscr{F}}\left(a_k, \mathbf{v}_{1,k}\right), \tag{5.6}$$

where $\mathbf{v}_{1,k}$ is the water level history data.

It is crucial to emphasize that the stress response is one-way coupled to the pit evolution. In this study, we do not consider the stress redistribution resulting from corrosion growth, as our primary focus is on the local corrosion evolution stage preceding significant material loss or structural failure.

Surrogate Modeling to Accelerate Pitting Corrosion Features Prediction

To evaluate the extent of pitting corrosion damage, three critical damage features—namely, pit depth γ_k, pit opening diameter α_k, and curvature c_k—are extracted from the simulation results Ω_k, as illustrated in Figure 5.4. Pit depth is identified as one of the most

crucial damage features in pitting corrosion, exerting a significant influence on component strength, as observed by Apostolopoulos et al. [10]. The selection of pit opening diameter is based on its ease of detection using image measurements. Lastly, curvature at the pit's tip location serves as a vital indicator for potential corrosion-induced cracking initiation, as highlighted in the study by Qian et al. [118].

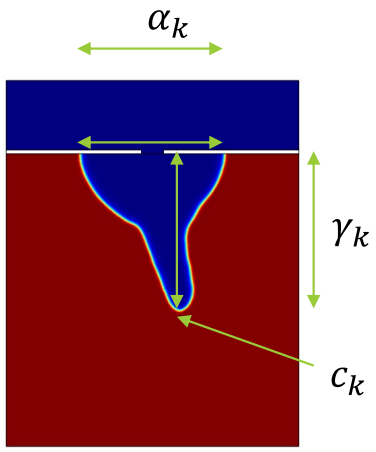

Figure 5.4. The pit depth, pit opening diameter and the curvature extraction

To enhance optimal maintenance strategies or decision-making in the structural health monitoring (SHM) system, the diagnostics and prognostics stages necessitate the execution of predictive models thousands of times within a short timeframe. Additionally, real-time monitoring systems require swift predictions for prompt responses. However, multiple nonlinear, coupled partial differential equations (PDEs) are inherently computationally demanding. A single corrosion simulation can take more than an hour to compute on a workstation with 10 cores of an Intel(R) Xeon(R) W-2155 CPU. To address this computational challenge, a machine learning-based surrogate model is applied to expedite feature prediction.

We employ a Gaussian process regression (GPR) model with a nonlinear autoregressive exogenous inputs (NARX). A notable advantage of this specific machine learning model is its ability to not only provide mean predictions but also offer confidences in a closed form. To predict the features at time step k, we construct three GP-NARX models for the three features,

utilizing information from the features and load of the previous N_t time steps in Equation 5.7.

$$\begin{aligned}
\gamma_{k+1} &= \hat{G}_1\left(\mathbf{y}_{(k-4):(k+1)}, \gamma_{(k-4):k}, \alpha_{(k-4):k}, \mathbf{c}_{(k-4):k}\right) + \varepsilon_{1,k+1} \\
\alpha_{k+1} &= \hat{G}_2\left(y_{(k-4):(k+1)}, \gamma_{(k-4):k}, \alpha_{(k-4):k}, c_{(k-4):k}\right) + \varepsilon_{2,k+1} \\
c_{k+1} &= \hat{G}_3\left(y_{(k-4):(k+1)}, \gamma_{(k-4):k}, \alpha_{(k-4):k}, c_{(k-4):k}\right) + \varepsilon_{3,k+1},\ i = 0,1,...,N_{pred}
\end{aligned} \tag{5.7}$$

where N_{pred} represents the time steps needed by GP-NARX to predict the features of the next step. By recursively applying Equation 5.7 as illustrated in Figure 5.5, the damage features at any time step $k, k > T_i$ can be predicted with Equation 5.8 from initiation time T_i.

$$\gamma_k, \alpha_k, c_k = \hat{G}\left(\mathbf{y}_{T_p,k}, \gamma_0, \alpha_0, c_0, \theta\right), \tag{5.8}$$

where γ_0, α_0, c_0 are the initial features at the pit initiation time T_p.

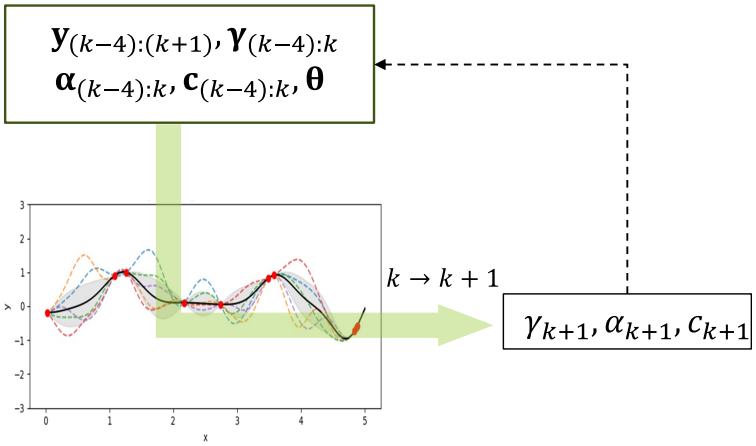

Figure 5.5. GP-NARX architecture for surrogate modeling

5.3.3 Machine Learning-Based Pitting Corrosion Identification and Detection

The multi-scale physics-based corrosion simulation with surrogate modeling enables acquiring accurate pitting information at each step under dynamic loads. Based on the physics information developed in the last section, vision-based pitting corrosion inspection can be

achieved if image inspection data are available in the process of the forward problem. However, in cases like corrosion analysis, acquiring real-world data in sufficient quantity and diversity can be challenging. This is where synthetic image data generation, particularly using advanced 3D computer graphics software like Blender, becomes invaluable.

Synthetic Image Data Generation Using Blender

Blender is a free and open-source 3D computer graphics software, offering comprehensive tools that enable users to create detailed and physically accurate simulations. [136, 106, 78, 144, 124] The powerful tools enable Blender to generate synthetic datasets that accurately represent pitting corrosion over time. These datasets will serve as training samples for convolutional neural network (CNN) models, aimed at identifying and predicting the progression of corrosion in large-scale steel structures.

The process in Blender involves simulating the dynamic evolution of corrosion pits on steel surfaces. This is achieved through a series of steps, starting from the creation of a 3D plate to represent the metallic base. The progression of corrosion is then simulated according to imported pitting information from the last section, generating pit shapes, and applying realistic modifications to mimic the stochastic nature of actual corrosion processes. The final step involves rendering the corroded plate at multiple angles of view and at various stages of pit development, thereby creating a series of images that capture the progression of pitting corrosion. These images allow for training CNN models for vision-based pitting corrosion detection.

Convolutional Neural Network (CNN) for Pitting Corrosion Identification

CNNs are a class of deep neural networks that consist of multiple layers that automatically and adaptively learn spatial hierarchies of features from input images. These features range from edges and patterns at lower layers to high-level features and object classes at deeper layers. The CNN models are well-known for tasks such as image classification, segmentation, and object detection [60, 5, 111], which are critical in the context of pitting corrosion identification .

The core component of a CNN is the convolutional layer, which applies a series of learnable filters with adjustable sizes to the input images. This operation captures local dependencies of features to identify (pitting holes in this work). Through the use of pooling layers, CNNs downsample the captured features for the model's invariance to local translation, making them robust to small translations of the input. For the purpose of pitting corrosion detection, where the task is to identify and localize corrosion on a pixel level, a specialized form of CNN known as U-Net is employed [75, 24, 32, 102].

The U-Net architecture was originally designed for biomedical image segmentation, offering precise object detection by combining a contracting path to capture context and a symmetric expanding path that concatenates lower-layer features with deeper-layer features. This architecture is particularly well-suited for the task of pitting corrosion identification, as it requires the model to learn the pitting corrosion at different scales. As shown in Figure 5.6, the U-Net architecture, as employed in our study, is designed for a 512x512 pixel input image. The architecture follows a symmetrical design with two main paths - the contracting (downsampling) path and the expansive (upsampling) path.

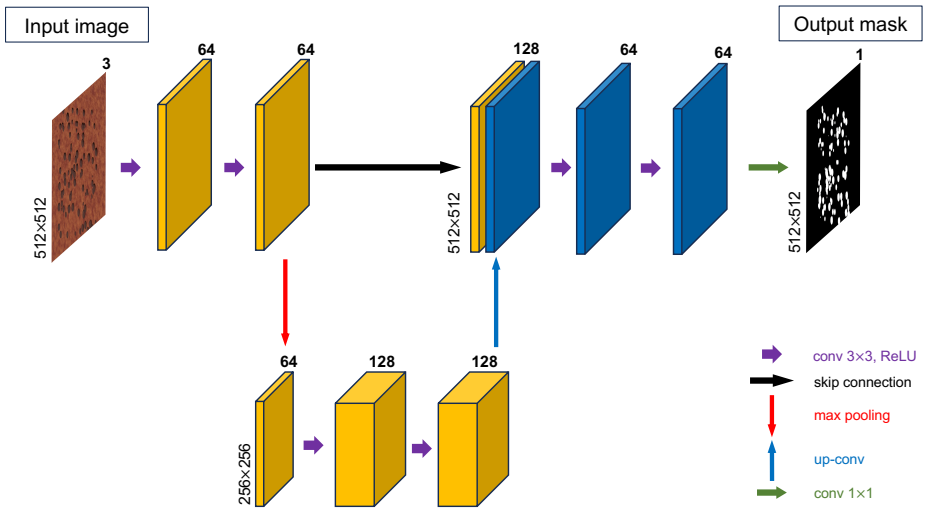

Figure 5.6. The architecture of a U-Net neural network for pitting corrosion identification.

The contracting path begins with an input layer of dimensions 512x512x3 (typically

for RGB images). The first convolutional block consists of 3x3 convolutions, stride 1, and padding 1, producing an output of dimensions 512x512x64. This is followed by a max pooling layer with a 2x2 kernel and stride 2, reducing the spatial dimensions to 256x256x64. Further convolutional blocks follow this pattern, each time doubling the number of filters while halving the spatial dimensions. The final layer in this path has dimensions 256x256x128. To the right part of the architecture, the expansive path begins with an upsampling layer that increases the spatial dimensions, followed by convolutional layers. The first upsampling layer enlarges the input to 512x512x128. The subsequent convolutional block reduces the channel dimensions to 512x512x64.

This path essentially mirrors the contracting path but in reverse, gradually increasing the spatial resolution while decreasing the depth. The skip connections, as indicated as solid black arrow in the figure, connect corresponding layers in the contracting path to the expansive path. These connections are crucial as they allow the network to use fine-grained details from the contracting path for precise localization during upsampling.

Final convolution and output have a final 1x1 convolutional layer that consolidates the feature map into a single channel, resulting in an output dimension of 512x512x1. This output represents the segmented image, where each pixel is classified as either part of a corrosion area or not. It is important to note that the figure of the U-Net model, as presented in this work, reflects this simplified architecture. It demonstrates a single convolutional block in both the contracting and expansive paths, with a proportional reduction in spatial dimensions and a corresponding increase in feature depth at each stage. For more complex corrosion patterns, the network can be deepened by adding convolutional blocks. This enhancement allows for the processing of intricate features at the expense of increased computational demand.

To generate the ground truth as the training output for the CNN model, the synthetic dataset is further augmented with binary masks for pixel-level segmentation. These masks label the corroded from the non-corroded areas, with pixel values set to 255 for regions exhibiting pitting and 0 for all other regions. The CNN training process involves feeding the synthetic

images and their corresponding masks into a U-Net model. The U-Net architecture is optimized through back propagation and gradient descent algorithms, minimizing a loss function that quantifies the difference between the predicted segmentation and the ground truth masks.

Through the employment of a U-Net CNN trained on several generated synthetic datasets, a robust CNN model for machine learning-based pitting corrosion identification and detection is available, for further applications in corrosion diagnostics and prognostics.

Interpreting Pitting Corrosion Output

Assume the input image, denote as x, is passed through the U-Net model, where the output of the U-Net model y after a series of convolutional, pooling, and upsampling operations can be represented as follows

$$y = f_{\text{U-Net}}(x) \tag{5.9}$$

where y is a matrix of the same spatial dimensions as x but represents the raw prediction for each pixel.

The raw output y is then passed through a sigmoid activation function σ to convert them into probabilities as follows,

$$p = \sigma(y) = \frac{1}{1+e^{-y}} \tag{5.10}$$

This function ensures that the output for each pixel of the prediction lies between 0 to 1, which can be interpreted as the probability of the presence of corrosion. Upon obtaining the sigmoid output, these probabilities are typically converted into binary values for clear segmentation by applying a pre-defined threshold T. The binary pixel-level identification result $\tilde{\chi}$ is obtained as follows:

$$\tilde{\chi} = \begin{cases} 1 & \text{if } p > T \\ 0 & \text{otherwise} \end{cases} \tag{5.11}$$

where the threshold level T can be determined based on the specific requirements of the task and to reflect the risk of underestimating corrosion. The binary pixel-level identification result $\tilde{\chi}$ presents that pixels with values above the threshold are classified as 'corrosion' (1), while those below are classified as 'non-corrosion' (0).

In scenarios where multiple classes of corrosion are involved, such as differentiating various severity levels of corrosion, a softmax activation function would typically be used. This function extends the capability of the model to handle multi-class classification by outputting a probability distribution over multiple classes. It assigns a probability to each class for each pixel, ensuring that the sum of these probabilities equals 1. However, this work primarily focuses on the aspect of feature extraction using CNN models in the context of binary classification for corrosion detection. Thus, quantifying the severity or classifying multiple types of corrosion falls beyond the scope of our current study.

5.3.4 Pit Feature Extraction from Observation

The corrosion depth γ_k is acknowledged as a crucial feature of corrosion damage. However, accurately identifying pit depth from normal-scale images poses challenges. Firstly, the depth direction typically lies in the out-of-plane direction on the image due to the camera location, diminishing the depth information on the image. Additionally, the scale of pit depth is much smaller than the distance between the camera and pits. The presence of rust and stains on the pit surface introduces additional noise for depth identification. Consequently, direct measurement of depth is not performed in this study.

Despite the challenges in directly measuring depth from images, the pit depth γ_k can be inferred from the opening width α_k using Equation 5.8, given the mechanical load history $\mathbf{y}_{T_p,k}$. Conversely, the opening width can be identified from images since this information is directly

visible.

To achieve this, we propose an advanced feature extraction algorithm based on pixel-level corrosion identification results, incorporating a super-resolution network and a circle detection algorithm. Initially, the enhanced deep super-resolution network (EDSR) by Lim et al. [92] is employed to improve resolution and reduce noise in the binary identification results, as illustrated in [Reference to the specific figure]. EDSR is designed to optimize performance by eliminating redundant modules often present in conventional residual networks, resulting in a significant overall efficiency enhancement.

Subsequently, morphological closing by dilation and erosion is applied to fill small holes between overlapping pits. The distance transform is then performed on the morphological closing results. The feature extraction algorithm combines the distance transform with a disk and the previous results, identifying local maxima as indicators of pit location $\hat{d}_{pk}$ and radius $\hat{\alpha}_{pk}$ for pit p at time k, as shown in Equation 5.12.

$$\hat{\alpha}_{kp}, \hat{d}_{kp} = I(\tilde{\chi}),\ p = 1, ..., \hat{N}_k,\ k = T_i, ..., N_t, \tag{5.12}$$

where I is the feature extraction algorithm, $\tilde{\chi}$ represents the pixel-level identification result from Section 5.3.3, the total number of pits identified at the current time point.

5.3.5 Parameter Updating from Features Identified

The Approximate Bayesian Computation (ABC) algorithm is employed to iteratively update three parameters, λ, η, and θ in the forward model. This process unfolds in two steps, each corresponding to a stage in the forward model. The flowchart of the updating procedures is presented in Figure 5.7.

Step 1: Updating λ and η in the Weibull Distribution

In this stage, the two parameters $x = [\lambda, \eta]$ in the Weibull distribution for the pit initiation time are initially updated using the pit numbers identified from the measurements $\hat{N}_k$. Given the

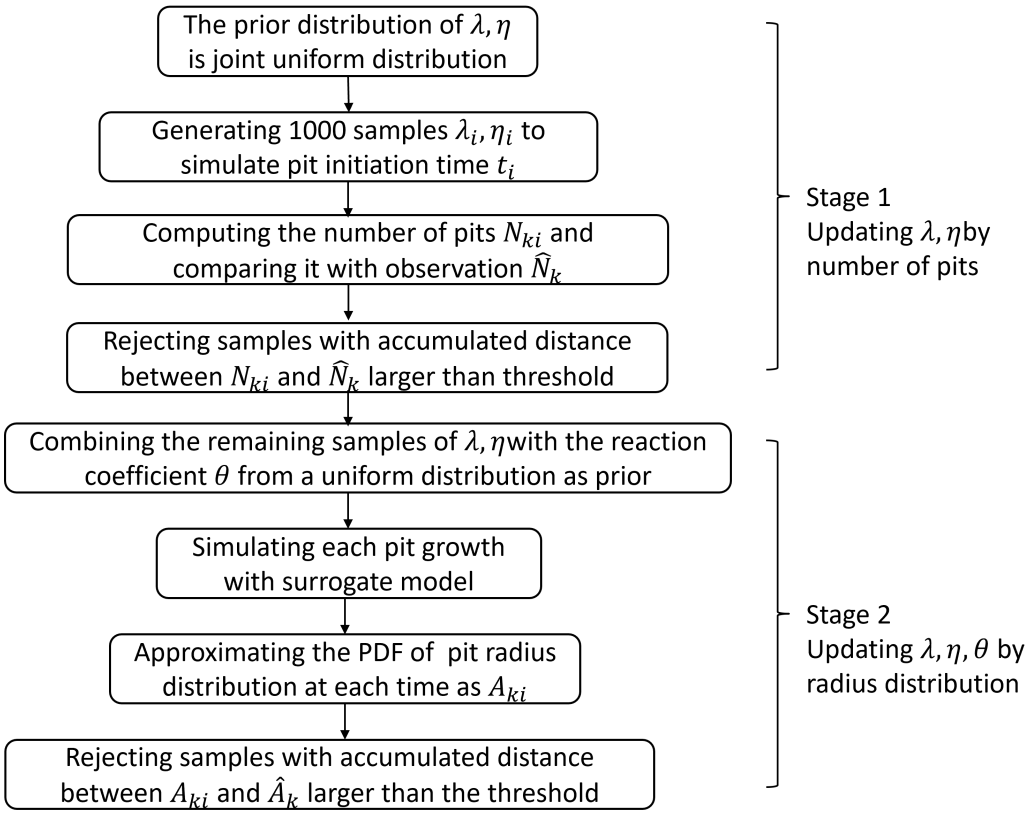

Figure 5.7. Flowchart of updating procedures

absence of prior information about the pit initiation time, a uniform distribution is used as the prior distribution $X_{prior} \sim U$. 1000 samples are generated from the prior distribution and fed into the Weibull distribution $W(x_i)$ to generate pit initiation time samples T_i. The pit number N_{ki} at time k for the ith realization is calculated. The error between N_{ki} and $\hat{N}_k$ is computed using Equation 5.13.

$$\varepsilon_{i1} = \sum |N_{ki} - \hat{N}_k|, \quad k = T_i, ..., N_t \tag{5.13}$$

The error threshold ε_{th1} is set to ensure an adequate number of posterior samples for the subsequent update. The posterior samples of stage 1, denoted by x_{mid}, are selected as $x_{mid} = x[\varepsilon_{i1} < \varepsilon_{th1}]$.

Step 2: Refining x_{mid} and θ with $\hat{\alpha}_k$ Distribution

In the second step, three parameters, including two from x_{mid} and the reaction constant θ, are further refined with the distribution of $\hat{\alpha}_k$. The prior distribution is also assumed to be uniform, denoted as $\theta_{prior} \sim U$. An equal number of samples for θ_i is generated and concatenated with x_{mid} as the new prior samples.

For each pit p, the surrogate model for feature prediction in Section 5.3.3 is applied to predict pit diameters α_{kp} at time k, as shown in Equation 5.14.

$$\alpha_{kp} = \hat{G}(\mathbf{y}_{T_p,k}, \theta_p, \gamma_0, \alpha_0, c_0) \tag{5.14}$$

The error between the measurements $\hat{\alpha}_{kp}$ and the simulation α_{kp} is not calculated directly due to the randomness in the pit evolution. Instead, an error metric is devised using the approximated probability density function (PDF) fitted to all pit diameters at time k. The error metric is given by Equation 5.15.

$$\varepsilon_{i2} = \sum_{k=0}^{N_t} |f(A_{ik}) - f(\hat{A}_k)| \tag{5.15}$$

Here, A_{ik} represents the diameter distribution at time k for the ith sample, $\hat{A}_k$ is the diameter distribution measured at time k, and $f(\cdot)$ represents the approximated PDF, estimated using kernel density estimation.

Similar to stage 1, an error threshold ε_{th2} is set to retain posterior samples for stage 2, denoted as $[x, \theta]_{post} = [x, \theta]\,[\varepsilon_{i2} < \varepsilon_{th2}]$.

5.4 Case Study

5.4.1 Problem Statement

The application of the proposed framework was demonstrated on the Greenup miter gate, a component of the Greenup Locks and Dam system, situated approximately 341 miles

downstream of Pittsburgh. The Greenup miter gate is prone to corrosion, especially in the context of fatigue cracks induced by exposure to water and debris. The debris not only directly contacts the material but also causes substantial damage to the corrosion-protective paint layer on the surface, making the pits more likely to initiate fatigue cracks. Corrosion is also a significant factor contributing to the loss of contact between the gate and the contact wall, a crucial concern for maintenance [81, 44]. The implementation of the Structural Health Monitoring (SHM) system and prognostics can significantly reduce both direct and indirect maintenance costs by offering more reliable physics-based diagnosis and prognosis. The Greenup Locks and Dam incur substantial costs, approximately 14 million in direct tow-operating costs to the industry, with just one unscheduled maintenance closure [58].

The Greenup miter gate's dimensions are 19.35 by 18.75 meters (Figure 5.8). In this study, the upstream and downstream water levels are simulated using KL-expansion based on historical data, with the gap length remaining fixed as the primary focus is on pitting corrosion. Future work may explore multi-modes damage diagnostics and prognostics.

Figure 5.8. Picture of a lifted miter gate at Greenup

A validated high-fidelity Finite Element (FE) model of the Greenup miter gate from a previous study [44] was utilized. Due to the limited availability of real pitting corrosion images

with varying damage levels, synthetic images were employed to train the diagnostics algorithms. Additionally, synthetic data with added noise was used as continuous measurement images, addressing the scarcity of long-term continuous monitoring data for pitting corrosion on the structure. While the value is not specifically calibrated for the Greenup miter gate, the reaction constant θ was calibrated using literature data and serves as the reference value for updating. Pit initiation time data for the miter gate is limited, so the λ, η values were approximated based on pit corrosion data from a bulk carrier [113].

Given that corrosion is a long-term process and accumulating monitoring data takes time, the study employed a state-of-the-art synthetic data generation approach to demonstrate the validity of the proposed framework. Once real data becomes available, the framework can be applied, and parameters can be further calibrated.

5.4.2 Single Pit Features Prediction Results by Surrogate Modeling

The phase-field simulation employed in this study has undergone partial calibration [118]. The total simulation duration spans 1 year, comprising 65 time steps, with each time step equivalent to approximately 5 days. The simulation aims to predict the corrosion morphology and potentials of the plate, considering the mechanical load history and reaction constant.

As outlined in Section 5.3.2, the surrogate model takes the mechanical stress, the reaction coefficient, and three features from the preceding 5 time steps as input. The output of the surrogate model is the opening width of the next time step.

To generate training data for the surrogate model, 200 simulations were conducted, ensuring a reasonable number for local corrosion simulations. For each simulation, 200 locations on the gate were selected to provide the mechanical load, representing the overall stress level. The normalized reaction constant was determined through Sobol sampling within the range from 1 to 10.

Three features γ_k, α_k, c_k are extracted from the morphology of each time point from each simulation. The data is then processed to fit NARX structure for training, i.e., the simulation

time history is cut to input and output pairs.

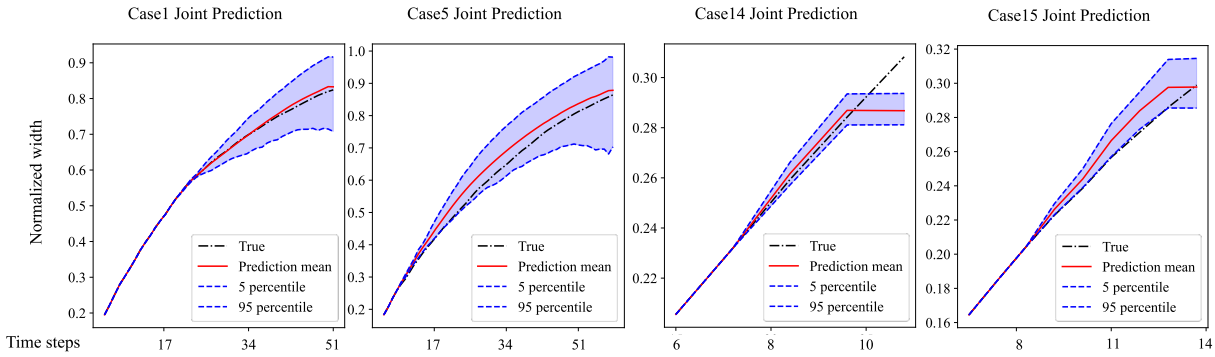

Figure 5.9. Pit opening width prediction results

The model is iteratively applied to forecast the growth of opening width, leveraging the initial features from the first five steps. The prediction outcomes are visualized in Figure 5.9, where the x-axis represents the time steps, and the y-axis signifies the normalized width. Notably, the predictions exhibit accuracy, with the true values consistently falling within the associated confidence intervals. Over time, the confidence interval widens, signifying an increase in prediction epistemic uncertainties. This widening is a consequence of accumulated prediction errors during the recursive forecasting process..

5.4.3 Synthetic Measurement Generation and Corrosion Identification Results

To demonstrate the effectiveness of the CNN model for corrosion identification, a time series of images are synthetically generated using Blender representing the pitting corrosion on a steel plate. As shown in Figure 5.10, the procedure can be described as:

- Initialization of a 3D Plate: A flat surface object, representing a metallic plate, was created as the foundation for the corrosion pits.
- Pitting Information Importation: Data representing the location and growth information of corrosion pits were imported into Blender using Python scripting. This data was sourced from a pre-processed .pickle file.

- Pit Shape Generation: Initially, 100 spherical volumes were created on the plate. These spheres, each with a nominal radius, were positioned at predetermined coordinates. The spheres were then dynamically scaled, based on the imported time-dependent data, to simulate the growth of corrosion pits over time.
- Realism in Pitting Effect: To introduce variability and mimic real corrosion, each sphere was modified with a displacement modifier, creating irregularities at the pit edges. Boolean operations were then used to subtract these spheres from the plate, forming hollows that represent corrosion pits.
- Image rendering: The spherical volumes used in the Boolean operations were made invisible, ensuring that only the corroded plate was visible in the final render. The plate was rendered at each time step, producing a series of images that show the progression of pitting corrosion.

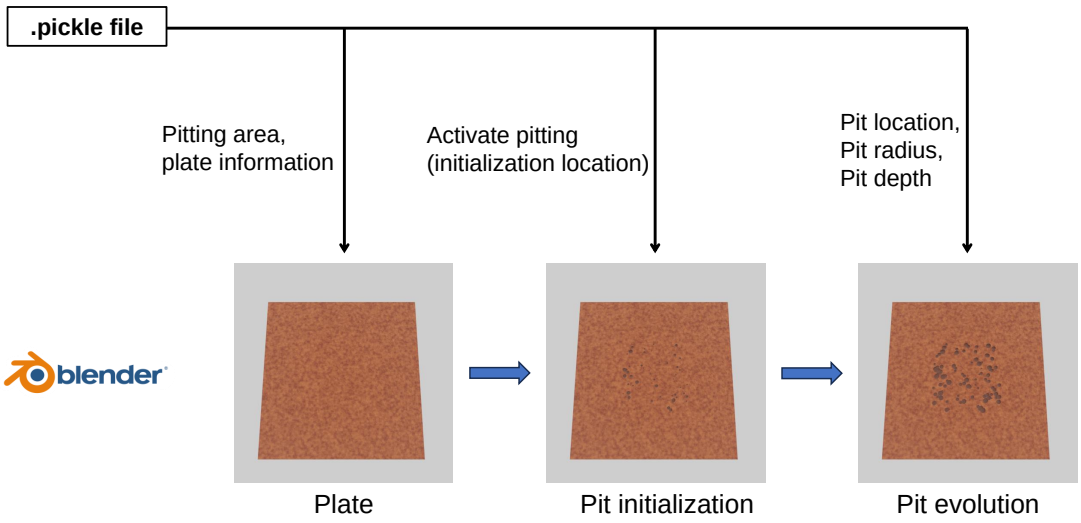

Figure 5.10. Synthetic measurement generation given pitting information.

The generated RGB images are then fed into the trained CNN model for pixel-level corrosion identification. As shown in Figure 5.11, the prediction indicates high consistency and is able to adjust the threshold for binary segmentation maps that reflect the cost of falsely identifying or ignoring the corrosion.

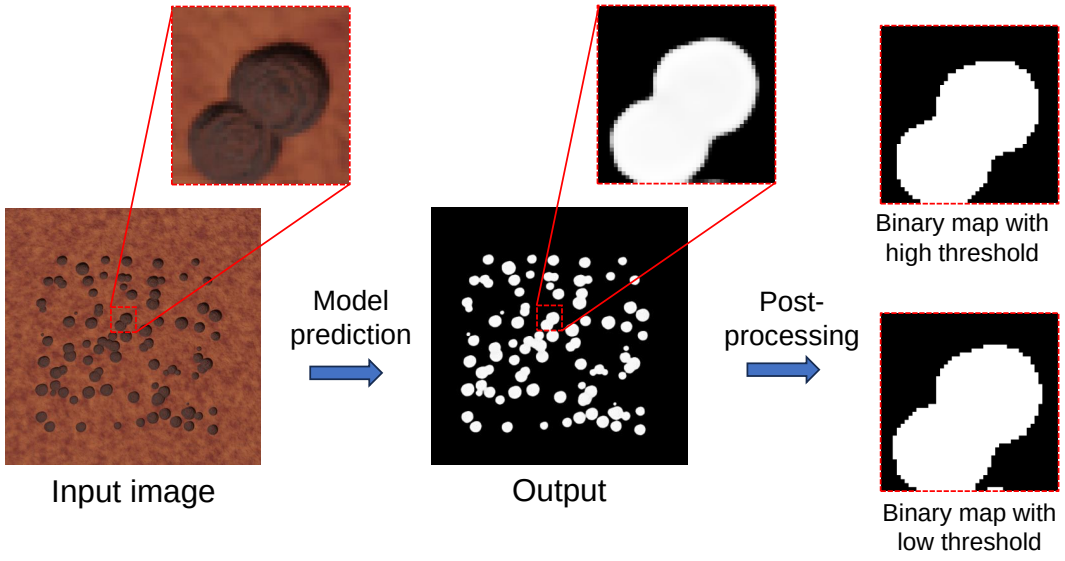

Figure 5.11. CNN output and binary maps after post-processing with different thresholds.

5.4.4 Corrosion Feature Extraction Results

The feature extraction algorithm is applied on the pixel level corrosion identification results of previous step. The number of pits and the opening widths of each picture is going to be identified. The binary pixel-level corrosion identification result is 512 by 512 pixel. The resolution is enhanced by 4 times for both dimensions. Then, the modified circle detection algorithm is applied. The result is as shown in Figure 5.12. Most pits in each image are identified successfully and the identified circle (red circle in the image) is close to the pit boundary. The resolution of current detection algorithm is about 1 millimeter. Considering the limited resolution in the cropped images. As the pit grows, the neighbor pits can touch with each other. Most touching pits can still be detect by the algorithm. However, when multiple pits touch, the pit might not be able to be identified. The example is shown as the middle pit in the red box in Figure 5.12. The middle pit is identified in the time step 30 but cannot be identified in step 40 or 50. One possible reason is that the most part of the middle pit boundary is covered by growing nearby pits. The scale factor is determined by the reference point on the structure in the images.

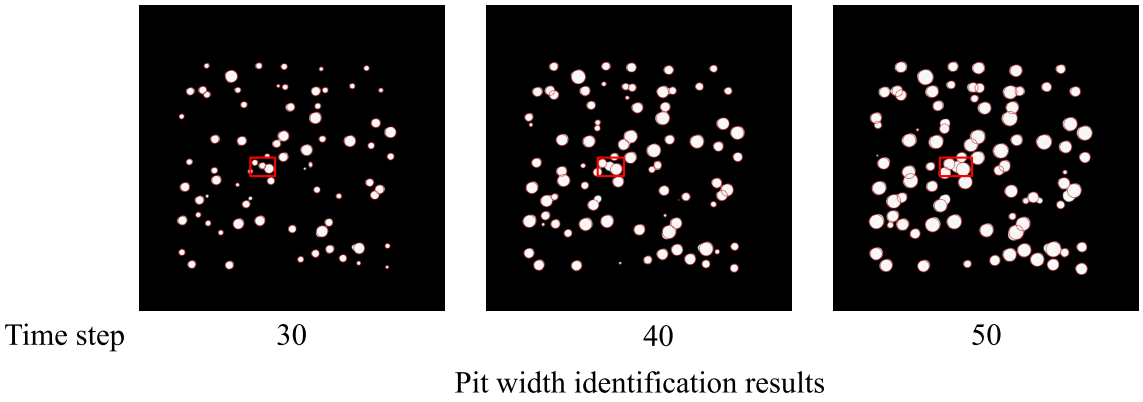

Figure 5.12. Feature extraction results of different time steps

5.4.5 Bayesian Updating Results

In stage 1, the prior distribution for λ and η is a uniform distribution since there is no additional information available about the pit initiation time in the miter gate. Given that η is set to be larger than 1 (as the failure rate generally increases with time in an aging process like corrosion), 1000 samples of λ and η are drawn. These samples are used to generate pit initiation times through the Weibull distribution. The assumed total number of pits generated is 100 within one grid of the surface, based on a measurement result [153]. For each sample, the number of pits at each time step is identified and compared with the observed values. The error is summed over all 65 time steps. About 500 samples with larger errors are rejected. The joint probability density function (PDF) of the posterior distribution is approximated with the remaining samples, as shown in the top-left plot in Figure 5.13. The posterior PDF of stage 1 exhibits significant values around 2.75 for k, while λ has a wider range.

For stage 2, the reaction constant θ is sampled from a uniform distribution ranging from 1 to 10. These samples are concatenated with the remaining λ and η samples from stage 1 to form the prior distribution for stage 2. The three parameters are used to simulate pit growth with the surrogate model for each sample. The pit opening width distribution at each time step is employed to approximate the PDF A_{ki}. The distance between A_{ki} and the PDF $\hat{A}_k$ estimated from observations is summed for all time steps. About 300 samples with large errors are rejected. The

posterior PDFs of stage 2 are displayed in the upper-right, lower-left, and lower-right plots in Figure 5.13. The posterior PDF of η is closer and more concentrated around the real value than in stage 1. However, the posterior PDF tends to be larger than the true value, similar to stage 1. This bias may arise from the detectability limit described in Section 5.4.4, as small pits just initiated cannot be detected. This would cause a delay in initiation times, affecting the shape parameter η, which is related to the distribution position.

The posterior of λ still has a wide range, as shown in the upper-right plot in Figure 5.13, indicating that λ is not easily detectable from the process. The difference between λ and η might be related to their distinct roles in the Weibull distribution; η is the shape parameter, influencing both the shape and the location, whereas λ is the scale parameter, mainly affecting the spread of the distribution without shifting the location. Therefore, the general initiation time point is easier to infer from observations, while the initiation duration or spread is more challenging.

The posterior PDF of θ has one peak close to the true value but another peak near the upper boundary, as the lower-right plot in Figure 5.13 shows. One possible reason for this might be that the surrogate model has some bias in prediction, given the scarcity of training samples near the boundary. While stage 1 only updates λ and η since the reaction constant θ is theoretically not involved, the detectability issue mentioned in Section 5.4.4 might suggest that the reaction constant θ is also influenced by the bias of λ and η, as pits initiated at the same time with different reaction constants will be detected at different times.

It's encouraging to observe that the number of pits predicted using the posterior distribution is very close to the true value, as depicted in Figure 5.14. This outcome highlights the effectiveness of both stage 1 and stage 2 in reducing epistemic uncertainties. The improved accuracy in predicting the number of pits is crucial for enhancing the reliability and applicability of the prognostic model.

It's promising to observe that the prediction results using posterior samples are very close to the true distribution, as shown in Figure 5.15. Additionally, the proximity of the predicted distribution to the true distribution increases with time steps. This behavior aligns with the

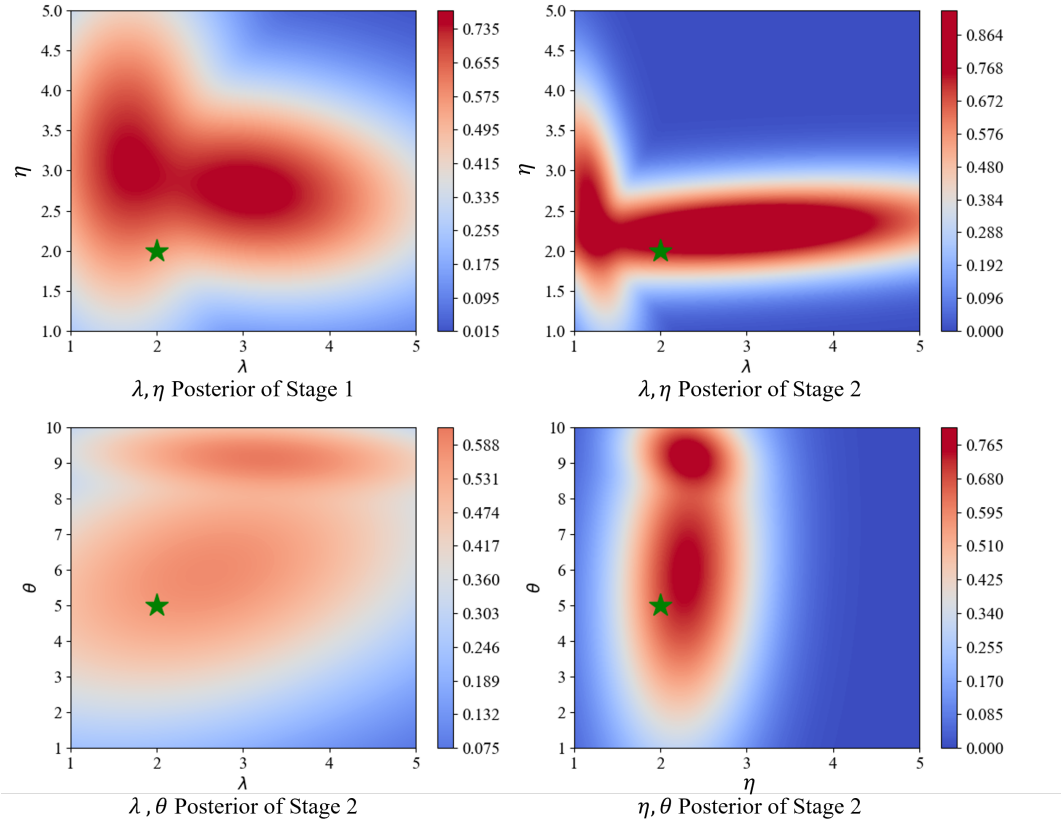

Figure 5.13. Posterior distribution of λ, η and θ

expectation that, over time, the model gains more information, leading to improved predictions. The model's ability to approach the true distribution as time progresses is a positive indication of its effectiveness.

5.5 Conclusions

The proposed pitting corrosion diagnostics and prognostics framework for civil infrastructures represents a comprehensive and sophisticated approach. Here are some key highlights and potential suggestions for improvement:

multi-scale Simulation Approach: The integration of mesoscale corrosion simulation, macroscale structural analysis, and statistical initiation time modeling provides a robust foundation for capturing pitting corrosion in large structures. The use of GP regression models for

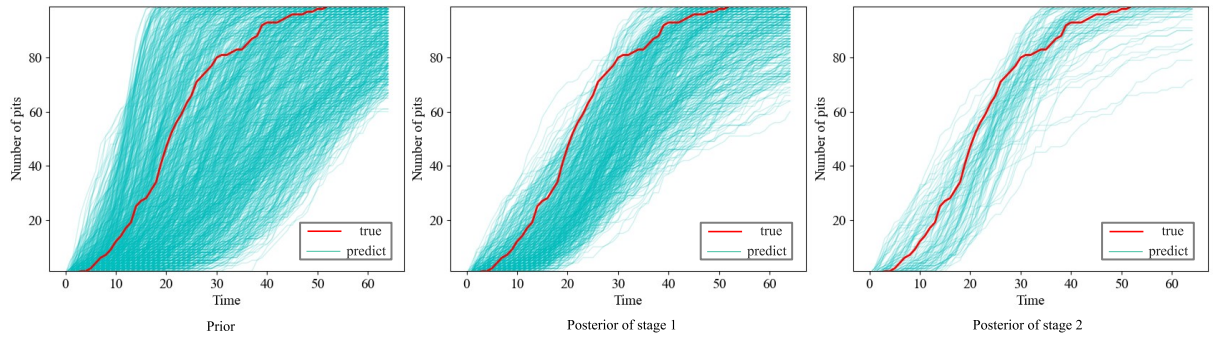

Figure 5.14. Number of pits predicted by prior and posterior distribution

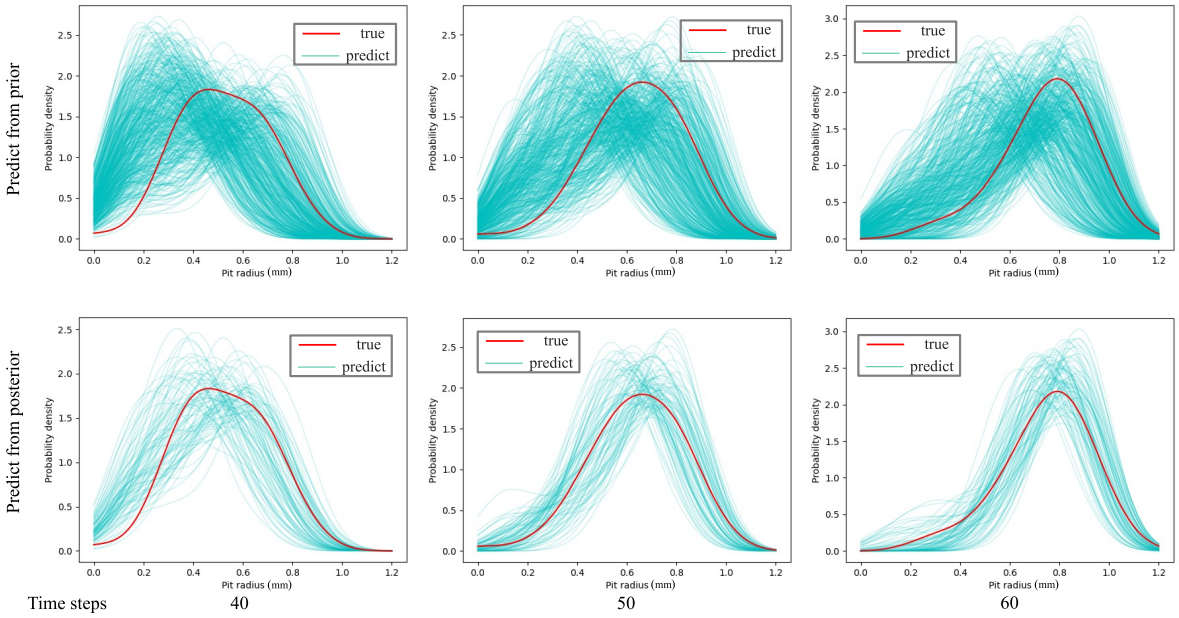

Figure 5.15. Pit opening radius distribution predicted from prior and posterior distribution

accelerating simulations is a practical and efficient choice, demonstrating a balance between accuracy and computational cost.

Detection and Feature Extraction: The CNN-based pit detection method and computer vision-based feature extraction add a practical dimension to the framework, enabling the identification and measurement of pitting corrosion features from inspection images. The application of a two-stage approximate Bayesian computation framework for updating key parameters reflects a thoughtful and systematic approach.

Parameter Update and Prognostics: The two-stage approximate Bayesian computation

framework is effective in updating certain parameters, such as the shape parameter and reaction constant, leading to improved prognostics. The recognition that the scale parameter is challenging to accurately infer is an insightful observation. Further investigation into the sensitivity of the scale parameter and potential improvements in its estimation could be a valuable avenue for future research.

Model Validation and Real-World Application: The application of the framework to the Greenup miter gate and its validation against real-world scenarios provide practical relevance to the proposed methodology. As the study progresses and real data becomes available, continuous validation and calibration against observed data will be crucial for ensuring the reliability of the framework.

Future Directions: The framework's sensitivity to the scale parameter and its potential impact on pitting corrosion growth could be explored further. Understanding the limitations and potential improvements in estimating this parameter would enhance the framework's robustness. The continuous refinement and calibration of the framework against real-world data and scenarios will be essential for its broader applicability to diverse civil infrastructure settings. Consideration of uncertainties and sensitivity analyses could be integrated into the framework to enhance its reliability in different operational and environmental conditions.

Overall, the proposed framework is a promising step towards advancing the field of corrosion diagnostics and prognostics in civil infrastructures. Continued refinement, validation, and adaptation to varying contexts will contribute to its effectiveness and widespread applicability.

5.6 Remarks

Material for this chapter is from the following articles:

[1] **Guofeng Qian**, Zihan Wu, Zhen Hu, and Michael D Todd. Pitting corrosion diagnostics and prognostics using multi-scale simulation and image inspection data. In preparation.

Chapter 6

Conclusions and Future Research

Diagnostics and prognostics for pitting corrosion have been implemented in large civil infrastructures through a comprehensive approach involving multiphysics, multi-scale corrosion simulation, machine learning-based surrogate modeling, uncertainty quantification and reliability analysis, Bayesian model updating, and image-based corrosion identification. The primary contributions of this work encompass the establishment of a connection between mesoscale corrosion simulation and macroscale structural simulation through a multi-scale approach. Additionally, surrogate models have been constructed to expedite physics-based simulations, enabling more efficient probabilistic analyses and enhancing reliability assessment. Furthermore, a comprehensive framework for diagnosing pitting corrosion in civil infrastructure has been introduced, utilizing both strain measurements and image data. Subsequent prognostics is conducted, informed by updates to the model based on the outcomes of the diagnostic process.

In the discussions presented in Chapter 2, it is noted that the current phase-field corrosion model is calibrated for non-stress conditions. There is a recognized need for a quantitative calibration to account for the influence of both static and dynamic stresses on corrosion evolution. The extended duration of the corrosion process poses challenges for calibration efforts. The use of accelerated experiments can facilitate the development of a reasonable time-scaling technique, though the introduction of dynamic stress loads adds complexity to this process.

The small scale of pitting corrosion within large-scale structures necessitates a multi-scale

simulation, as highlighted in Chapter 2. From this perspective, the interaction between models at different scales becomes crucial. The current multi-scale simulation employs one-way coupling from macroscale structural analysis to mesoscale corrosion simulation. However, the direct simulation of the influence of corroded parts on the overall structure is not addressed. While it may not be feasible to directly incorporate small-scale pits into a structural model, the coupling from local pits to the structure is essential for component-level and structural-level damage diagnostics and prognostics.

The incorporation of corrosion initiation into the proposed multi-scale simulation is suggested, considering the improving understanding of the physics and influencing factors of corrosion initiation. The current work relies on a purely statistical approach for the pit initiation process, as discussed in Chapter 2. Although experimental results indicate a correlation between corrosion initiation and mechanical stress, the current understanding is insufficient for physics-based modeling. The modeling of the initiation process could enhance diagnostics, particularly since many initiations occur beneath paint layers, rendering them invisible.

Chapter 5 discusses the selection of pit opening width as the damage feature in this thesis due to its relative ease of detection in images. With a physics-based simulation, exploring the relationship between pit opening width and other pit features, such as pit depth and maximum curvature, becomes feasible. These additional features can enhance diagnostics for other corrosion-related damages like fatigue or stress crack initiation. Further investigation of thresholds using simulations and experiments is warranted.

Bibliography

[1] Ohio river at greenup dam near greenup tailwater monitoring data. https://waterdata.usgs.gov/monitoring-location/03216600/#parameterCode=00065&period=P365D. Accessed: 2023-04-18.

[2] Sanjay Kumar Ahuja and Manoj Kumar Shukla. A survey of computer vision based corrosion detection approaches. *Information and Communication Technology for Intelligent Systems (ICTIS 2017)-Volume 2 2*, pages 55–63, 2018.

[3] KV Akpanyung and RT Loto. Pitting corrosion evaluation: a review. In *Journal of Physics: Conference Series*, volume 1378, page 022088. IOP Publishing, 2019.

[4] Natheer Alatawneh, Peter Ross Underhill, and Thomas W Krause. Low-frequency eddy-current testing for detection of subsurface cracks in cf-188 stub flange. *IEEE Sensors Journal*, 18(4):1568–1575, 2017.

[5] Saad Albawi, Tareq Abed Mohammed, and Saad Al-Zawi. Understanding of a convolutional neural network. In *2017 international conference on engineering and technology (ICET)*, pages 1–6. Ieee, 2017.

[6] Ted L Anderson. *Fracture mechanics: fundamentals and applications*. CRC press, 2017.

[7] Talha Qasim Ansari, Haitao Huang, and San-Qiang Shi. Phase field modeling for the morphological and microstructural evolution of metallic materials under environmental attack. *npj Computational Materials*, 7(1):1–21, 2021.

[8] Talha Qasim Ansari, Jing-Li Luo, and San-Qiang Shi. Multi-phase-field model of intergranular corrosion kinetics in sensitized metallic materials. *Journal of The Electrochemical Society*, 167(6):061508, 2020.

[9] Talha Qasim Ansari, Zhihua Xiao, Shenyang Hu, Yulan Li, Jing-Li Luo, and San-Qiang Shi. Phase-field model of pitting corrosion kinetics in metallic materials. *npj Computational Materials*, 4(1):1–9, July 2018. Bandiera_abtest: a Cc_license_type: cc_by Cg_type: Nature Research Journals Number: 1 Primary_atype: Research Publisher: Nature Publishing Group Subject_term: Chemical engineering;Theory and computation Subject_term_id: chemical-engineering;theory-and-computation.

[10] Charis A Apostolopoulos, Sotiris Demis, and Vagelis G Papadakis. Chloride-induced corrosion of steel reinforcement–mechanical performance and pit depth analysis. *Construction and Building Materials*, 38:139–146, 2013.

[11] Harold Ascher and Harry Feingold. Repairable systems reliability: modeling, inference, misconceptions and their causes. *(No Title)*, 1984.

[12] PM Aziz. Application of the statistical theory of extreme values to the analysis of maximum pit depth data for aluminum. *Corrosion*, 12(10):35–46, 1956.

[13] Parth Bansal, Zhuoyuan Zheng, Chenhui Shao, Jingjing Li, Mihaela Banu, Blair E Carlson, and Yumeng Li. Physics-informed machine learning assisted uncertainty quantification for the corrosion of dissimilar material joints. *Reliability Engineering & System Safety*, 227:108711, 2022.

[14] Felipe Alexander Vargas Bazán and André Teófilo Beck. Stochastic process corrosion growth models for pipeline reliability. *Corrosion Science*, 74:50–58, 2013.

[15] Martin Z Bazant. Theory of chemical kinetics and charge transfer based on nonequilibrium thermodynamics. *Accounts of chemical research*, 46(5):1144–1160, 2013.

[16] Barron J Bichon, Michael S Eldred, Laura Painton Swiler, Sandaran Mahadevan, and John M McFarland. Efficient global reliability analysis for nonlinear implicit performance functions. *AIAA journal*, 46(10):2459–2468, 2008.

[17] Jill Bingham and Mark Hinders. Lamb wave characterization of corrosion-thinning in aircraft stringers: Experiment and three-dimensional simulation. *The Journal of the Acoustical Society of America*, 126(1):103–113, 2009.

[18] Charles Blundell, Julien Cornebise, Koray Kavukcuoglu, and Daan Wierstra. Weight uncertainty in neural networks, 2015.

[19] Francisco Bonnin-Pascual and Alberto Ortiz. Chapter corrosion detection for automated visual inspection. 2014.

[20] G. Bradski. The OpenCV Library. *Dr. Dobb's Journal of Software Tools*, 2000.

[21] Patrick T Brewick. Simulating pitting corrosion in am 316l microstructures through phase field methods and computational modeling. *Journal of The Electrochemical Society*, 169(1):011503, 2022.

[22] Jacques Buffle, Zeshi Zhang, and Konstantin Startchev. Metal flux and dynamic speciation at (bio) interfaces. part i: Critical evaluation and compilation of physicochemical parameters for complexes with simple ligands and fulvic/humic substances. *Environmental science & technology*, 41(22):7609–7620, 2007.

[23] Christopher P. Burgess, Irina Higgins, Arka Pal, Loic Matthey, Nick Watters, Guillaume Desjardins, and Alexander Lerchner. Understanding disentangling in β-vae, 2018.

[24] Sijing Cai, Yunxian Tian, Harvey Lui, Haishan Zeng, Yi Wu, and Guannan Chen. Dense-unet: a novel multiphoton in vivo cellular image segmentation model based on a convolutional neural network. *Quantitative imaging in medicine and surgery*, 10(6):1275, 2020.

[25] Luigi Calabrese, Massimiliano Galeano, Edoardo Proverbio, Domenico Di Pietro, Filippo Cappuccini, and Angelo Donato. Monitoring of 13% cr martensitic stainless steel corrosion in chloride solution in presence of thiosulphate by acoustic emission technique. *Corrosion Science*, 111:151–161, 2016.

[26] P Castaldo, B Palazzo, and A Mariniello. Effects of the axial force eccentricity on the time-variant structural reliability of aging rc cross-sections subjected to chloride-induced corrosion. *Engineering Structures*, 130:261–274, 2017.

[27] NR Cawley and DG Harlow. Spatial statistics of particles and corrosion pits in 2024-t3 aluminium alloy. *Journal of materials science*, 31:5127–5134, 1996.

[28] Alexander F Chadwick, James A Stewart, Raúl A Enrique, Sicen Du, and Katsuyo Thornton. Numerical modeling of localized corrosion using phase-field and smoothed boundary methods. *Journal of The Electrochemical Society*, 165(10):C633, 2018.

[29] Lei Chen, Hao Wei Zhang, Lin Yun Liang, Zhe Liu, Yue Qi, Peng Lu, James Chen, and Long-Qing Chen. Modulation of dendritic patterns during electrodeposition: A nonlinear phase-field model. *Journal of Power Sources*, 300:376–385, 2015.

[30] Long-Qing Chen. Phase-field models for microstructure evolution. *Annual review of materials research*, 32(1):113–140, 2002.

[31] Tianping Chen and Hong Chen. Universal approximation to nonlinear operators by neural networks with arbitrary activation functions and its application to dynamical systems. *IEEE Transactions on Neural Networks*, 6(4):911–917, 1995.

[32] Yilong Chen, Kai Wang, Xiangyun Liao, Yinling Qian, Qiong Wang, Zhiyong Yuan, and Pheng-Ann Heng. Channel-unet: a spatial channel-wise convolutional neural network for liver and tumors segmentation. *Frontiers in genetics*, 10:1110, 2019.

[33] Y Frank Cheng. *Stress corrosion cracking of pipelines*. John Wiley & Sons, 2013.

[34] R Cigna, C Andrade, U Nuernberger, R Polder, R Weydert, and E Siets. Cost 521 action,". *Corrosion of steel in reinforced concrete structure", Final Report, European Communities, Luxembourg*, 2003.

[35] EJ Cross, K Worden, and CR Farrar. Structural health monitoring for civil infrastructure. In *Health Assessment of Engineered Structures: Bridges, Buildings and Other Infrastructures*, pages 1–31. World Scientific, 2013.

[36] C Cuevas-Artega, JA Rodriguez, CM Clemente, and JM Rodríguez. Pitting corrosion damage for prediction useful life of geothermal turbine blade. *American Journal of Mechanical Engineering*, 2(6):164–168, 2014.

[37] Eduardo A Barros de Moraes, Hadi Salehi, and Mohsen Zayernouri. Data-driven failure prediction in brittle materials: A phase field-based machine learning framework. *Journal of Machine Learning for Modeling and Computing*, 2(1), 2021.

[38] Ken Dill and Sarina Bromberg. *Molecular driving forces: statistical thermodynamics in biology, chemistry, physics, and nanoscience*. Garland Science, 2010.

[39] Joshua V. Dillon, Ian Langmore, Dustin Tran, Eugene Brevdo, Srinivas Vasudevan, Dave Moore, Brian Patton, Alex Alemi, Matthew D. Hoffman, and Rif A. Saurous. Tensorflow distributions. *CoRR*, abs/1711.10604, 2017.

[40] Arinan Dourado and Felipe AC Viana. Physics-informed neural networks for corrosion-fatigue prognosis. In *Proceedings of the Annual Conference of the PHM Society*, volume 11, 2019.

[41] Vincent Dubourg, Bruno Sudret, and Franois Deheeger. Metamodel-based importance sampling for structural reliability analysis. *Probabilistic Engineering Mechanics*, 33:47–57, 2013.

[42] B. Echard, N. Gayton, and M. Lemaire. AK-MCS: An active learning reliability method combining Kriging and Monte Carlo Simulation. *Structural Safety*, 33(2):145–154, March 2011.

[43] Benjamin Echard, Nicolas Gayton, and Maurice Lemaire. Ak-mcs: an active learning reliability method combining kriging and monte carlo simulation. *Structural Safety*, 33(2):145–154, 2011.

[44] Brian A Eick, Zachary R Treece, Billie F Spencer Jr, Matthew D Smith, Steven C Sweeney, Quincy G Alexander, and Stuart D Foltz. Automated damage detection in miter gates of navigation locks. *Structural Control and Health Monitoring*, 25(1):e2053, 2018.

[45] Stephen J Engel, Barbara J Gilmartin, Kenneth Bongort, and Andrew Hess. Prognostics, the real issues involved with predicting life remaining. In *2000 ieee aerospace conference. proceedings (cat. no. 00th8484)*, volume 6, pages 457–469. IEEE, 2000.

[46] James A Evans, James R Tallent, Richard D Brown, Anton D Netchaev, Clayton R Thurmer, and ERDC Vicksburg United States. *Determining miter gate plate corrosion and thickness of anti-corrosion coatings; and development of a mobile sensor inspection platform*. US Army Engineer Research and Development Center, Information Technology . . . , 2019.

[47] Charles R Farrar and Keith Worden. An introduction to structural health monitoring. *Philosophical Transactions of the Royal Society A: Mathematical, Physical and Engineering Sciences*, 365(1851):303–315, 2007.

[48] Charles R Farrar and Keith Worden. *Structural health monitoring: a machine learning perspective*. John Wiley & Sons, 2012.

[49] Stuart D Foltz. Investigation of mechanical breakdowns leading to lock closures. Technical report, ERDC-Cerl Champaign United States, 2017.

[50] Raoul François. A discussion on the order of magnitude of corrosion current density in reinforcements of concrete structures and its link with cross-section loss of reinforcement. *RILEM Technical Letters*, 6:158–168, 2021.

[51] Gerald S Frankel, Tianshu Li, and John R Scully. Perspective—localized corrosion: passive film breakdown vs pit growth stability. *Journal of the electrochemical society*, 164(4):C180, 2017.

[52] GS Frankel. Pitting corrosion. *ASM handbook*, 13:236–241, 2003.

[53] Peter W Glynn and Donald L Iglehart. Importance sampling for stochastic simulations. *Management science*, 35(11):1367–1392, 1989.

[54] Kai Goebel, Bhaskar Saha, Abhinav Saxena, N Mct, and N Riacs. A comparison of three data-driven techniques for prognostics. In *62nd meeting of the society for machinery failure prevention technology (mfpt)*, pages 119–131, 2008.

[55] Changqing Gong and Dan M Frangopol. Reliability of steel girder bridges with dependent corrosion growth. *Engineering Structures*, 224:111125, 2020.

[56] JA Gonzalez, Carmen Andrade, C Alonso, and Sebastian Feliu. Comparison of rates of general corrosion and maximum pitting penetration on concrete embedded steel reinforcement. *Cement and concrete research*, 25(2):257–264, 1995.

[57] Alex Graves. Practical variational inference for neural networks. In J. Shawe-Taylor, R. Zemel, P. Bartlett, F. Pereira, and K.Q. Weinberger, editors, *Advances in Neural Information Processing Systems*, volume 24. Curran Associates, Inc., 2011.

[58] David V Grier. The declining reliability of the us inland waterway system. *US Army Corps of Engineers, Institute for Water Resources: Alexandria, VA, USA*, 2005.

[59] Peter G Groer. Analysis of time-to-failure with a weibull model. In *Proceedings of the maintenance and reliability conference*, volume 59, pages 1–4, 2000.

[60] Jiuxiang Gu, Zhenhua Wang, Jason Kuen, Lianyang Ma, Amir Shahroudy, Bing Shuai, Ting Liu, Xingxing Wang, Gang Wang, Jianfei Cai, et al. Recent advances in convolutional neural networks. *Pattern recognition*, 77:354–377, 2018.

[61] Yulin Guo, Sankaran Mahadevan, Shunsaku Matsumoto, Shunsuke Taba, and Daigo Watanabe. Investigation of surrogate modeling options with high-dimensional input and output. *AIAA Journal*, 61(3):1334–1348, 2023.

[62] Emmanuel M Gutman. *Mechanochemistry of solid surfaces*. World Scientific Publishing Company, 1994.

[63] Emmanuel M Gutman. *Mechanochemistry of materials*. Cambridge Int Science Publishing, 1998.

[64] CM Hansson. The impact of corrosion on society. *Metallurgical and Materials Transactions A*, 42:2952–2962, 2011.

[65] DG Harlow and RP Wei. A probability model for the growth of corrosion pits in aluminum alloys induced by constituent particles. *Engineering fracture mechanics*, 59(3):305–325, 1998.

[66] Rosemarie Helmerich and Astrid Zunkel. Partial collapse of the berlin congress hall on may 21st, 1980. *Engineering failure analysis*, 43:107–119, 2014.

[67] Geoffrey E. Hinton and Drew van Camp. Keeping the neural networks simple by minimizing the description length of the weights. In *Proceedings of the sixth annual conference on Computational learning theory - COLT '93*. ACM Press, 1993.

[68] Zhen Hu, Dan Ao, and Sankaran Mahadevan. Calibration experimental design considering field response and model uncertainty. *Computer Methods in Applied Mechanics and Engineering*, 318:92–119, 2017.

[69] Zhen Hu and Sankaran Mahadevan. Global sensitivity analysis-enhanced surrogate (gsas) modeling for reliability analysis. *Structural and Multidisciplinary Optimization*, 53(3):501–521, 2016.

[70] Zhen Hu and Sankaran Mahadevan. Uncertainty quantification and management in additive manufacturing: current status, needs, and opportunities. *The International Journal of Advanced Manufacturing Technology*, 93:2855–2874, 2017.

[71] Songling Huang and Shen Wang. *New technologies in electromagnetic non-destructive testing*. Springer, 2016.

[72] Siavash Jafarzadeh, Ziguang Chen, and Florin Bobaru. Computational modeling of pitting corrosion. *Corrosion reviews*, 37(5):419–439, 2019.

[73] Ricardo Jardim-Goncalves, Manuel Martins-Barata, J Alvaro Assis-Lopes, and Adolfo Steiger-Garcao. Application of stochastic modelling to support predictive maintenance for industrial environments. In *1996 IEEE International Conference on Systems, Man and Cybernetics. Information Intelligence and Systems (Cat. No. 96CH35929)*, volume 1, pages 117–122. IEEE, 1996.

[74] Gaofeng Jia and Alexandros A Taflanidis. Kriging metamodeling for approximation of high-dimensional wave and surge responses in real-time storm/hurricane risk assessment. *Computer Methods in Applied Mechanics and Engineering*, 261:24–38, 2013.

[75] Junfeng Jing, Zhen Wang, Matthias Rätsch, and Huanhuan Zhang. Mobile-unet: An efficient convolutional neural network for fabric defect detection. *Textile Research Journal*, 92(1-2):30–42, 2022.

[76] Martin Jönsson, Bo Rendahl, and Ingegerd Annergren. The use of infrared thermography in the corrosion science area. *Materials and Corrosion*, 61(11):961–965, 2010.

[77] Jack Hinton Julie Vignes, Lance Gullett. Overton Lock and Dam (Lock 2) Dewatering, Inspection and Repair. http://www.rrva.org/02242020/RRVA%20Overton%20Lock%20(Lock%202)%20Dewater%20Inspection%20Repair.pdf, 2020. [Accessed 01-12-2023].

[78] Krishn Katyal and SN Somala. *Computer-Vision based Structural Health Monitoring: Application to Buildings & Bridges*. PhD thesis, Indian Institute of Technology Hyderabad., 2022.

[79] Jack Raymond Kayser. *The effects of corrosion on the reliability of steel girder bridges*. University of Michigan, 1988.

[80] Seong Gyoon Kim, Won Tae Kim, and Toshio Suzuki. Phase-field model for binary alloys. *Physical review e*, 60(6):7186, 1999.

[81] Y Kondo. Prediction of fatigue crack initiation life based on pit growth. *Corrosion*, 45(1):7–11, 1989.

[82] Frank L Lewis. Optimal estimation: with an introduction to stochastic control theory. *(No Title)*, 1986.

[83] Tianshu Li, JR Scully, and GS Frankel. Localized corrosion: passive film breakdown vs pit growth stability: Part ii. a model for critical pitting temperature. *Journal of The Electrochemical Society*, 165(9):C484, 2018.

[84] Tianshu Li, JR Scully, and GS Frankel. Localized corrosion: passive film breakdown vs. pit growth stability: Part iii. a unifying set of principal parameters and criteria for pit stabilization and salt film formation. *Journal of The Electrochemical Society*, 165(11):C762, 2018.

[85] Tianshu Li, JR Scully, and GS Frankel. Localized corrosion: passive film breakdown vs. pit growth stability: Part iii. a unifying set of principal parameters and criteria for pit stabilization and salt film formation. *Journal of The Electrochemical Society*, 165(11):C762, 2018.

[86] Tianshu Li, JR Scully, and GS Frankel. Localized corrosion: passive film breakdown vs. pit growth stability: part iv. the role of salt film in pit growth: a mathematical framework. *Journal of The Electrochemical Society*, 166(6):C115, 2019.

[87] Tianshu Li, JR Scully, and GS Frankel. Localized corrosion: passive film breakdown vs pit growth stability: part v. validation of a new framework for pit growth stability using one-dimensional artificial pit electrodes. *Journal of The Electrochemical Society*, 166(11):C3341, 2019.

[88] Xiang Li, Qian Ding, and Jian-Qiao Sun. Remaining useful life estimation in prognostics using deep convolution neural networks. *Reliability Engineering & System Safety*, 172:1–11, 2018.

[89] Xuanpeng Li, Yang Zhao, Wenlong Qi, Jidong Wang, Junfeng Xie, Hairui Wang, Limin Chang, Bin Liu, Guanxin Zeng, Qiuying Gao, et al. Modeling of pitting corrosion damage based on electrochemical and statistical methods. *Journal of The Electrochemical Society*, 166(15):C539, 2019.

[90] Linyun Liang and Long-Qing Chen. Nonlinear phase field model for electrodeposition in electrochemical systems. *Applied Physics Letters*, 105(26):263903, 2014.

[91] Linyun Liang, Yue Qi, Fei Xue, Saswata Bhattacharya, Stephen J Harris, and Long-Qing Chen. Nonlinear phase-field model for electrode-electrolyte interface evolution. *Physical Review E*, 86(5):051609, 2012.

[92] Bee Lim, Sanghyun Son, Heewon Kim, Seungjun Nah, and Kyoung Mu Lee. Enhanced deep residual networks for single image super-resolution. In *Proceedings of the IEEE conference on computer vision and pattern recognition workshops*, pages 136–144, 2017.

[93] Chen Lin and Haihui Ruan. Multi-phase-field modeling of localized corrosion involving galvanic pitting and mechano-electrochemical coupling. *Corrosion Science*, 177:108900, 2020.

[94] Chen Lin and Haihui Ruan. Phase-field modeling of mechano–chemical-coupled stress-corrosion cracking. *Electrochimica Acta*, 395:139196, 2021.

[95] Chen Lin, Haihui Ruan, and San-Qiang Shi. Phase field study of mechanico-electrochemical corrosion. *Electrochimica Acta*, 310:240–255, 2019.

[96] Roland T Loto and Cleophas A Loto. Corrosion and protection of facilities and infrastructures in telecommunications industry-a review. In *IOP Conference Series: Materials Science and Engineering*, volume 1107, page 012014. IOP Publishing, 2021.

[97] Lu Lu, Pengzhan Jin, Guofei Pang, Zhongqiang Zhang, and George Em Karniadakis. Learning nonlinear operators via deeponet based on the universal approximation theorem of operators. *Nature Machine Intelligence*, 3(3):218–229, 2021.

[98] Weijie Mai and Soheil Soghrati. A phase field model for simulating the stress corrosion cracking initiated from pits. *Corrosion Science*, 125:87–98, 2017.

[99] Weijie Mai, Soheil Soghrati, and Rudolph G Buchheit. A phase field model for simulating the pitting corrosion. *Corrosion Science*, 110:157–166, 2016.

[100] Philippe Marcus. *Corrosion mechanisms in theory and practice*. CRC press, 2011.

[101] S Marinetti and V Vavilov. Ir thermographic detection and characterization of hidden corrosion in metals: General analysis. *Corrosion science*, 52(3):865–872, 2010.

[102] Joe McGlinchy, Brian Johnson, Brian Muller, Maxwell Joseph, and Jeremy Diaz. Application of unet fully convolutional neural network to impervious surface segmentation in urban environment from high resolution satellite imagery. In *IGARSS 2019-2019 IEEE International Geoscience and Remote Sensing Symposium*, pages 3915–3918. IEEE, 2019.

[103] David Montes de Oca Zapiain, James A Stewart, and Rémi Dingreville. Accelerating phase-field-based microstructure evolution predictions via surrogate models trained by machine learning methods. *npj Computational Materials*, 7(1):3, 2021.

[104] David A Najera-Flores, Guofeng Qian, Zhen Hu, and Michael D Todd. Corrosion morphology prediction of civil infrastructure using a physics-constrained machine learning method. *Mechanical Systems and Signal Processing*, 200:110515, 2023.

[105] Saideep Nannapaneni, Zhen Hu, and Sankaran Mahadevan. Uncertainty quantification in reliability estimation with limit state surrogates. *Structural and Multidisciplinary Optimization*, 54:1509–1526, 2016.

[106] Yasutaka Narazaki, Vedhus Hoskere, Koji Yoshida, Billie F Spencer, and Yozo Fujino. Synthetic environments for vision-based structural condition assessment of japanese high-speed railway viaducts. *Mechanical Systems and Signal Processing*, 160:107850, 2021.

[107] F Navai. Effects of tensile and compressive stresses on the passive layers formed on a type 302 stainless steel in a normal sulphuric acid bath. *Journal of materials science*, 30:1166–1172, 1995.

[108] F Navai. Electrochemical behaviour of a type 302 stainless steel in a stress field. *Journal of materials science*, 35:5921–5925, 2000.

[109] Thanh Tung Nguyen, J Bolivar, Y Shi, Julien Réthoré, A King, Marion Fregonese, J Adrien, Jean-Yves Buffiere, and Marie-Christine Baietto. A phase field method for modeling anodic dissolution induced stress corrosion crack propagation. *Corrosion Science*, 132:146–160, 2018.

[110] Marcos E Orchard and George J Vachtsevanos. A particle-filtering approach for on-line fault diagnosis and failure prognosis. *Transactions of the Institute of Measurement and Control*, 31(3-4):221–246, 2009.

[111] Keiron O'Shea and Ryan Nash. An introduction to convolutional neural networks. *arXiv preprint arXiv:1511.08458*, 2015.

[112] Chinedu I Ossai. A data-driven machine learning approach for corrosion risk assessment—a comparative study. *Big Data and Cognitive Computing*, 3(2):28, 2019.

[113] Jeom Kee Paik, Sung Kyu Kim, and Sang Kon Lee. Probabilistic corrosion rate estimation model for longitudinal strength members of bulk carriers. *Ocean Engineering*, 25(10):837–860, 1998.

[114] Warren Milton Persons. Indices of business conditions: an index of general business conditions. 1919.

[115] Guofeng Qian, Zhen Hu, and Michael D Todd. A hybrid surrogate modeling method for corrosion morphology prediction under non-stationary dynamic loading. In *Structural Health Monitoring 2023, Proceedings of the International Workshop on Structural Health Monitoring 2023*, pages 643–650. DEStech, 2023.

[116] Guofeng Qian, Zhen Hu, and Michael D Todd. Physics-based corrosion reliability analysis of miter gates using multi-scale simulations and adaptive surrogate modeling. *Mechanical Systems and Signal Processing*, 200:110619, 2023.

[117] Guofeng Qian, Zhen Hu, and Michael D Todd. Physics-based corrosion reliability analysis of miter gates using multi-scale simulations and adaptive surrogate modeling. In *Society for Experimental Mechanics Annual Conference and Exposition*, pages 101–105. Springer, 2023.

[118] Guofeng Qian, Karnpiwat Tantratian, Lei Chen, Zhen Hu, and Michael D Todd. A probabilistic computational framework for the prediction of corrosion-induced cracking in large structures. *Scientific Reports*, 12(1):20898, 2022.

[119] Shengping Qin and Weicheng Cui. Effect of corrosion models on the time-dependent reliability of steel plated elements. *Marine Structures*, 16(1):15–34, 2003.

[120] Carl Edward Rasmussen, Christopher KI Williams, et al. *Gaussian processes for machine learning*, volume 1. Springer, 2006.

[121] Kevin L Rens, Terry J Wipf, and F Wayne Klaiber. Review of nondestructive evaluation techniques of civil infrastructure. *Journal of performance of constructed facilities*, 11(4):152–160, 1997.

[122] Marco Ricci, Giuseppe Silipigni, Luigi Ferrigno, Marco Laracca, Ibukun D Adewale, and Gui Yun Tian. Evaluation of the lift-off robustness of eddy current imaging techniques. *NDT & E International*, 85:43–52, 2017.

[123] Pierre R Roberge. *Corrosion inspection and monitoring*. John Wiley & Sons, 2007.

[124] DP Rohe and EMC Jones. Generation of synthetic digital image correlation images using the open-source blender software. *Experimental Techniques*, 46(4):615–631, 2022.

[125] Bassem Saassouh and Zoubir Lounis. Probabilistic modeling of chloride-induced corrosion in concrete structures using first-and second-order reliability methods. *Cement and Concrete Composites*, 34(9):1082–1093, 2012.

[126] Sarita Sahu and Gerald S Frankel. Phase field modeling of crystallographic corrosion pits. *Journal of the Electrochemical Society*, 169(2):020557, 2022.

[127] Swarnavo Sarkar and Wilkins Aquino. Changes in electrodic reaction rates due to elastic stress and stress-induced surface patterns. *Electrochimica Acta*, 111:814–822, 2013.

[128] Stefan Scheiner and Christian Hellmich. Stable pitting corrosion of stainless steel as diffusion-controlled dissolution process with a sharp moving electrode boundary. *Corrosion science*, 49(2):319–346, 2007.

[129] Alexander K Schömig and Oliver Rose. On the suitability of the weibull distribution for the approximation of machine failures. In *IIE Annual Conference. Proceedings*, page 1. Institute of Industrial and Systems Engineers (IISE), 2003.

[130] Razieh Shahpir, SS Ghavami, and Alireza Khorsandi. Laser-based multichannel fiber optic sensor for multipoint detection of corrosion. *Optica Applicata*, 46(1):103–115, 2016.

[131] Zhong-Hui Shen, Jian-Jun Wang, Jian-Yong Jiang, Sharon X Huang, Yuan-Hua Lin, Ce-Wen Nan, Long-Qing Chen, and Yang Shen. Phase-field modeling and machine learning of electric-thermal-mechanical breakdown of polymer-based dielectrics. *Nature communications*, 10(1):1843, 2019.

[132] P Shi and S Mahadevan. Corrosion fatigue and multiple site damage reliability analysis. *International Journal of Fatigue*, 25(6):457–469, 2003.

[133] R Sicard, A Chahbaz, and J Goyette. Corrosion monitoring of airframe structures using ultrasonic arrays and guided waves. In *AIP conference Proceedings*, volume 657, pages 806–813. American Institute of Physics, 2003.

[134] Rene Sicard, Ahmad Chahbaz, and Jacques Goyette. Guided lamb waves and l-saft processing technique for enhanced detection and imaging of corrosion defects in plates with small depth-to wavelength ratio. *IEEE transactions on ultrasonics, ferroelectrics, and frequency control*, 51(10):1287–1297, 2004.

[135] René Sicard, Jacques Goyette, and Djamel Zellouf. A saft algorithm for lamb wave imaging of isotropic plate-like structures. *Ultrasonics*, 39(7):487–494, 2002.

[136] Billie F Spencer Jr, Vedhus Hoskere, and Yasutaka Narazaki. Advances in computer vision-based civil infrastructure inspection and monitoring. *Engineering*, 5(2):199–222, 2019.

[137] Janusz Stafiej, Dung Di Caprio, and Łukasz Bartosik. Corrosion-passivation processes in a cellular automata based simulation study. *The Journal of Supercomputing*, 65:697–709, 2013.

[138] Mark G Stewart. Spatial variability of pitting corrosion and its influence on structural fragility and reliability of rc beams in flexure. *Structural safety*, 26(4):453–470, 2004.

[139] Mark G Stewart and Ali Al-Harthy. Pitting corrosion and structural reliability of corroding rc structures: Experimental data and probabilistic analysis. *Reliability engineering & system safety*, 93(3):373–382, 2008.

[140] Mark G Stewart and Qinghui Suo. Extent of spatially variable corrosion damage as an indicator of strength and time-dependent reliability of rc beams. *Engineering Structures*, 31(1):198–207, 2009.

[141] Gian Antonio Susto, Andrea Schirru, Simone Pampuri, Seán McLoone, and Alessandro Beghi. Machine learning for predictive maintenance: A multiple classifier approach. *IEEE transactions on industrial informatics*, 11(3):812–820, 2014.

[142] Xiao-Ming Tan, Yue-Liang Chen, and JIN Ping. Corrosion fatigue life prediction of aircraft structure based on fuzzy reliability approach. *Chinese Journal of Aeronautics*, 18(4):346–351, 2005.

[143] Gregory H Teichert and Krishna Garikipati. Machine learning materials physics: Surrogate optimization and multi-fidelity algorithms predict precipitate morphology in an alternative to phase field dynamics. *Computer Methods in Applied Mechanics and Engineering*, 344:666–693, 2019.

[144] Adam Thelen, Xiaoge Zhang, Olga Fink, Yan Lu, Sayan Ghosh, Byeng D Youn, Michael D Todd, Sankaran Mahadevan, Chao Hu, and Zhen Hu. A comprehensive review of digital twin—part 1: modeling and twinning enabling technologies. *Structural and Multidisciplinary Optimization*, 65(12):354, 2022.

[145] Adam Thelen, Xiaoge Zhang, Olga Fink, Yan Lu, Sayan Ghosh, Byeng D Youn, Michael D Todd, Sankaran Mahadevan, Chao Hu, and Zhen Hu. A comprehensive review of digital twin—part 2: roles of uncertainty quantification and optimization, a battery digital twin, and perspectives. *Structural and multidisciplinary optimization*, 66(1):1, 2023.

[146] HLV Trees. Detection and estimation theory part 1, 1968.

[147] Alma Valor, Francisco Caleyo, Lester Alfonso, Julio Vidal, and José M Hallen. Statistical analysis of pitting corrosion field data and their use for realistic reliability estimations in non-piggable pipeline systems. *Corrosion*, 70(11):1090–1100, 2014.

[148] Manuel A Vega. *Diagnosis, prognosis, and maintenance decision making for civil infrastructure*. University of California, San Diego, 2020.

[149] Manuel A Vega, Zhen Hu, and Michael D Todd. Optimal maintenance decisions for deteriorating quoin blocks in miter gates subject to uncertainty in the condition rating protocol. *Reliability Engineering & System Safety*, 204:107147, 2020.

[150] Manuel A Vega, Zhen Hu, Yichao Yang, Mayank Chadha, and Michael D Todd. Diagnosis, prognosis, and maintenance decision making for civil infrastructure: Bayesian data analytics and machine learning. In *Structural Health Monitoring Based on Data Science Techniques*, pages 45–73. Springer, 2022.

[151] Manuel A Vega, Ramin Madarshahian, Travis B Fillmore, and Michael D Todd. Optimal maintenance decision for deteriorating components in miter gates using markov chain prediction model. 2023.

[152] Leopold Vehovar, V Kuhar, and A Vehovar. Hydrogen-assisted stress-corrosion of pre-stressing wires in a motorway viaduct. *Engineering Failure Analysis*, 5(1):21–27, 1998.

[153] Yafei Wang and Guangxu Cheng. Quantitative evaluation of pit sizes for high strength steel: Electrochemical noise, 3-d measurement, and image-recognition-based statistical analysis. *Materials & Design*, 94:176–185, 2016.

[154] Zequn Wang and Pingfeng Wang. A nested extreme response surface approach for time-dependent reliability-based design optimization. *Journal of Mechanical Design*, 134(12), 2012.

[155] Jarmila Woodtli and Rolf Kieselbach. Damage due to hydrogen embrittlement and stress corrosion cracking. *Engineering failure analysis*, 7(6):427–450, 2000.

[156] Yichao Yang, Mayank Chadha, Zhen Hu, and Michael D Todd. An optimal sensor design framework accounting for sensor reliability over the structural life cycle. *Mechanical Systems and Signal Processing*, 202:110673, 2023.

[157] Yichao Yang, Mayank Chadha, Zhen Hu, Manuel A Vega, Matthew D Parno, and Michael D Todd. A probabilistic optimal sensor design approach for structural health monitoring using risk-weighted f-divergence. *Mechanical Systems and Signal Processing*, 161:107920, 2021.

[158] Tianhe Yu, Saurabh Kumar, Abhishek Gupta, Sergey Levine, Karol Hausman, and Chelsea Finn. Gradient surgery for multi-task learning. *CoRR*, abs/2001.06782, 2020.

[159] Xingliang Yu, Fangyi Wan, and Yingnan Guo. Micromechanics modeling of skin panel with pitting corrosion for aircraft structural health monitoring. In *2016 IEEE International Conference on Prognostics and Health Management (ICPHM)*, pages 1–8. IEEE, 2016.

[160] Qi Zeng, Yash Kothari, Spencer H. Bryngelson, and Florian Schäfer. Competitive physics informed networks, 2022.

[161] Guanfeng Zhang, George A Gazonas, and Florin Bobaru. Supershear damage propagation and sub-rayleigh crack growth from edge-on impact: A peridynamic analysis. *International Journal of Impact Engineering*, 113:73–87, 2018.

[162] Ruoxue Zhang and Sankaran Mahadevan. Reliability-based reassessment of corrosion fatigue life. *Structural safety*, 23(1):77–91, 2001.

[163] Weiping Zhang, Binbin Zhou, Xianglin Gu, and Hongchao Dai. Probability distribution model for cross-sectional area of corroded reinforcing steel bars. *Journal of Materials in Civil Engineering*, 26(5):822–832, 2014.

[164] Y Zhang and A Poursaee. Passivation and corrosion behavior of carbon steel in simulated concrete pore solution under tensile and compressive stresses. *Journal of Materials in Civil Engineering*, 27(8):04014234, 2015.

[165] Ying Zhao, Mayank Chadha, Nicholas Olsen, Elissa Yeates, Josh Turner, Guga Gugaratshan, Guofeng Qian, Michael D Todd, and Zhen Hu. Machine learning-enabled calibration of river routing model parameters. *Journal of Hydroinformatics*, 25(5):1799–1821, 2023.

[166] Ying Zhao, Chen Jiang, Manuel A Vega, Michael D Todd, and Zhen Hu. Surrogate modeling of nonlinear dynamic systems: a comparative study. *Journal of Computing and Information Science in Engineering*, 23(1):011001, 2023.

[167] Zeqi Zhao, Bin Liang, Xueqian Wang, and Weining Lu. Remaining useful life prediction of aircraft engine based on degradation pattern learning. *Reliability Engineering & System Safety*, 164:74–83, 2017.